Annual Report 2013

Center for Nuclear Study,
Graduate School of Science, the University of Tokyo

Editors
  Taku Gunji
  Shinsuke Ota
  Yukino Kishi

Center for Nuclear Study

Annual Report
2013

Preface

This is the annual report of the Center for Nuclear Study (CNS), Graduate School of Science, the University of Tokyo, for the fiscal year 2013 (April 2013 through March 2014). During this period, a lot of research activities in various fields of nuclear physics have been carried out and a wide variety of fruitful results have been obtained at CNS. This report summarizes research such activities. I hereby mention some highlights of the report.

CNS aims to elucidate the nature of nuclear system by producing the characteristic states where the Isospin, Spin and Quark degrees of freedom play central roles. These researches in CNS lead to the understanding of the matter based on common natures of many-body systems in various phases. We also aim at elucidating the explosion phenomena and the evolution of the universe by the direct measurements simulating nuclear reactions in the universe. In order to advance the nuclear science with heavy-ion reactions, we develop AVF upgrade, CRIB and SHARAQ facilities in the large-scale accelerators laboratories RIBF. We started a new project OEDO for a new energy-degrading scheme is proposed, where a RF deflector system is introduced to obtain a good quality of low-energy beam. We promote collaboration programs at RIBF as well as RHIC-PHENIX and ALICE-LHC with scientists in the world, and host international meetings and conferences. We also provide educational opportunities to young scientists in the heavy-ion science through the graduate course as a member of the department of physics in the University of Tokyo and through hosting the international summer school.

The NUSPEQ (NUclear SPectroscopy for Extreme Quantum system) group studies exotic structures in high-isospin and/or high-spin states in nuclei. The CNS GRAPE (Gamma-Ray detector Array with Position and Energy sensitivity) is a major apparatus for high-resolution in-beam gamma-ray spectroscopy. Missing mass spectroscopy using the SHARAQ is going to start as another approach on exotic nuclei. In 2013, the following progress has been made. Experimental programs under the EURICA collaboration were performed for studying evolution of deformation in neutron-rich $Z \sim 60$ nuclei, which are being analyzed now. High-spin states in $A \sim 40$ nuclei were measured at Tandem ALTO facility at IPN Orsay by using fusion reaction, where a new candidate of superdeformed states were found in ^{35}S. Gamow-Teller transitions of ^{8}He were studied by the (p,n) reaction in inverse kinematics, where a prominent sharp peak at $E_x \sim 8$ MeV was found to be the Gamow-Teller resonance. Exothemic charge exchange reactions (^{8}He,^{8}Li*(1+)) on ^{12}C and ^{4}He are being analyzed now. Experiment on the tetra-neutron system via the ^{4}He(^{8}He,^{8}Be)$4n$ reaction is being analyzed, where several tens of events were identified to be candidates of the $4n$ system just above the threshold. The readout system of 14 detectors of the CNS GRAPE was upgraded, where digital pulse data taken by sampling ADCs are analyzed by FPGAs on boards.

The nuclear astrophysics group in CNS is working for experiments using the low-energy RI beam separator CRIB. In September, 2013, beta-delayed alpha decay of ^{16}N, which is relevant for the astrophysical ^{12}C(α, γ) reaction rate, was measured at CRIB using an active target system (GEM-MSTPC). Many decay events were detected from ^{16}N beam particles stopped in the active target. ^{15}O and ^{10}Be beams were produced for the first time at CRIB, and both beams will be used for resonant scattering experiments. Based on recent collaboration on nuclear astrophysics at CRIB, two memoranda of understanding on the collaborated research have been made between CNS and IBS (Korea), and CNS, INFN-LNS (Italy) and CNS-SKKU (Korea).

Main goal of the quark physics group is to understand the properties of hot and dense nuclear matter created by colliding heavy nuclei at relativistic energies. The group has been involved in the PHENIX experiment at Relativistic Heavy Ion Collider (RHIC) at Brookhaven National Laboratory, and the ALICE experiment at Large Hadron Collider (LHC) at CERN. As for ALICE, the group has been involved in the data analyses, which include the analysis of the nuclear modification of energetic neutral pions in Pb-Pb collisions, and measurement of low-mass lepton pairs in Pb-Pb and p-Pb

collisions. The group has been involved in the ALICE-TPC upgrade using a Gas Electron Multiplier (GEM) since 2012. Systematic studies of gain stability, ion back flow, and energy resolutions with various field configurations and space-charge density are underway at CNS and at CERN. Performance evaluation of the COBRA-GEM for the ALICE-TPC upgrade has been measured.

A main subject of the SHARAQ program is charge-exchange reactions induced by heavy-ion beams, with which a variety of selectivities in transferred quantum numbers, ΔS, ΔT, ΔT$_z$, ΔL etc, are available. This year SHARAQ group made preparations for the coming two experiments. One was for the development of parity-transfer probe (^{16}O, ^{16}F(g.s.)) reaction. A MWDC was installed at the exit of the first dipole magnet of SHARAQ to track the proton produced from the instant decay of ^{16}F(g.s.) $\rightarrow$ ^{15}F + p. The other was for the mass measurement around $A \sim 50$ isotopes including ^{54}Ca by the $B\rho$-TOF method. For this purpose, a set of CVD diamond detectors was developed and we attained a time resolution of 27 ps. Also a detector system for tagging the isomers at the final focal plane of the SHARAQ was developed. As a project of near future, a letter of intent was submitted to NP-PAC aiming at studying spin-isospin response of isomers by (p, n) reaction.

In a project of active target development, technical development of gating operation of GEM has been done for one active target and the alpha emission following the beta decay of ^{16}N was measured with the same active target. The development for the high intensity beam injection is being performed for the other active target. The test experiment with a high intensity ^{132}Xe beam was performed.

One of the Major tasks of the accelerator group is the AVF upgrade project that includes development of ion sources, upgrading the AVF cyclotron of RIKEN and the beam line to CRIB. Development of ECR heavy ion sources is to provide a new HI beams, higher and stable beams of metallic ions, and to improve the control system. The Hyper ECR and the Super ECR sources provide all the beams for the AVF cyclotron and support not only CRIB experiments but also a large number of RIBF experiments. Injection beam monitoring and control are being developed and studied. Detailed study of the optics from the ion sources are expected to improve transmission and qualities of beams for the RIBF facility.

The nuclear theory group has been promiting the RIKEN-CNS Collaboration project on large-scale nuclear structure calculations since 2001 and maintain its PC cluster. Based on this experience and its achievements, we participated in activities of HPCI Strategic Programs for Innovative Research (SPIRE) Field 5 The origin of matter and universe since 2011. The SPIRE project aims at an integral understanding of the origin and structure of matter and the universe utilizing the K computer. In the SPIRE project, we are in charge of the elucidation of nuclear properties using ultra large-scale simulations of quantum many-body systems and its applications. In order to perform large-scale shell-model calculations, we developed an efficient computer program of the Monte Carlo Shell Model (MCSM) method for massive parallel computation, and per- formed benchmark calculations at K computer. We have studied both the medium-heavy and light nuclei with large model space on K computer in 2013. In medium-heavy nuclei, we successfully describe the shape coexistence for ^{68}Ni. In light nuclei, systematic calculations have been performed with increasing the number of the major shells. The α cluster structure in Be isotopes has been also studied.

The 12th CNS-EFES International Summer School (CNS-EFES13) has been organized in August 2013 with many invited lecturers including four foreign distinguished physicists.

Finally, I thank Mr. Yoshimura and other administrative stuff members for their heartful contributions throughout the year.

Takaharu Otsuka
Director of CNS

Table of Contents

1a. Experimental Nuclear Physics: Low and Intermediate Energies

S. Go, E. Ideguchi, R. Yokoyama, M. Kobayashi, K. Kisamori, M. Takaki, H. Miya, S. Ota, S. Michimasa, S. Shimoura, M. Niikura, T. Koike, T. O. Yamamoto, Y. Ito, J. Takatsu, A. Yagi, H. Nishibata, T. Suzuki, K. Shirotori, Y. X. Watanabe, Y. Hirayama, M. Sugawara, M. Koizumi, Y. Toh, T. Shizuma, A. Kimura, H. Harada, K. Furutaka, S. Nakamura, F. Kitatani, Y. Hatsukawa, M. Oshima, I. Matea, D. Suzuki, D. Verney, F. Azaiez

1b. Experimental Nuclear Physics: PHENIX Experiment at BNL-RHIC and ALICE Experiment at CERN-LHC

2. Accelerator and Instrumentation

3. Theoretical Nuclear Physics

4. Other Activities

Appendices

Experimental Nuclear Physics: Low and Intermediate Energies

First production of ^{10}Be beam at CRIB and ^{10}Be+α resonant elastic scattering

H. Yamaguchi, D. Kahl, S. Hayakawa, Y. Sakaguchi, T. Nakao[a], Y. Wakabayashi[b], T. Suhara[c],
Y. Kanada-En'yo[d], A. Kim[e], K.Y. Chae[e], P.S. Lee[f], S.M. Cha[e], M.S. Gwak[e], D.H. Kim[g],
T. Hashimoto[h], T. Kawabata[d], T. Teranishi[i], N. Iwasa[j], J.Y. Moon[h], Y.K. Kwon[h], E. Milman[b]

Center for Nuclear Study, Graduate School of Science, the University of Tokyo
[a]Advanced Science Research Center, Japan Atomic Energy Agency
[b]RIKEN Nishina Center
[c]Matsue College of Technology
[d]Department of Physics, Kyoto University
[e]Department of Physics, Sungkyunkwan University
[f]Department of Physics, Chung-Ang University
[g]Department of Science Education, Ewha Womans University
[h]Institute for Basic Science
[i]Department of Physics, Kyushu University
[j]Department of Physics, Tohoku University
[d]Advanced Science Research Center, JAEA

α-cluster states are known to emerge in many nuclei, including carbon isotopes. Among α-cluster states, linear-chain cluster states have been considered as exotic and of interest for a long time. In spite of the long history of theoretical investigation, we have obtained no clear experimental evidence for such states for the moment.

The search for linear-chain cluster structure in carbon or other nuclei has a long history. The early work by Morinaga [1] suggested that the Hoyle state in ^{12}C may correspond to a state of three α particles ordered in a line. Later it was pointed out by Horiuchi [2, 3] using the orthogonality condition model (OCM) that the Hoyle state could be a molecular-like level of ^{8}Be+α, or equivalently three α particles weakly coupled to each other, instead of a linear chain.

As for the other carbon isotopes, Itagaki et al. [4] discussed linear-chain states in ^{12,14,16}C using a microscopic model. They investigated breathing and bending motions and concluded that ^{16}C might have a linear-chain structure with a stability but at high excitation energies E_{ex} above 20 MeV. In their following work [5], it was discussed that an equilateral-triangular shaped cluster structure is expected to appear in ^{14}C. Such a structure should be reflected to a rotational band with $K^{\pi} = 3^{-}$, the first members of which may correspond to the known $E_{ex} = 9.80$ MeV (spin and parity $J^{\pi} = 3^{-}$) and 11.67 MeV (4^{-}) states. In the work by Oertzen et al. [6], prolate $K = 0^{\pm}$ bands in ^{14}C were proposed. It was discussed that the states in these bands may have a linear cluster structure, but the reasoning was only based on the relatively large momentum of inertia, and the J^{π} values had been confirmed only for low-lying levels (0^{+}, 1^{-}, and 2^{+}) in the bands. Thus, a clear evidence of linear chain structure was not presented.

Suhara and En'yo [7, 8] also obtained a band (0_5^{+}, 2_6^{+}, 4_6^{+}) which could be explained as linear-chain cluster levels. It was predicted that these levels appear a few MeV or more above the ^{10}B+α threshold, unlike the prolate bands in [6]. The investigation in [8] shows that the AMD wave function has a configuration in which two α particles and two neutrons are closely located, while the remaining α particle is more distant. This implies states having such a linear-chain configuration could be accessed from the ^{10}Be+α channel.

The excited states in ^{14}C had been studied by various re-actions such as ^{9}Be(^{6}Li, p)^{14}C. Some recent studies were motivated by the interest on the cluster structure in ^{14}C, and performed with ^{7}Li(^{9}Be, ^{14}C*)d [9], $2n$-transfer [6], reactions of ^{12}C(^{6}He, α)^{14}C [10], ^{14}C(^{13}C, ^{14}C*) [11], ^{14}C(^{14}C, ^{14}C*) [12], and ^{12}C(^{16}O, ^{14}O)^{14}C* [13], where ^{14}C* could be detected as ^{10}Be+α or ^{13}C+n. There are resonances commonly observed in several methods, but only the energies are determined. To discuss the structure more precisely, we need additional information such as their J^{π} and α widths, which are still not known.

The purposes of the present work can be summarized as follows: 1) To search a linear-chain configuration via ^{10}Be+α resonant scattering, and 2) To determine resonant parameters of the high excited states (13-18 MeV) of ^{14}C, which are still mostly unknown.

In the present study, the thick-target method in inverse kinematics [14] was used, which has been applied for many measurements at CRIB and produced fruitful results. In particular, there are two resonant scattering experiments at CRIB recently performed, ^{7}Li+α [15] and ^{7}Be+α [16]. Strong α resonances in ^{11}B and ^{11}C were successfully observed, and we newly determined J^{π} and α widths for some of the resonant states. We proposed negative-parity cluster bands in ^{11}B and ^{11}C, and the moment of inertia of the former one was well reproduced with the theoretical calculation by Suhara and En'yo [17]. Using a similar experimental setup but with a ^{10}Be beam, we can study resonances in ^{14}C above the ^{10}Be+α threshold energy (12.01 MeV).

The first production of the ^{10}Be beam at CRIB was performed for Jan. 17-19, 2014. Using a 5.57 MeV/u primary ^{11}B beam from the AVF cyclotron and a 500-Torr cryogenic deuterium target, ^{10}Be particles were produced via the ^{11}B(d, ^{3}He)^{10}Be reaction in inverse kinematics. We selected the charge state of 4+ with the dipole magnet. The produced ^{10}Be^{4+} beam had a small contamination of ^{10}B^{4+}, which was mostly excluded by inserting a 0.7 μm-thick Mylar film as a charge stripper at the F1 focal plane. The best ^{10}Be beam production rate was 2×10^{4} pps at the final focal plane (F3), The beam energy was 3.51 MeV/u before Parallel-Plate Avalanche Counters (PPACs) installed for the beam monitoring.

We also performed a test measurement of alpha resonant

scattering using a chamber filled with helium-gas at 760 Torr, which served as the target of elastic scattering. The chamber had a beam-entrance window made of a 25 μm-thick Mylar film. A pair of silicon detectors, which had thicknesses of 20 μm and 480 μm respectively, were placed in the gas-filled chamber, consisting a "ΔE-E" telescope. The telescope was located at 482 mm from the Mylar entrance window, exactly on the direction of the beam axis. The beam was degraded and stopped in the thick-gas target and α particles from elastic scatterings were reaching the telescope. The energy spectrum of the α particles had a structure with several peaks as shown in Fig. 1, which should correspond to resonances in ^{14}C.

In summary, we successfully produced an ^{10}Be beam at CRIB for the first time, and also showed that the alpha resonant scattering measurement is feasible. A main measurement of 7.5 days is planned to be performed in 2015.
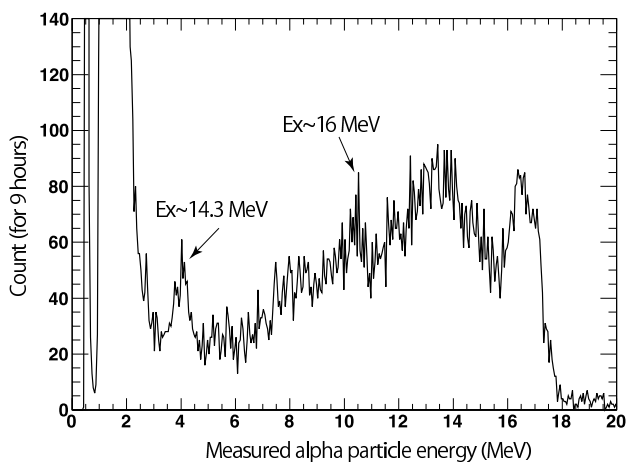
Figure 1: Energy spectrum of α particles. The data were accumulated for 9 hours.

References

[1] H. Morinaga, Phys. Rev. **101** (1956) 254.
[2] H. Horiuchi, Prog. Theor. Phys. **51** (1974) 1266.
[3] H. Horiuchi, Prog. Theor. Phys. **53** (1975) 447.
[4] N. Itagaki, S. Okabe, K. Ikeda, and I. Tanihata, Phys. Rev. C **64** (2001) 014301.
[5] N. Itagaki, T. Otsuka, K. Ikeda, and S. Okabe, Phys. Rev. Lett. **92** (2004) 142501.
[6] W. Oertzen, H. Bohlen, M. Milin, T. Kokalova, S. Thummerer, A. Tumino, R. Kalpakchieva, T. Massey, Y. Eisermann, G. Graw, T. Faestermann, R. Hertenberger, and H.-F. Wirth, Eur. Phys. J. **A21** (2004) 193.
[7] T. Suhara and Y. Kanada-En'yo, Phys. Rev. C **82** (2010) 044301.
[8] T. Suhara and Y. Kanada-En'yo, Phys. Rev. C **84** (2011) 024328.
[9] N. Soić, M. Freer, L. Donadille, N. M. Clarke, P. J. Leask, W. N. Catford, K. L. Jones, D. Mahboub, B. R. Fulton, B. J. Greenhalgh, D. L. Watson, and D. C. Weisser, Phys. Rev. C **68** (2003) 014321.
[10] M. Milin, S. Cherubini, T. Davinson, A. D. Pietro, P. Figuera, D. Miljanić, A. Musumarra, A. Ninane, A. Ostrowski, M. Pellegriti, A. Shotter, N. Soić, C. Spitaleri, and M. Zadro, Nucl. Phys. A **730** (2004) 285.
[11] D. Price, M. Freer, S. Ahmed, N. Ashwood, N. Clarke, N. Curtis, P. McEwan, C. Metelko, B. Novatski, S. Sakuta, N. Soić, D. Stepanov, and V. Ziman, Nucl. Phys. A **765** (2006) 263.
[12] D. L. Price, M. Freer, N. I. Ashwood, N. M. Clarke, N. Curtis, L. Giot, V. Lima, P. M. Ewan, B. Novatski, N. A. Orr, S. Sakuta, J. A. Scarpaci, D. Stepanov, and V. Ziman, Phys. Rev. C **75** (2007) 014305.
[13] P. J. Haigh, N. I. Ashwood, T. Bloxham, N. Curtis, M. Freer, P. McEwan, D. Price, V. Ziman, H. G. Bohlen, T. Kokalova, C. Schulz, R. Torabi, W. v. Oertzen, C. Wheldon, W. Catford, C. Harlin, R. Kalpakchieva, and T. N. Massey, Phys. Rev. C **78** (2008) 014319.
[14] K. P. Artemov, O. P. Belyanin, A. L. Vetoshkin, R. Wolskj, M. S. Golovkov, V. Z. Gol'dberg, M. Madeja, V. V. Pankratov, I. N. Serikov, V. A. Timofeev, V. N. Shadrin, and J. Szmider, Sov. J. Nucl. Phys **52** (1990) 408.
[15] H. Yamaguchi, T. Hashimoto, S. Hayakawa, D. N. Binh, D. Kahl, S. Kubono, Y. Wakabayashi, T. Kawabata, and T. Teranishi, Phys. Rev. C **83** (2011) 034306.
[16] H. Yamaguchi, D. Kahl, Y. Wakabayashi, S. Kubono, T. Hashimoto, S. Hayakawa, T. Kawabata, N. Iwasa, T. Teranishi, Y. Kwon, D. N. Binh, L. Khiem, and N. Duy, Phys. Rev. C **87** (2013) 034303.
[17] T. Suhara and Y. Kanada-En'yo, Phys. Rev. C **85** (2012) 054320.

Measurement of alpha elastic scattering on ^{15}O

A. Kim[a], K. Y. Chae[a], S. M. Cha[a], M. S. Kwag[a], K. I. Hahn[b], D. H. Kim[b], G. W. Kim[b],
S. Y. Han[b], S. H. Choi[c], H. W. Chae[c], Y. H. Kim[c], P. S. Lee[d], J. Y. Moon[e], H. Yamaguchi[f],
D. Kahl[f], and T. Nakao[f]

[a]*Department of Physics, Sung-Kyun-Kwan University*
[b]*Department of Physics, Ewha Womans University*
[c]*Department of Physics, Seoul National University*
[d]*Department of Physics, Chung-Ang University*
[e]*RISP, Institute for Basic Science*
[f]*Center for Nuclear Science, University of Tokyo*

Alpha-cluster structures have been an interesting subjects of study. Several investigations of alpha-cluster structures have been conducted on 4N nuclei such as ^{8}Be, ^{12}C, ^{16}O, and ^{20}Ne [1–3]. In the case of ^{19}Ne, because the system of nuclei can be regarded as ^{20}Ne plus one hole, weakly coupled states of the alpha and hole have been studied theoretically in the low-excitation energy region, but limited experimental data are available, till date. Therefore, experimental study of alpha elastic scattering on ^{15}O is very crucial for understanding how alpha clustering is manifested in proton-rich nuclei. Unknown alpha-cluster states of ^{19}Ne from 1^- and 3^- members (K$^\pi$= 0^- cluster band of ^{20}Ne) as well as 4^+ and 6^+ members (K$^\pi$= 0^+ cluster band of ^{20}Ne) can be identified by performing alpha elastic scattering on ^{15}O. Because the study of alpha cluster states of ^{19}Ne has been carried out theoretically, this experimental result can be used to confirm the alpha-cluster structure of Z>N nuclei of Ne isotopes [4,5].

In addition to the alpha clustering study, the ^{18}F$(p,\alpha)^{15}$O reaction is astrophysically important because the amount of ^{18}F produced in a nova depends sensitively on the reaction rates of ^{18}F$(p,\alpha)^{15}$O and ^{18}F$(p,\gamma)^{19}$Ne. [6] To date, experimental studies using ^{18}F beams as well as theoretical works have been reported competitively. However, resonance parameters of relevant states above the proton threshold at E_x = 6.411 MeV have not been confirmed and remain controversial [7–9]. Therefore, if the resonance properties of ^{19}Ne using ^{15}O$(\alpha, p)^{18}$F are studied, which is a time reverse reaction of ^{18}F$(p,\alpha)^{15}$O, we can expect better results because the ^{15}O + α threshold energy is only 3.53 MeV(E_x of ^{19}Ne). In this study, the ^{15}O$(\alpha, \alpha)^{15}$O reaction was measured in the energy range $E_{c.m.}$ = 1.50 − 7.30 MeV, which corresponds to E_x = 5.03 − 11.03 MeV of ^{19}Ne.

Alpha elastic scattering on ^{15}O was performed using the thick target method, which can provide a continuous excitation function in inverse kinematics because energy loss occurs steadily through thick gas cell filled with ^{4}He. The primary beam, ^{15}N (7.0 MeV/u, 0.6 pμA), was transported from the AVF cyclotron of the RIKEN Accelerator Research Facility to the low-energy RI beam separator, called CRIB at the Center for Nuclear Study, University of Tokyo [10] and impinged on a hydrogen gas target with a thickness of 1.09 mg/cm^2. The primary target was cooled to 80 K by liquid nitrogen in order to avoid breaking the target window by heat [11].

The secondary beam, ^{15}O, was produced by the $p(^{15}$N,$n)^{15}$O reaction. Fig. 1 shows beam identification for ^{15}O and other contaminations on the F2 focal plane. The main contamination of the secondary beam was ^{15}N,
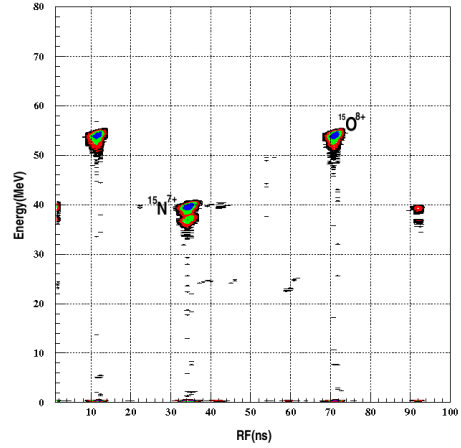
Figure 1: Secondary beam identification on the F2 focal plane.

but it was clearly distinguished from the ^{15}O beam by using the timing information between two PPACs(Parallel Plate Avalanche Counters) [12]. The ^{14}O beam was selectively purified by a Wien filter system so that the beam purity was 90% at the focal plane (F3) of CRIB. The final intensity of ^{15}O beam was 6×10^5 counts/s at the target. The F3 chamber was filled with the helium gas of 760 Torr, which was maintained at room temperature. For detecting the recoiling alpha particles, one set of the ΔE-E telescope at 0 degrees was installed directly in the F3 chamber, which was located at a distance of 200 mm from the entrance window of the chamber. The effective target thickness was 3.32 mg/cm^2 considering the position of the telescope in the F3 chamber. The thicknesses of two detectors are 20μm and 480μm, respectively. The energy of the ^{15}O beam was well-defined with 34 ± 0.5 MeV after the entrance window (Mylar 25 μm-thick) of the F3 chamber. Fig. 2 shows a schematic view of the experimental set-up.
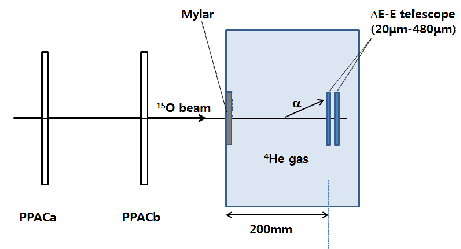
Figure 2: Schematic view of the experimental setup.

The particle identification was clearly performed through the ΔE-E method as shown in Fig. 3. Most of recoiled particles were α and the proton was rarely produced owing to that the proton threshold is about 3 MeV higher than the alpha threshold. The green spot in the alpha particle group was verified with coming from the primary target through the background measurement using the Ar gas target. The data are currently being analyzed.
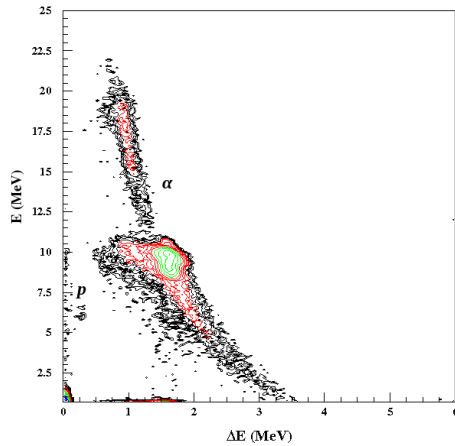
Figure 3: Particle identification in ΔE-E telescope.

References

[1] K. Ikeda *et al.*, Prog. Theor. Phys. Suppl. **68**, 1 (1986).

[2] H. Horiuch *et al.*, Suppl. Prog. Theor. Phys. **192**, 1 (2012).

[3] M. Freer, Rep. Prog. Phys. **70**, 2149 (2007).

[4] F. Nemoto and H. Bando, Prog. Theor. Phys. **47**, 1210 (1972).

[5] T. Sakuda and F. Nemoto, Prog. Theor. Phys. **62**, 1274 (1979).

[6] M. Hernanz *et al.*, Astrophys. J. **526**, L97 (1999).

[7] D. W. Bardayan *et al.*, Phys. Rev. C **70**, 015804 (2004).

[8] H. Fortune *et al.*, Phys. Rev. C **73**, 024302(2006).

[9] A. St. J. Murphy *et al.*, Phys. Rev. C **79**, 058801 (2009).

[10] Y. Yanagisawa *et al.*, RIKEN Accel. Prog. Rep. **30**, 183 (2001).

[11] H. Yamaguchi *et al.*, Nucl. Instrum. Methods Phys. Res. Sect. A **589**, 150 (2008).

[12] H. Kumagai *et al.*, Nucl. Instrum. Methods Phys. Res. Sect. A **470**, 562 (2001).

^{16}N beta delayed alpha decay studied using the Center for Nuclear Study Multi Sampling Time Projection Chamber

S. Cherubini$^{a,\,b}$, S. Hayakawa$^{b,\,d}$, A. Di Pietro^{b}, P. Figuera^{b}, M. Gulino,$^{b,\,c}$ M. La Cognata^{b}, M. Lattuada$^{a,\,b}$, S. Sanfilippo^{a}, C. Spitaleri$^{a,\,b}$, H. Yamaguchi^{d}, D.M. Kahl^{d}, T. Nakao^{d}, S. Kubono^{d}, Y. Wakabayashi^{d}, T. Hashimoto^{f}, N. Iwasa^{g}, Y. Okoda^{g}, K. Ushio^{g}, T. Teranishi^{h}, M. Mazzocco^{i}, C. Signorini^{i}, D. Torresi^{i}, J.Y. Moon^{j}, T. Komatsubara^{j}, P. Lee^{k}, K. Chae^{l}, M. Gwak^{l}.

^{a}Dipartimento di Fisica e Astronomia, Università di Catania, Catania, Italy
^{b}INFN - Laboratori Nazionali del Sud, Catania, Italy
^{c}Università KORE, Enna, Italy
^{d}Center for Nuclear Study, University of Tokyo, Wako Branch, Saitama, Japan
^{e}RIKEN Nishina Center, Wako, Saitama, Japan
^{f}RCNP, Osaka University, Osaka, Japan
^{g}Department of Physics, Tohoku University,Sendai, Japan
^{h}Department of Physics, Kyushu University, Fukuoka, Japan
^{i}Dipartimento di Fisica, Università di Padova and INFN-Sez. Padova, Padova, Italy
^{j}Institute for Basic Science, Daejeon, Korea
^{k}Department of Physics, Chung Ang University, Seoul, Korea
^{l}Department of Physics, Sungkyunkwan University, Seoul, Korea

The importance of measuring the cross section of the nuclear reaction ^{12}C$(\alpha,\gamma)^{16}$O at astrophysical energies is well known. Despite half a century long efforts to perform this measurement, our knowledge regarding this cross section remains unsatisfactory.

The ^{12}C$(\alpha,\gamma)^{16}$O reaction is known to proceed mainly through two radiative capture modes of alpha particles on ^{12}C to ^{16}O. One is the E1 capture with contributions from the ^{16}O state at E$_x$ = 9.585 MeV (E$_r$ = 2.418 MeV) and the subthreshold ^{16}O state at E$_x$ = 7.117 MeV (E$_r$=−45 keV). The other mode is E2 capture and it is dominated by the contributions from direct capture and by the contribution of the subthreshold 2+ state at E$_x$=6.917 MeV (E$_r$=−245 keV). Given the cross section values recalled above, it is clear why all direct measurements done so far were not able to descend below E$_c$.m.=890 keV. As it is often the case in nuclear astrophysics, these data are then extrapolated into the energy region of astrophysical interest using some theoretical approach, usually R-matrix calculations. This led to a situation where the published astrophysical factors range from 1 to 288 keVb for S$_{E1}$(300) and 7 to 120 keVb for S$_{E2}$(300) because the high energy data are not very sensitive to the contributions from subthreshold resonances. To improve the reliability of these extrapolations, data from complementary experiments, such as elastic and quasi-elastic α scattering on ^{12}C, α-transfer reactions to ^{16}O, and ^{16}N decay are usually included in the analyses. Here the contribution from this latter to the study of the ^{12}C$(\alpha,\gamma)^{16}$O reaction is considered, and a completely new experimental technique is suggested together with the use of a ^{16}N beam. The state of the art on these studies is still represented by a paper by Tang and collaborators [3].

The decay of ^{16}N into ^{12}C+α proceeds through a first step governed by a weak process, the beta decay of ^{16}N into ^{16}O*, which can in turn decay to ^{12}C+α. The level scheme of ^{16}N is shown in figure 1. Information on the E1 component of the astrophysical factor of the ^{12}C+α reaction, S_{E_1} can be extracted from the relative height of the of the peak located at roughly 0.9 MeV in the β-delayed α spectrum. The peak at 900 keV originates from the interference of the high-lying 1$^-$ state of ^{16}O at 9.585 MeV with the subthreshold one at 7.117 MeV. This is presently considered the best method to constrain the value of S_{E_1}. Note that the branching ratio for the ^{16}O decay in the channel of interest is 10^{-5}. In order to improve the available results on the measurements of the spectrum of the alpha particles emitted in the decay of ^{16}N, we proposed a new experimental approach based on the use of the Multi Sampling Time Projection Chamber (MSTPC) of the Center for Nuclear Study (CNS) of the University of Tokyo. The limitations arising from the use of implantation foils adopted in all previous experiments were eliminated in the presented study, because the chamber itself becomes the implantation material, and the detection efficiency of the decay products
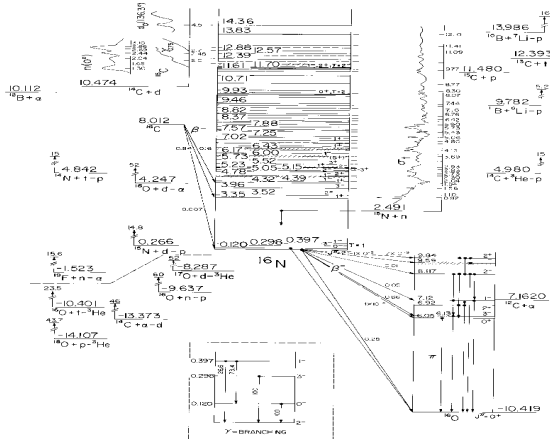
Figure 1: The diagram shows the levels of the ^{16}N nucleus relevant for the present study. The branching ratios to the ^{16}O states of interest are also indicated.

is also increased.

The ^{16}N nucleus has a half-life time $T_{1/2}$=7.1 s and mean-life time τ=10.24 s. If one imagines to send a beam of such particles inside a collection system where they slow down until being stopped the number of particles present at a certain instant of time t will be given by $n(t) = \frac{R}{\lambda}(1 - e^{-\frac{t}{\tau}})$. where R is the rate of incoming particles and $\lambda = 1/\tau$. As expected, the number of particles inside the system does not increase beyond a certain asymptotic value given by $n(t = \infty) = R/\lambda$.

A key point in the experiment was the necessity of using the MSTPC in pulsed mode: an implantation period, during which the beam is sent and stopped in the middle of the active region of the MSTPC, is followed by a time period in which the primary beam is stopped before entering CRIB and the ^{16}N decay events are detected and registered by the MSTPC and its data acquisition system. In order to prevent the destruction of the two gas electron multipliers (GEMs) during the phase when the beam is entering the system, a gating grid was added to the MSTPC to stop electron multiplication during the ^{16}N beam implantation period. Hence

Table 1: Number of decays in 24 hours

ΔT_1 (s)	ΔT_2 (s)	decays/day
0.1	0.1	215974
0.5	0.5	215932
1	1	215805
5	5	211793
10	10	200319
20	20	166234
10	1	70840
5	10	184734

the duty cycle of the experiment will consist in a succession of "beam on, TPC off" and "beam off, TPC on" states. Let's assume that the duration of these states is ΔT_1 and ΔT_2 respectively. The transient time between the on and off states was of the order of a few microseconds and hence completely negligible with respect to all other typical time scale parameters of the experiment, namely ΔT_1, ΔT_2 and τ. The number of decays that it is ideally possible to detect depends on the values ΔT_1, ΔT_2 and τ. The total number of decays can be easily calculated by summing the decays that will take place during the time periods when the TPC is acquiring data, (i.e. the ΔT_2). Various ΔT_1, ΔT_2 pairs have been considered, as shown in the Table 1 above. The calculations are made assuming a beam of 10^6 pps and a branching ratio into the interesting channel of 10^{-5}. In figure 3 the number of particles accumulated in the TPC during the beam on-beam off periods is sketched. The on-off timing showed here are not the optimal ones chosen during the experiment. From the calculation above it follows that a on/off time of the order of 1 s or less is favorable in terms of number of decays. The timing finally adopted was an equal duration of 50 ms for these two periods.

The experiment required a long technical development phase. During this phase, two ^{16}N beam production test runs were performed at the CNS Radioactive Ion Beam (CRIB) facility with very good results. The intesities of the ^{16}N beam obtained during these tests reached 10^6 ions per second. Despite the fact that during the final run of the ex-
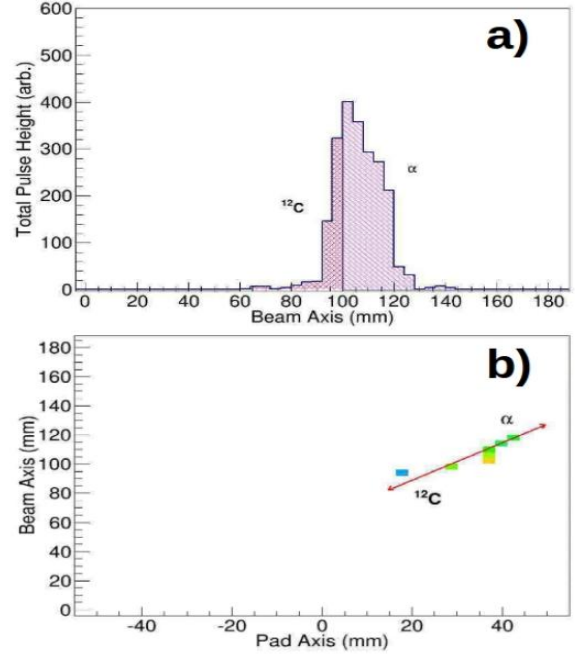
Figure 2: Panel a): energy loss in the TPC along the beam axis: spectrum shape is consistent with a typical Bragg's peak in which we are in presence of two particles, one (more massive) looses its energy faster than the other. Panel b): the same event projected onto yz plane. The track of a back to back decay can be reconstructed.

periment, that took place in September 2013,the intensities of the beam reached a value that was lower than expected, the experiment was technically successful. In figure 4, a candidate decay event obtained from a rough on-line data selaction is shown. New software programs needed to decode and analyze data are presently being developped in orther to start the data analysis.

References

[1] C. E. Rolfs, W. S. Rodney: Cauldrons in the cosmos, The University of Chicago Press, (1988)

[2] F. C. Barker: Austr. J. Phys., 24, 777 (1971)

[3] X. D. Tang *et al.*: Phys. Rev. C81, 045809 (2010)

Spectroscopy of single-particle states in oxygen isotopes via the ^{A}O$(\vec{p}, pN)$ reaction with polarized protons

S. Kawase, T. Uesaka[a], S. Shimoura, K. Yako, S. Ota, S. Michimasa, H. Tokieda, H. Miya[a],
T. L. Tang[†], K. Kisamori[a], M. Takaki, Y. Kubota[a], C. S. Lee[a], R. Yokoyama, T. Fujii, M. Kobayashi,
M. Sasano[a], J. Zenihiro[a], H. Matsubara[a], M. Dozono[a*], H. Sakai[a], T. Kubo[a], K. Yoshida[a],
N. Inabe[a], Y. Yanagisawa[a], H. Takeda[a], K. Kusaka[a], N. Fukuda[a], D. Kameda[a], H. Suzuki[a],
T. Kawahara[b], T. Wakui[c], S. Sakaguchi[d], T. Noro[d], T. Wakasa[d], J. Yasuda[d], T. Fukunaga[d],
Y. Maeda[e], W. Kim[f], S. H. Hwang[f‡], S. Stepanyan[f], A. Obertelli[g], A. Galindo-Uribarri[h],
E. Padilla-Rodal[i], and D. Beaumel[j]

Center for Nuclear Study, Graduate School of Science, the University of Tokyo
[a]*RIKEN (The Institute of Physical and Chemical Research)*
[b]*Department of Physics, Toho University*
[c]*Cyclotron and Radioisotope Center, Tohoku University*
[d]*Department of Physics, Kyushu University*
[e]*Department of Physics, University of Miyazaki*
[f]*Department of Physics and Energy Sciences, Kyungpook National University, Korea*
[g]*CEA Saclay, France*
[h]*Oak Ridge National Laboratory, USA*
[i]*Instituto de Ciencias Nucleares, Universidad Nacional Autónoma de México, México*
[j]*Institut de Physique Nucléaire d'Orsay, France*

The spin-orbit coupling plays a significant role in nuclear system; it causes the energy splitting of the nucleon spin-doublet *i.e.*, single particle levels having the same orbital angular momentum but with opposite direction of the nucleon spin. It was originally introduced by Mayer [1] and Jensen [2] to explain the magic numbers which are developed in stable nuclei and is accounted as a significant success. However, recent studies reveal that the disappearance and appearance of the magic number occur in the region of unstable nuclei [3, 4] and therefore the spin-orbit coupling in that region draws increasing attention. From the experimental point of view, we cannot experimentally measure the spin-orbit coupling itself but alternatively the spin-orbit splitting can be experimentally determined. It is defined as the energy difference of spin-doublets of nucleons and directly reflects the strength of the spin-orbit coupling.

The most straightforward way to observe the spin-orbit splitting is to deduce the single-particle or single-hole excitation energy spectra through direct reactions such as nucleon transfer or nucleon knockout reactions. For that purpose, the exclusive measurement of the $(\vec{p}, pN)$ reaction is an effective spectroscopic tool. One can determine the spin-parity of single-particle states in nuclei from the momentum dependence of the cross section and the vector analyzing power without model dependence [5]. After that, the spin-orbit splitting can be obtained as a difference of the effective single-particle energy (ESPE) of the spin doublet.

We performed $^{14,22-24}$O$(\vec{p}, 2p)$ reaction measurements (SHARAQ04 experiment) with a polarized proton target at RIKEN RIBF to measure single-particle spectra and to determine spin-orbit splitting of 1p proton single particle orbits in $^{14,22-24}$O as a function of their neutron num-
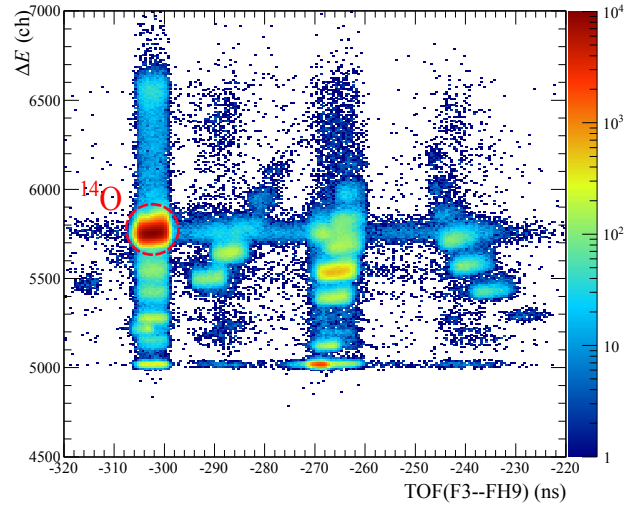
Figure 1: TOF–ΔE plot for beam nuclei. Abscissa is TOF from F3 to FH9 focal plane and ordinate is energy loss in a plastic scintillator at FH9.

ber. For the experimental setup, see ref. [6]. We identified $^{14,22-24}$O$(\vec{p}, 2p)$ reaction via the particle identification (PID) of both incident and residual nuclei in addition to the PID of two scattered protons. The particles are identified via the TOF–ΔE method on an event-by-event basis. For residuals, only their atomic numbers are identified for this time. Figure 1 and 2 show the time-of-flight (TOF)-ΔE correlations for incident and residual particles in ^{14}O runs, respectively. In addition, a selection by the reaction vertex position which deduced from the tracking information of the multi-wire drift chambers located at upstream of the target and at both sides of the beam line. was also applied. This selection reduces the background which came from the
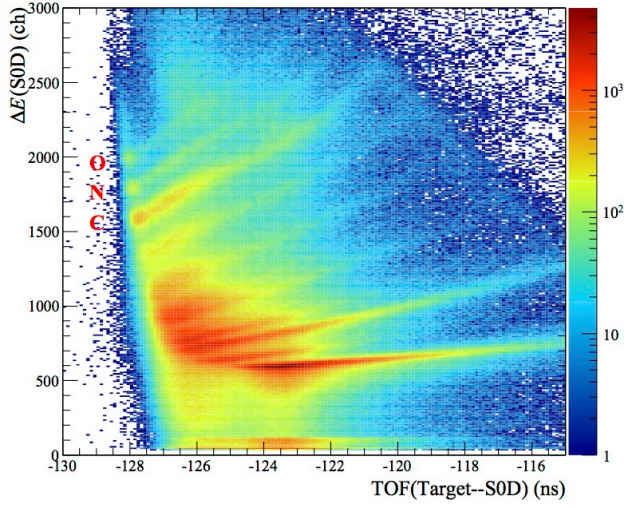
Figure 2: TOF–ΔE plot for residual nuclei. Abscissa is TOF from the target position to S0 downstream (S0D) and ordinate is energy loss in a plastic scintillator at S0D.
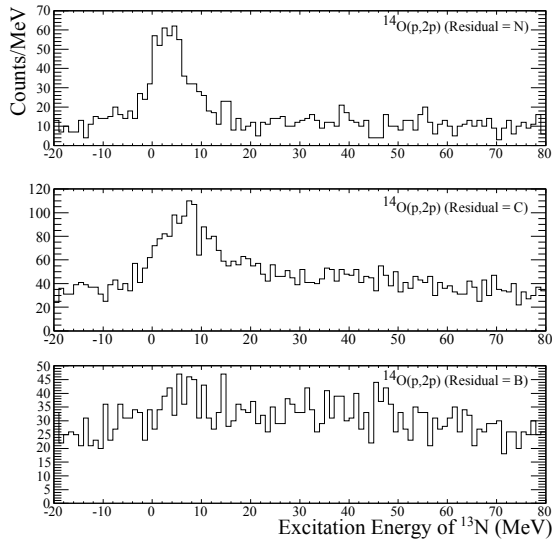
Figure 3: ^{13}N excitation energy spectra via the ^{14}O$(p, 2p)$ reaction for N, C, B residual nuclei

reaction at the target holder and the surrounding materials.

The proton separation energy (S_p) from the target nuclei was calculated from the scattering angles and the momenta of two scattered protons:

$$S_p = (1 - \gamma)m_p - \gamma(T_1 + T_2) + \beta\gamma(p_{1\parallel} + p_{2\parallel}), \quad (1)$$

where γ and β are the Lorentz factor and the velocity of the beam, respectively: m_p is the proton mass, T_1 and T_2 are the kinetic energies of the scattered protons, and $p_{1\parallel}$ and $p_{2\parallel}$ are the momenta of the scattered protons. In this formula, the momentum of the residual nucleus is ignored because its effect to S_p is negligibly small compared with the resolution of S_p. The excitation energy of ^{13}N was calculated as $E_x(^{13}\mathrm{N}) = S_p - 4.627$ MeV. Figure 3 shows the ^{13}N excitation energy spectrum for the ^{14}O$(p, 2p)$ reaction for each residual nucleus. The strengths from the $(p, 2p)$ reaction were succsessfully observed in the spectra with N

and C residuals. The background is mainly coming from the ^{14}O$(^{12}$C$,2p)$ reaction in polarized proton target which includes carbon nuclei and some proton knockout reactions occurred in the surrounding materials. The spectrum for ^{14}O$(p, 2p)$N should include only the ground state of ^{13}N because no excited state of ^{13}N exists below the proton decay threshold of ^{13}N at 1.944 MeV and almost all strength of the excited states instantly decays with proton emission. However, the peak in ^{14}O$(p, 2p)$N spectrum locates at slightly higher energy region than 0 MeV. The origin of this shift is unknown at this time and will be investigated.

We intend to continue the analysis of these results by investigating different gating and energy correction methods that may improve the efficiency, resolution, and S/N ratio.

The analysis for the other oxygen isotopes is in progress.

References

[1] M. G. Mayer, Phys. Rev. **74** (1948) 235; **75** (1949) 1969; **78** (1950) 16; **78** (1950) 22.
[2] O. Haxel, J.H.D. Jensen and H.E. Suess, Phys. Rev. **75** (1949) 1766.
[3] T. Motobayashi *et al.*, Physics Letters B **346** (1995) 9.
[4] A. Ozawa *et al.*, Phys. Rev. Lett. **84** (2000) 5493.
[5] G. Jacob, Th. A. J. Maris, *et al.*, Nucl. Phys. A, **257** (1976) 517.
[6] S. Kawase *et al.*, CNS Ann. Rep. 2012 (2013) 13.

Analysis of proton-proton elastic scattering in SHARAQ04 experiment

T.L. Tang, S. Kawase, T. Uesaka[a], S. Shimoura, K. Yako, S. Ota, S. Michimasa, T. Kawahara[b],
T. Wakui[c], S. Sakaguchi[d], S.H. Hwang[e], Y. Kubota, M. Sasano[a], H. Matsubara[a], M. Dozono[a],
C.S. Lee, H. Tokieda, H. Miya, T. Fujii, K. Kisamori, M. Takaki, R. Yokoyama, M. Kobayashi,
J. Zenihiro[a], H. Takeda[a], K. Kusaka[a], N. Fukuda[a], D. Kameda[a], H. Suzuki[a], W. Kim[e],
S.S. Stepanyan[e], T. Wakasa[d], J. Yasuda[d], T. Fukunaga[d], T. Noro[d], Y. Maeda[f], D. Beaumel[g],
A. Obertelli[h], A. Galindo-Uribarri[i], E. Padilla-Rodal[j]

Center for Nuclear Study, Graduate School of Science, University of Tokyo
[a]RIKEN (The Institute of Physical and Chemical Research)
[b]Department of Physics, Toho University
[c]Cyclotron and Radioisotope Center, Tohoku University
[d]Department of Physics, Kyushu University
[e]Department of Physics and Energy Science, Kyungpook National University
[f]University of Miyazaki
[g]Institut de physique nucleaire d′Orsay
[h]CEA Saclary
[i]Oak Ridge National Laboratory
[j]Instituto de Ciencias Nucleares, Universidad Nacional Autónoma de México

1. Introduction

In SHARAQ04, a (p,2p) knockout experiment was studied by employing polarized proton target [1, 2]. The analysis of the proton-proton elastic scattering (PPES) will be presented in this report. There are two purposes of the analysis: 1) Extraction of the absolute magnitude of spin polarization of the target, and 2) Determination of the angular resolution of the recoil protons and the energy resolution of the experimental setup.
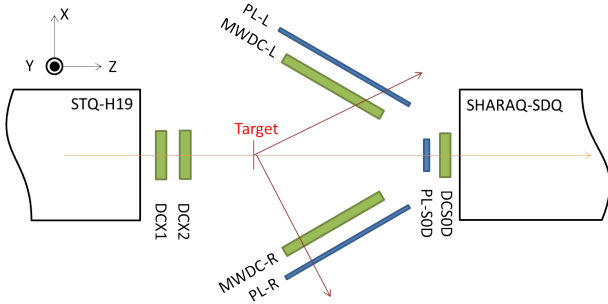
Figure 1: The setup of the detectors in SHARAQ04 experiment. The beam was coming from left to right. The coordinate is defined on the upper left corner.

2. Experimental setup of PPES

The experiment was performed in RIBF, RIKEN Nishina Center. A detailed explanation on the target was described in Ref. [2]. A proton beam at 260 MeV was delivered by BigRIPS to SHARAQ spectrometer. The setup around the target system is shown on Fig. 1. Two low-pressure multi-wire drift chambers (LP-MWDC) (DCX1 and DCX2) [3] were installed on the upstream of the target for tracking of the beam. They were used in beam tuning and turned off during PPES measurement because of low efficiency. Two sets of MWDC [4] and plastic scintillator were placed on the left and right side downstream. The planes of MWDCs and plastic scintillators were set 30° with respect to the Y-Z

plane of laboratory's frame (see Fig. 1). The perpendicular distance from the target to the MWDCs and the plastic scintillators were 1022 mm and 1400 mm respectively. The detectors covered forward angles from 20° to 70°. Scattering angle of the protons in the center of momentum (CM) frame (θ_{NN}) was ranging from 40° to 140°.

3. Spin polarization of the proton target

The polarization of the target was calibrated by PPES for which the analyzing power is known [5]. The scattering angle was divided into 5 sectors equally in the CM frame. The yield of each sector was used to compute the asymmetry. A combined yields (Eq. (1)) formed on left and right detector sets and spin-up and spin-down runs were used to eliminate asymmetry, which originated from the misalignment of the experimental setup or detector's nonuniform efficiency,

$$y_L(i) = \sqrt{Y_L^{\uparrow}(i)Y_R^{\downarrow}(i)}, \quad y_R(i) = \sqrt{Y_R^{\uparrow}(i)Y_L^{\downarrow}(i)} \quad (1)$$

where $Y(i)$ is the yield from the i-th angular sector, the subscript represents left or right and the superscript represents spin-up or spin-down. The asymmetry (ϵ) of the elastic scattering of each sector was calculated by Eq. (2).

$$\epsilon(i) = A_y(i)P = \frac{y_L(i) - y_R(i)}{y_L(i) + y_R(i)} \quad (2)$$

where $A_y(i)$ is the analyzing power, which is known for PPES [5], of the i-th sector and P is the polarization of the target. In relativistic PPES, the laboratory opening angle $\Delta\theta = \theta_1 + \theta_2$ is ranging from 86° to 89° depending on the scattering angle θ_{NN}. Here θ_1 and θ_2 are the scattering angle of the protons in laboratory frame. The background was eliminated by gating on the opening angle, $85° < \Delta\theta < 90°$. The results of the yield and the asymmetry are shown in Fi. 2. The deduced magnitude of spin polarization was $31 \pm 15\%$. Note that the magnitude of the spin polarization was assumed to be equal for spin-up and spin-down runs (Ref. [2], Fig. 2).
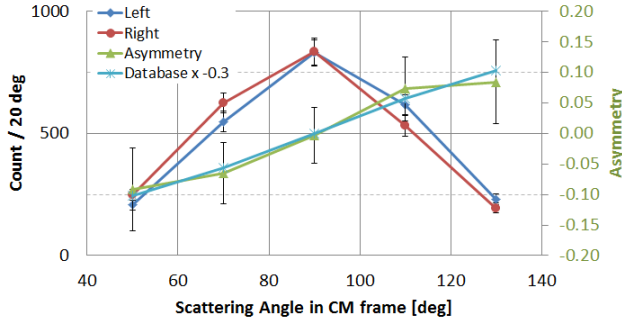
Figure 2: Combined yields of y_L (blue) and y_R(red), and asymmetry (green) versus the scattering angle in CM frame (θ_{NN}).

4. Cross section of proton-proton elastic scattering

The number of incident proton was 2.13×10^9. The target thickness was 1.00 ± 0.05 mm and the number of proton in the target was $4.3(2) \times 10^{21}$ cm^{-2}. The fraction of beam, which hit on the target, was inspected from optics runs and the result was 33%. The DAQ live time was 77%. The combined efficiency of MWDCs was 76%. The total yield was 5032. The cross section was then 2.7 ± 0.3 mb. The error mainly came from the target thickness. The result was compared with data of PPES in the database [5]. The calculation of the cross section from the database (including the detectors acceptance) was 2.51 mb. Our result was consistent with the database.

5. Angular and energy resolution

The opening angle around $|\theta_{NN} - 90°| < 5°$ is almost a delta distribution with width $0.0141°$. Therefore, the resolution of the opening angle can be evaluated by gating on θ_{NN}. A gate from azimuthal opening angle $\Delta\phi = (\phi_2 - 180°) - \phi_1$ was applied for more restricted condition for PPES. Here ϕ_1 and ϕ_2 are the laboratory azimuthal angle of scattered protons. Fig. 3 shows the distribution of the opening angle by gating on the scattering angle $|\theta_{NN} - 90°| < 5°$ and the azimuthal opening angle $|\Delta\phi| < 7.5°$. The background (red line) was estimated by negation of the azimuthal opening angle gate. The resolution of the opening angle was $0.49°$. Assuming the angular resolutions for both recoil protons were the same, i.e. $\sigma(\theta_1) = \sigma(\theta_2)$, then the angular resolution was $0.35°$ for each proton.
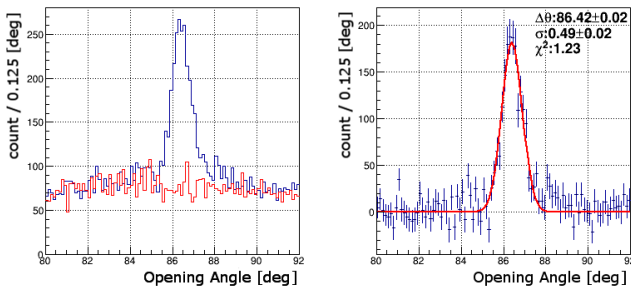
Figure 3: (Left) The distribution of opening angle near $\theta_{NN} = 90°$ (see main text). The blue line is signal. The red line is estimated background. (Right) The background subtracted signal with Gaussian fitting.

The energy resolution was deduced from the width of the excitation energy spectrum in PPES. Fig. 4 shows the spec-

trum. The spectrum was gated by the same opening angle and azimuthal opening angle gates. The background (red line) was estimated by negation of the azimuthal opening angle gate. The background subtracted signal was fitted with a Gaussian. The standard deviation of the Gaussian was 2.88 ± 0.07 MeV, which was the resolution of the excitation energy in (p,2p) reaction. This resolution agrees with kinematics calculation, in which the angular resolution and the time resolution of recoil protons were set to be $0.35°$ and 500 ps respectively.
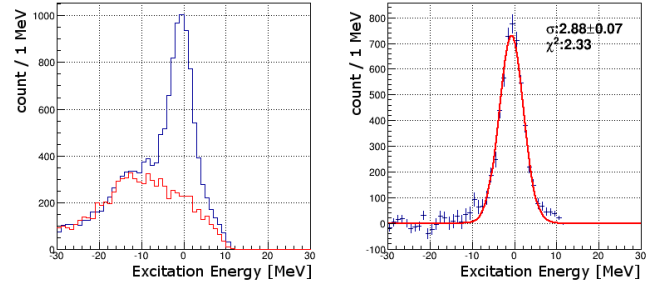
Figure 4: (Left) The distribution of excitation energy with gates (see main text). The blue line is signal. The red line is estimated background. (Right) The background subtracted signal with Gaussian fitting.

6. Conclusion

The analysis of proton-proton elastic scattering have shown that the magnitude of the proton spin polarization in the target was $31 \pm 15\%$, the cross section was consistence with the nucleon-nucleon scattering database, the angular resolution for the recoil proton was $0.35°$, and the separation energy resolution was 2.88 ± 0.07 MeV. These values help later analyses on the (p,2p) reactions.

References

[1] S. Kawase *et al.*, CNS annual report 2012, **13** (2013).
[2] T.L. Tang *et al.*, CNS annual report 2012, **59** (2013).
[3] H. Miya *et al.*, Nucl. Instrum. Methods Phys. Res., Sect. B, **317** (2013)
[4] H. Okamura *et al.*, Nucl. Instrum. and Methods Phys. Res., Sec. A, **406** (1998), p. 78
[5] CNS Data Analysis Center, http://gwdac.phys.gwu.edu/

Missing-mass spectroscopy of the 4n system by ^{4}He(^{8}He, ^{8}Be)4n reaction at high beam counting rate

K. Kisamori, S. Shimoura, H. Miya, M. Assie[a], H. Baba[b], T. Baba[c], D. Beaumel[a], M. Dozono[b], T. Fujii, N. Fukuda[b], S. Go, F. Hammache[a], E. Ideguchi[d], N. Inabe[b], M. Itoh[e], D. Kameda[b], S. Kawase, T. Kawabata[c], M. Kobayashi, Y. Kondo[f], T. Kubo[b], Y. Kubota, M. Kurata-Nishimura[b], C. S. Lee, Y. Maeda[g], H. Matsubara[k], S. Michimasa, K. Miki[d], T. Nishi[h], S, Noji[i], S. Ota, S. Sakaguchi[j], H. Sakai[b], Y. Sasamoto, M. Sasano[b], H. Sato[b], Y. Shimizu[b], A. Stolz[a] H. Suzuki[b], M. Takaki, H. Takeda[b], S. Takeuchi[b], A. Tamii[d], L. Tang, H. Tokieda, M. Tsumura[c], T. Uesaka[b], K. Yako, Y. Yanagisawa[b] and R. Yokoyama

Center for Nuclear Study, Graduate School of Science, University of Tokyo
[a]IPN, Orsay, Fance
[b]RIKEN (The Institute of Physical and Chemical Research)
[c]Department of Physics, Kyoto University
[d]Research Center Nuclear Physics, Osaka University
[e]Cyclotron and Radioisotope Center, Tohoku University
[f]Depertment of Physics, Tokyo Institute of Technology
[g]Faculty of Engineering, University of Miyazaki
[h]Depertment of Physics, University of Tokyo
[i]National Supercoduction Cyclorton Laborator, Michigan State University, USA
[j]Faculty of Sciences, Kyushu University
[k]National Institute of Radiological Sciences

Since possible candidate of bound tetra-neutron was firstly reported [1], multi-neutron systems in nuclei have attracted keen attentions of both the experimentalists and theorists. On the other hand, theoretical studies using ab-initio calculations [2] have suggested that the tetra-neutron cannot exist as a bound system.

We performed missing-mass spectroscopy of the 4n system via an exothermic double-charge exchange reaction ^{4}He(^{8}He,^{8}Be)4n. The purpose of this experiment was to obtain information on few-body forces, such as the $T=3/2$ three body force, and the correlations between in multi-body scattering states that reflect final state interactions of sub-systems, such as di-neutron correlations. In order to produce the 4n system with a small momentum transfer of less than 20 MeV/c, a secondary beam of ^{8}He with a large internal energy, 190 AMeV, was used.

The experiment was performed at the RIKEN RI Beam Factory (RIBF) using the SHARAQ spectrometer and a liquid He target system. The Be target at BigRIPS-F0 was bombarded by a primary beam of ^{18}O at 230 AMeV to produce the ^{8}He secondary beam. We measured the momentum of the ^{8}He in event-by-event at BigRIPS-F6 with the High-Resolution-Beamline and also measured the momentum of two alpha particles, which were the decay products of the ^{8}Be ejectile, with the SHARAQ spectrometer.

Because a small cross section was expected for this reaction, it was important to achieve a large yield and good S/N ratio. The highest ^{8}He beam intensity in this experiment was 2×10^6 counts/sec at the secondary target, which was produced by the 13.7 MHz AVF cyclotron. Because of the high intensity, the percentages of events recorded two ^{8}He particles, which we call here multi-particle events, were about 15 % in the same beam bunch, about 15 % in the neighboring bunches, respectively.
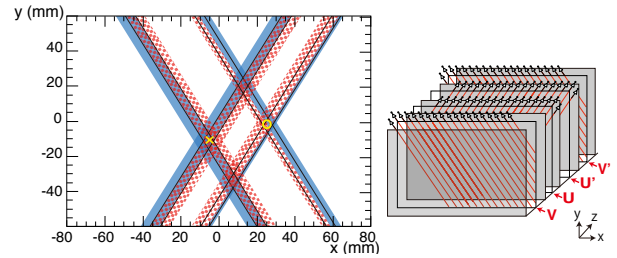
Figure 1: Example of an event snapshot. The MWDC at F6 consists of 4 planes (U($30°$)-U'($30°$)-V($60°$)-V'($60°$)). Solid lines represent hit wires. Blue solid and red meshed bands represent the drift length of U(U') and V(V') planes, respectively. We can track the position (indicated by yellow circle) if there are 4 candidates. The yellow cross denotes the particle in the next bunch of triggered particle.

We developed a new analysis framework that contains information of multi particles arranged in a bunch structure as a new dimension. Previous frameworks have assumed that one trigger event corresponds to only one particle. By combined with the new framework and multi-hit TDC, we identified beam bunches containing reaction-induced ^{8}He beam. This method helped to increase the number of usable events for missing-mass analysis by 12 %. Such multi-particle events often provoke wrong hit positions by the MWDC, since the drift time of MWDC is larger than the RF period of the beam. To reduce miss tracking of MWDC, we use the sum of drift time in two planes half shifted to each other, which is constant for one particle hits. We are able to determine hit positions of both two particles when their distance is more than a half cell size of MWDC (4.5 mm). By using this condition, we improved the number of tracking events

by about 10 %.

At the final focal plane of the SHARAQ spectrometer, two-alpha events can be tracked using cathode readout drift chamber [4] (CRDCs). We identified approximately about a hundred candidate events of the 4n system.
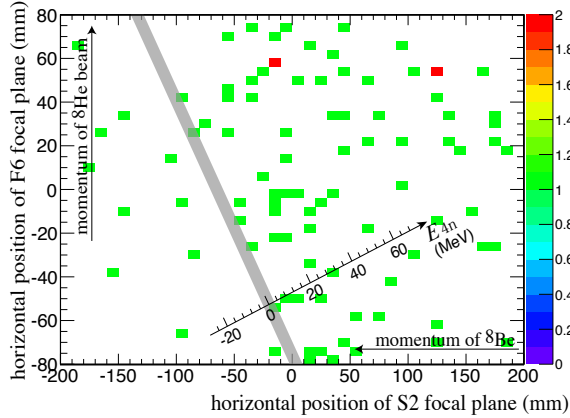
Figure 2: Correlation of candidate events between horizontal position of F6 and S2 focal plane which correspond to the momentum of ^{8}He beam and momentum of ^{8}Be ejectile respectively. Shaded line shows the threshold of 4n.

To identify 4n events, we selected events which satisfy the following conditions; 1) Tof measurement between secondary target and final focal plane plastic scintillator and energy loss at the plastic scintillator, 2) rejection of events of multi-particle in one-bunch, 3) identification of a true track which made by a trigger event, 4) identification of 2α particles at final focal plane in coincidence, 5) confirmation of the position of the target and 6) other fiducial cuts.

We identified about a hundreds of events as candidate of 4n events, including backgrounds which correspond to about 150 nb as total cross section. Figure 2 shows the correlation of candidate events between the horizontal position of F6 and S2 dispersive focal plane which correspond to a momentum of ^{8}He beam and a momentum of ^{8}Be ejectile respectively. Shaded line correspond to the threshold of 4n (excitation energy of 4n: $E_{4n} = 0$ MeV). For the energy calibration we used a known peak of ^{8}He(p,n)^{8}Li reaction and Bρ scaling of the SHARAQ spectrometer. Uncertainty of the calibration still has about ±3 MeV (RMS) which correspond to a width of gray shaded line. The missing mass spectrum can be obtained by projecting diagonally along the $E_{4n} = 0$ MeV line. Since the number of events per unit area above the line of the threshold are larger than below, reasonable correlation was obtained between the momentum of ^{8}He beam and ^{8}Be ejectile while there are still unphysical events below the 4n threshold. Further analysis is now in progress. We try to select the interested events by impose the kinematical condition of the reaction.

References

[1] F. Marques *et al.*: Phys. Rev. **C 65**, 044006 (2002)
[2] S. Pieper: Phys. Rev. Lett. **90**, 252501 (2003)
[3] K. Kisamori *et. al.*: CNS Ann. Rep. 2010 (2012)
[4] K. Kisamori *et. al.*: Accelerator Progress Rep. **46** (2013)

Study of spin-dipole response of ^{4}He in time-like region by using (^{8}He,^{8}Li$^*(1^+)$) reaction

H. Miya, S. Shimoura, K. Kisamori, M. Assié[a], H. Baba[b], T. Baba[c], D. Beaumel[b], M. Dozono[b], T. Fujii, N. Fukuda[b], S. Go, F. Hammache[b], E. Ideguchi[d], N. Inabe[b], M. Ito[e], D. Kameda[b], S. Kawase, T. Kawabata[c], M. Kobayashi, Y. Kondo[f], T. Kubo[b], Y. Kubota, C. S. Lee, Y. Maeda[g], H. Matsubara[b], S. Michimasa, K. Miki[d], T. Nishi[h], M. Kurata-Nishimura[b], S. Ota, H. Sakai[b], S. Sakaguchi[i], M. Sasano[b], H. Sato[b], Y. Shimizu[b], H. Suzuki[b], A. Stolz[j], M. Takaki, H. Takeda[b], S. Takeuchi[b], A. Tamii[d], H. Tokieda, M. Tsumura[c], T. Uesaka[b], K. Yako, Y. Yanagisawa[b], and R. Yokoyama

Center for Nuclear Study, Graduate School of Science, the University of Tokyo
[a]*Institut de Physique Nucléaire, Orsay, France*
[b]*RIKEN (The Institute of Physical and Chemical Research)*
[c]*Department of Physics, Kyoto University*
[d]*Research Center for Nuclear Physics, Osaka University*
[e]*Cyclotron and Radioisotope Center, Tohoku University*
[f]*Department of Physics, Tokyo Institute of Technology*
[g]*Department of Applied Physics, University of Miyazaki*
[h]*Department of Physics, the University of Tokyo*
[i]*Department of Physics, Kyushu University*
[j]*National Superconducting Cyclotron Laboratory, Michigan State University, USA*

We performed the exothermic charge-exchange (CE) reaction of (^{8}He, ^{8}Li) at the RIKEN RIBF facility by using the BigRIPS, the High-Resolution Beamline, and the SHARAQ spectrometer [1, 2]. Missing mass spectra in the ^{4}He(^{8}He, ^{8}Li$^*(1^+)$) reactions were measured at the beam energy of 190 MeV/nucleon. This experiment aimed at studying spin-isospin response, especially spin-dipole transition in ^{4}He by RI-beam induced CE reaction. In order to identify ^{8}Li$^*(1^+)$, we measured the 980-keV γ-ray corresponding to the $1^+ \to 2^+$ transition in ^{8}Li. The coincident detection of ^{8}Li and the 980-keV γ-ray is an evidence of the occurrence of the CE reaction. The CE reaction is possible to reach the highly excited state at the condition of the time-like region.

Figure 1 shows the schematic view of the BigRIPS, the High-Resolution Beamline, and the SHARAQ spectrometer. A ^{8}He beam at 190 MeV/nucleon was produced via the projectile fragmentation reaction of the ^{18}O beam at 230 MeV/nucleon with a Be target at F0. The intensity of ^{8}He was approximately 2×10^6 cps at S0, where the secondary targets of liquid ^{4}He were installed. The target thicknesses of the liquid ^{4}He were 120 mg/cm^2. The liquid ^{4}He target was made using the CRYPTA system. [3] The beam trajectory was measured by μ-hodoscope [4] and low-pressure multi-wire drift chambers [5] (LP-MWDCs) in the BigRIPS and the High-Resolution Beamline. The μ-hodoscope was installed at F3 to measure beam position whose spot size is as small as 1 cm (FWHM). The momentum of ^{8}He was measured at F6, which is the momentum dispersive focal plane. At S0, the beam position and incident angle into the targets were determined. The scattered ^{8}Li was momentum analyzed with the SHARAQ spectrometer and detected by cathode readout drift chambers (CRDCs) [6] at S2. The 980-keV γ-rays emitted from ^{8}Li were detected by the NaI(Tl) detector array (DALI2 [7]) located near the secondary target.
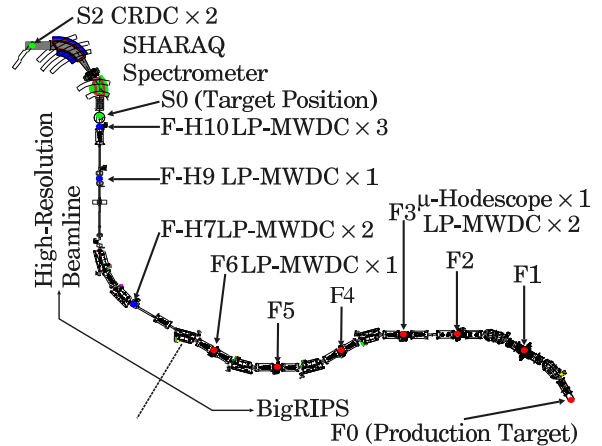
Figure 1: Schematic view of BigRIPS, High-Resolution Beamline, and SHARAQ Spectrometer.

The secondary RI beam has momentum distribution. In order to perform high-resolution missing mass spectroscopy with the RI beam, measurement of the beam momentum (δ) of incoming and outgoing particles at the target is required. At the momentum-dispersive focal planes, δ is correlated with the beam trajectory. In High-resolution achromatic transport mode, it is important to measure the trajectory, the horizontal position (x), at the BigRIPS-F6 and the SHARAQ-S2. δ couples with the beam transfer matrix elements of x and horizontal angle (a). The matrix elements should be measured to obtain the missing mass energy in the CE reaction. The ^{8}Li beam was transported to S2 for checking the matrix elements of $(x|x)$ and $(x|a)$ of the beamline and the SHARAQ spectrometer in the experiment.

Figure 2(a) shows the correlations of x_{S0} with x_{S2} for the momentum correction of the ^{8}Li beam. The five loci corre-
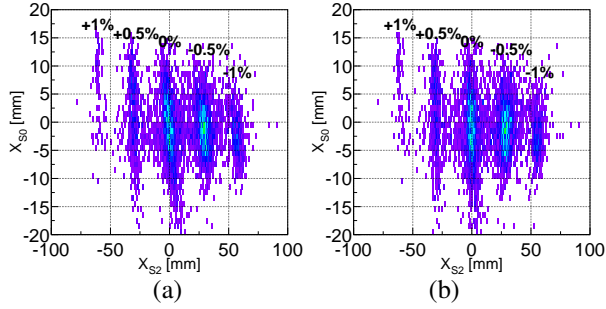
Figure 2: Correlation of x_{S0} with x_{S2} (a) before and (b) after correction.The five loci correspond to the particles with δ = -1%, -0.5%, ... ,1%, which were tagged at the BigRIPS-F6.

spond to the particles with $\delta = -1\%, -0.5\%, ...$,1%, which were tagged at F6. The inclinations of the loci indicate the matrix element of $(x|x)$. The difference in the inclinations for different δ's is due to the effect of the second-order matrix element of $(x|x\delta)$. This defference enables enabled us to obtain the δ at high resolution by correcting the correlation, as shown in Fig. 2(b). The matrix elements of $(x|a)$ and $(x|a\delta)$ were determined to correct the tilt of the focal plane. These higher-order matrix elements of the beamline at F6 were determined by checking the correlation with tagging the beam momentum at S2. The missing mass resolution was evaluated to be 3.2 MeV in FWHM by using the matrix elements and 4.6 MeV in FWHM before the correction.

Further analysis of the missing mass and angular distribution is now in progress.

References

[1] T. Uesaka *et al*.: Prog. Theor. Exp. Phys. (2012) 03C007.
[2] S. Michimasa *et al*.: Nucl. Instr. Meth. B **317**, 305-310 (2013).
[3] H. Ryuto *et al*: Nucl. Instr. Meth. A 555, 1-5 (2005).
[4] S. Ota *et al*.: CNS Ann Rep. 2011 (2013).
[5] H. Miya *et al*.: Nucl. Instr. Meth. B **317**, 710-713 (2013).
[6] K. Kisamori *et al*.: CNS Ann. Rep. 2011 (2013).
[7] T. Takeuchi *et al*.: Nucl. Instr. Meth. A **763**, 1-8 (2014).

Spin-isospin response of the neutron-rich nucleus ^{8}He via the (p, n) reaction in inverse kinematics

M. Kobayashi, K. Yako, S. Shimoura, M. Dozono[a], S. Kawase, K. Kisamori, Y. Kubota, C. S. Lee, S. Michimasa, H. Miya, S. Ota, H. Sakai[a], M. Sasano[a] and M. Takaki

Center for Nuclear Study, Graduate School of Science, University of Tokyo
[a]*RIKEN Nishina Center*

1. Introduction

(p, n) reactions at intermediate energies ($E > 100$ MeV) provide powerful tools to study spin-isospin responses in nuclei, in particular Gamow-Teller (GT) transitions. The GT giant resonance (GTGR), which exhausts a large part of the model independent GT sum rule, is a representative collective mode of excitation.

A key feature of (p, n) reactions at intermediate energies is that there is a close proportionality between cross sections at $0°$ and the GT transition strengths $B(GT)$ [1]. Since, in contrast to β-decay, charge-exchange reactions do not suffer from any Q-value limitation, they can be used to study transitions to excited states at relatively high energies, including GTGR, as well as the low-lying states.

While numerous (p, n) studies have been performed on stable nuclei, high-intensity radioactive isotope (RI) beams have recently made it possible to measure (p, n) reactions on unstable nuclei [2].

In the present work, we focused on the neutron-rich nucleus ^{8}He, which has the largest neutron-to-proton ratio among all known particle-stable nuclei ($N/Z = 3$), to study the spin-isospin correlation in neutron-rich light nuclei. In the past, some information on the spin-isospin responses of ^{8}He has been reported from β-decay studies (for example [3,4]).

2. Experiment

Measurement of the ^{8}He$(p, n)^8$Li reaction in inverse kinematics was performed at the RIKEN RI Beam Factory.

Figure 1 shows the experimental setup around the secondary target, which was 0.39-g/cm^2 polyethylene. The neutron detector array WINDS (Wide-angle Inverse-kinematics Neutron Detectors for SHARAQ) [5] , which is an array of plastic scintillators, surrounded the secondary target at a distance of 180 cm. A superconducting triplet quadrupole magnet was installed between the focal plane FH9 and the downstream one FH10.

In the present work, missing mass spectroscopy was employed. Excitation energies (E_x) of ^{8}Li and the scattering angle in the center-of-mass frame (θ_{cm}) were constructed from measurements of kinetic energies (T_n) and scattering angles in the laboratory frame (θ_{lab}) of neutrons. T_n was determined by measuring the neutron time-of-flight, and θ_{lab} was determined from the location of the scintillator bar in which the scattered neutron was detected.

To improve the signal-to-noise ratio, the residual nucleus from the ^{8}He(p, n) reaction was detected by auxiliary beam line detectors, i.e., the plastic scintillator and Low-Pressure Multi-Wire Drift Chambers [6] at FH10, in coincidence with detection of neutrons in WINDS. In the present experiment, Li isotopes, including the residual nucleus ^{8}Li and its decay product ^{7}Li, were tagged.
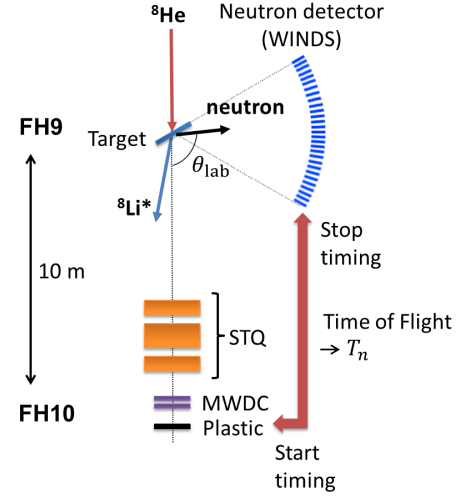
Figure 1: Experimental setup around the secondary target.

3. Results

Double differential cross sections for the ^{8}He$(p, n)^8$Li reaction at excitation energies of 0–20 MeV and neutron energies of 2.0–4.4 MeV, which correspond to momentum transfers of $q = 0.31$–0.46 fm^{-1}, respectively, were obtained. Figure 2 provides an excitation energy spectrum for $T_n = 2.6$–3.2 MeV. In this spectrum, two peaks were observed at $\sim$1 MeV and $\sim$8 MeV. The lower-energy peak corresponds to the first excited 1^+ state in ^{8}Li located at 0.98 MeV, which is known to have GT strength of $B(GT) = 0.24$ according to a previous β-decay study [3].
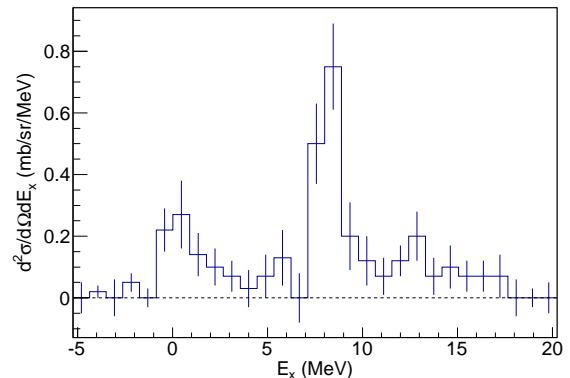
Figure 2: (Preliminary.) Double differential cross sections for neutron energies of $T_n = 2.6$–3.2 MeV.

The angular distributions of the differential cross sections for the ~ 1 MeV and ~ 8 MeV peaks are displayed in Fig. 3, where the transmission efficiencies of the Li isotopes between the target position and detection focal plane have

been corrected for. The transmission efficiencies were evaluated by a Monte Carlo simulation.
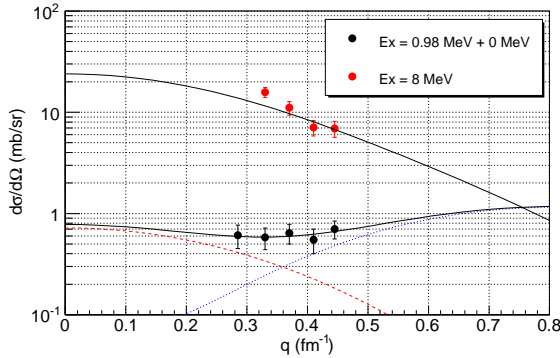
Figure 3: (Preliminary.) Angular distributions of the measured cross section for the 0.98-MeV (black) and the 8-MeV (red) peaks. The error bars represent statistical errors only.

The angular distributions were compared to distorted wave impulse approximation (DWIA) calculations. The angular distribution of the peak at $\sim$1 MeV, which displays a flat distribution, was reproduced well by a sum of the distributions from the 0.98-MeV state ($J^\pi = 1^+$) and the ground state ($J^\pi = 2^+$). The $B(GT)$ value for the 8-MeV state was derived using the extracted cross sections at $q = 0$ and the known $B(GT)$ value for the 0.98-MeV state. The obtained GT strength for the neutron decay channel of the 8-MeV state was $B(GT) = 8 \pm 4$, which is $\sim$70% of the sum rule value of $3(N - Z) = 12$.

β-decay studies of ^{8}He provided the excitation energy and $B(GT)$ values for the GT state in ^{8}Li from R-matrix theory, but these values have not been fixed [4, 7–9]. It is noted that only the triton emission channel of the GT state was considered in obtaining these values; Borge *et al.* [4] measured a β-delayed triton branch, and obtained $B(GT) = 5.18$ at the excitation energy of $E_x = 9.3$ MeV. Figure 4 shows the decay scheme of ^{8}He, including the resonance state observed in the present measurement as well as excited states observed in previous β-decay studies. It is not clear whether the GT state observed in the present measurement and that observed in the β-decay measurement are the same. We conclude that the observed state with large transition strength at ~ 8 MeV is the GTGR, which is the first direct observation of the GTGR in ^{8}He.
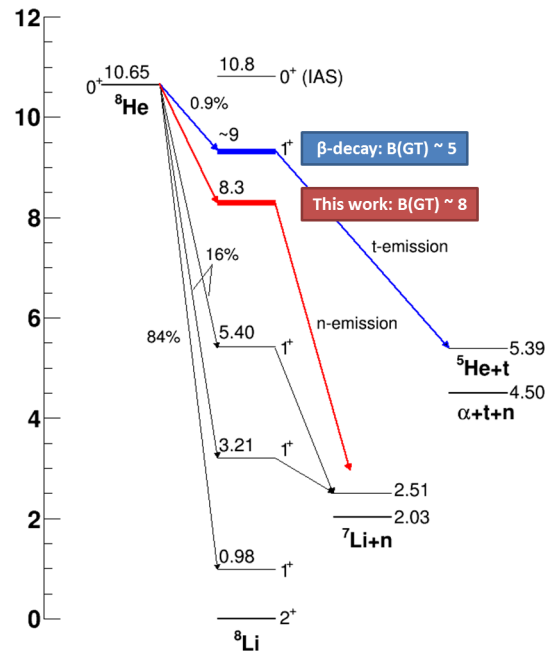
Figure 4: Decay scheme of ^{8}He. The excited state observed at ~ 8 MeV in the present (p, n) measurement is shown as well as those observed in the previous β-decay studies [10].

References

[1] T.N. Taddeucci *et al.*, Nucl. Phys. A **469** (1987) 125.
[2] K. Yako *et al.*, RIKEN Accel. Prog. Rep. **45** (2012) v.
[3] T. Björnstad *et al.*, Nucl. Phys. A **366** (1981) 461.
[4] M.J.G. Borge *et al.*, Nucl. Phys. A **560** (1993) 664.
[5] For example, K. Yako *et al.*, RIKEN Accel. Prog. Rep. **45** (2012) 137.
[6] H. Miya *et al.*, Nucl. Instr. Meth. B **317** (2013) 710 .
[7] M.J.G. Borge *et al.*, Nucl. Phys. A **460** (1986) 373.
[8] F.C. Barker, E.K. Warburton, Nucl. Phys. A **487** (1988) 269.
[9] F.C. Barker, Nucl. Phys. A **609** (1996) 38.
[10] D.R. Tilley *et al.*, Nucl. Phys. A **745** (2004) 155.

New type of spectroscopy via heavy–ion double charge exchange (^{12}C, ^{12}Be(0_2^+)) reaction

M. Takaki, T. Uesaka[a], S. Shimoura, N. Aoi[b], M. Dozono, S. Gotanda[c], T. Hashimoto[b], Y. Kanaya[c], T. Kawabata[d], K. Kisamori, M. Kobayashi, Y. Kubota, Y. Maeda[c], M. Matsushita, S. Michimasa, K. Miki[b], E. Milman[a], S. Ota, M. Sasano[a], A. Tamii[b], M. Tsumura[d], and J. Zenihiro[a]

Center for Nuclear Study, Graduate School of Science, University of Tokyo
[a]*RIKEN (The Institute of Physical and Chemical Research)*
[b]*Research Center for Nuclear Physics, Osaka University*
[c]*Department of Applied Physics, Miyazaki University*
[d]*Department of Physics, Kyoto University*

One of the most interesting features in atomic nuclei is the variety of spin and isospin responses. The Gamow–Teller (GT) transition is the simplest spin–isospin response within one-phonon excitations, and it has been well studied. In contrast, data on multi-phonon excitations have been scarce. The double GT giant resonance (DGTGR) [1] is the simplest two-phonon excitation mode. However, DGT-GRs have not been observed so far. The discovery of the DGTGR is an essential step in extending the research of the spin–isospin responses to multi-phonon space. Another interest for studying DGTGRs relates to its relevance in neutrino physics; the DGT transition is induced by the same transition operator as the $\beta\beta$-decay is , *i.e.*, $\sigma\tau\sigma\tau$. However, the $\beta\beta$-decay has quite small DGT strength. A major part of the DGT strength lies in highly excited states in the DGTGR. A promising spectroscopic method to search for DGTGRs is heavy-ion double charge exchange (HIDCX) reactions, which can induce two-phonon excitations with spin and isospin transfer by two units.

In 2011, we conducted a HIDCX ^{12}C(^{18}O, ^{18}Ne)^{12}Be reaction experiment and found a large cross section of 1.5 μb/sr for the second 0^+ (0_2^+) state in ^{12}Be at $0°$ [2]. This is probably because all the initial ^{12}C($0_{\text{g.s.}}^+$), intermediate ^{12}B($1_{\text{g.s.}}^+$), and final ^{12}Be(0_2^+) states are dominated by a $0\hbar\omega$ configuration [3–5]. This led us to a new idea to use the (^{12}C, ^{12}Be(0_2^+)) reaction as a tool to investigate DGTGRs. In this method, the excitation energies of target nuclei are measured using a missing mass technique. Several final states in ^{12}Be can degrade the signal-to-noise ratio of an observed spectrum in the method. The key of this method is to avoid the contamination by tagging the two 511–keV γ-rays emitted back-to-back from the e^+e^- decay with the mean life-time of 331 ns [6]. In order to demonstrate the feasibility of the delayed γ-ray tagging method, we performed the HIDCX ^{18}O(^{12}C, ^{12}Be(0_2^+))^{18}Ne reaction measurement using the Grand Raiden (GR) spectrometer at RCNP, Osaka University. The primary ^{12}C beam at 100A MeV bombarded a 20-mg/cm^2 H$_2$^{18}O ice target. The momenta of outgoing particles were analyzed using GR. The two 511–keV γ-rays from ^{12}Be(0_2^+) were detected using a NaI(Tl) array surrounding a plastic-scintillator stopper at the GR focal plane.

In the analysis, we require detection of 511-keV γ-rays emitted back-to-back and within 10 ns time difference for the (^{12}C, ^{12}Be(0_2^+)) event selection. Figure 1 shows the excitation energy spectra of ^{18}Ne. The peak of the spectrum without the γ-ray tagging, which originates from the ^{18}Ne ground state, is rather broad and has a tail. The broad-

ening is probably due to contributions from different final states in ^{12}Be, and the tail originates from accidental coincidence events of ^{9}Li and ^{6}He. On the other hand, in a spectrum with γ-ray tagging, the peak is narrower, and the background has mostly vanished. The energy resolution was $\sim$3 MeV mainly limited by the energy-loss difference in the target, and thus the difference between the peak positions of the two spectra is within the resolution. More
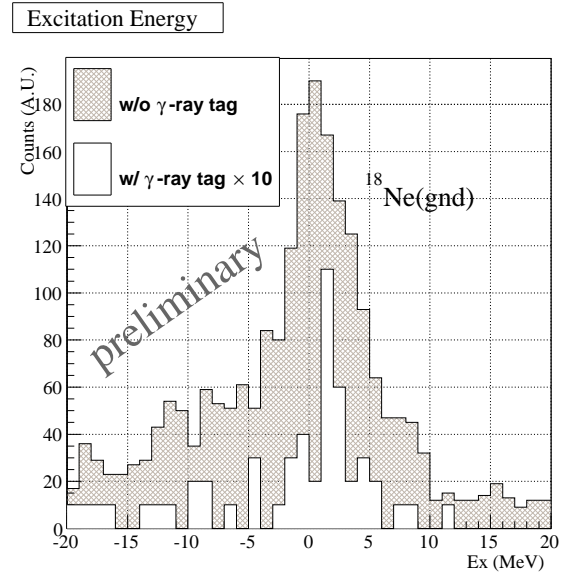
Figure 1: Excitation energy spectra of ^{18}Ne with or without γ-ray tagging. For the γ-ray tagged spectrum, detection efficiency of 10% is considered for the NaI(Tl) array.

convincingly, a time spectrum of observed two 511 keV γ-rays, shown in Fig. 2, exhibits a decay with a time constant of $\tau = 395^{+173}_{-92}$ ns which is consistent with the known life-time of ^{12}Be(0_2^+) (331 ns) reported in Ref. [6] within the error.

Now, we conclude the HIDCX (^{12}C, ^{12}Be(0_2^+)) reaction with the delayed γ-ray coincidence serves as a powerful probe to the DGTGR. Based on experiences obtained in the test experiment, we will be able to further optimize the detector setup and readout electronics, which will enable us to achieve a better signal-to-noise ratio.

Our next step is to apply this method to nuclei exhibiting $\beta\beta$-decay. An experimental proposal, which aims to
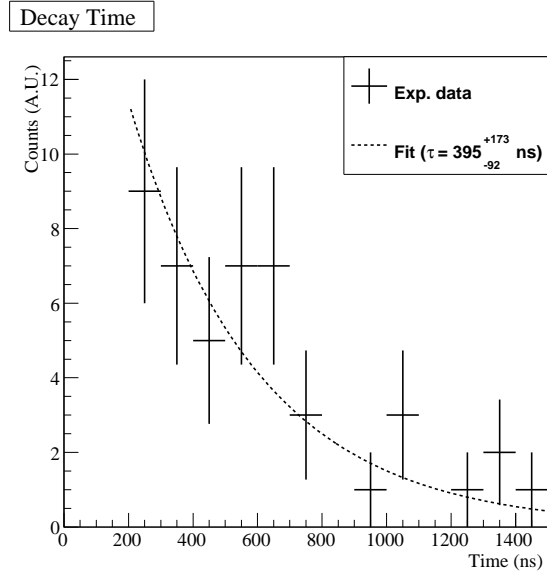
Figure 2: Timing spectrum of the NaI(Tl) detectors. Events with ^{12}Be were selected by the coincidence with the back-to-back 511 keV γ-rays emission.

observe the DGTGR in ^{48}Ti via the ^{48}Ca$(^{12}$C, ^{12}Be$(0_2^+))$ reaction, has been approved at RCNP. The experiment will be performed in FY 2014.

References

[1] D.C. Zheng, L. Zamick, N. Auerbach, Ann. of Phys. **197**, 343 (1990).

[2] M. Takaki *et al.*, RIKEN Accel. Prog. Rep. **46**, 29 (2013).

[3] F.C. Barker, J. Phys. G **2**, L45 (1976).

[4] H. Fortune and R. Sherr, Phys. Rev. C **74** (2006) 024301.

[5] R. Meharchant *et al.*, Phys. Rev. Lett. **108** (2012) 122501.

[6] S. Shimoura *et al.*, Phys. Lett. B **560** (2003) 31; *ibid* **654**, (2007) 87.

Superdeformation in ^{35}S

S. Go, E. Ideguchi[a], R. Yokoyama, M. Kobayashi, K. Kisamori, M. Takaki, H. Miya, S. Ota,

S. Michimasa, S. Shimoura, M. Niikura[b], T. Koike[c], T. O. Yamamoto[c], Y. Ito[d], J. Takatsu[d],

A. Yagi[d], H. Nishibata[d], T. Suzuki[a], K. Shirotori[a], Y. X. Watanabe[e], Y. Hirayama[e], M. Sugawara[f],

M. Koizumi[g], Y. Toh[h], T. Shizuma[g], A. Kimura[g], H. Harada[g], K. Furutaka[g], S. Nakamura[g],

F. Kitatani[g], Y. Hatsukawa[g], M. Oshima[g], I. Matea[h], D. Suzuki[h], D. Verney[h] and F. Azaiez[h]

Center for Nuclear Study, The University of Tokyo
[a]Research Center for Nuclear Physics, Osaka University
[b]Department of Physics, The University of Tokyo
[c]Department of Physics, Tohoku University
[d]Department of Physics, Osaka University
[e]High Energy Accelerator Research Organization
[f]Chiba Institute of Technology
[g]Japan Atomic Energy Agency
[h]Institute de Physiqué Nucleaire d'Orsay

Recently superdeformed states were systematically investigated in the A$\sim$40 nuclei, ^{36}Ar [1], ^{40}Ar [2], ^{40}Ca [3] and ^{44}Ti [4]. It was suggested that the $f_{7/2}$ intruder orbitals play an important role for superdeformation in A$\sim$40 since the SD-shell gaps would be caused by the crossing $f_{7/2}$ and $d_{3/2}$ orbitals. In the lighter mass region, a superdeformed state in ^{32}S has been studied by various theoretical models [5–8], though it has not been observed experimentally. Investigations of the orbitals responsible in this region are of importance to verify the existence of superdeformed states in ^{32}S. Especially, the spin-parity of superdeformed band heads in odd-mass isotopes gives direct information about involved orbital for the large deformation. with superdeformation. An odd-mass sulfur isotope, ^{35}S is a good candidate to study the role of the $f_{7/2}$ orbital since a large gap at $N = 20$ would be caused by $3/2^-$[321] originated from the $f_{7/2}$ orbital and $1/2^+$[200] from the $d_{3/2}$ orbital (see Woods-Saxon orbitals in Ref. [3]).

The high-spin states in ^{35}S were investigated using a ^{26}Mg(^{18}O, $2\alpha 1n$)^{35}S fusion-evaporation reaction at the Tandem-ALTO facility of Institut de Physique Nucleáire d'Orsay. The optimal ^{18}O beam energy was selected to be 80 MeV. The energy was determined by comparing the ratio of the observed transitions from high-spin states to those from low-spin states in ^{35}S among a set of measurements using 70, 80, 95 and 110 MeV ^{18}O beams in the JAEA Tokai Tandem Accelerator [9]. A stack of self-supporting ^{26}Mg foils of 0.5 mg/cm^2 each was used as the target. Charged particles such as protons and alpha particles evaporated from the compound nucleus were detected by an array of segmented silicon detectors, Si-Ball [10]. The signals from Si-Ball were successfully used to select the reaction channels with 2α-emission. The germanium detector array ORGAM, based on the EUROGAM [11] coaxial HPGe detectors, was employed for the γ-ray detection. A total of 13 detectors was installed at 5 different angles, which enabled us to measure the angular distribution of the γ rays.

The obtained γ-ray spectrum is shown in Fig 1. The peaks labeled with the triangles at 732-, 1576-, 2421- and 2869-keV are newly observed transitions in the present work. The other energies of γ rays were consistent with the previous experimental result [12]. γ-ray coincidence analysis, angular correlation analysis using Angular Distribution from Oriented states (ADO ratio [13]), and the measurement of the linear polarization of γ rays at CYRIC [14] were used to deduce the spin-parity of the levels. As a result, the high-spin levels up to 19/2 were identified (see Fig. 2).
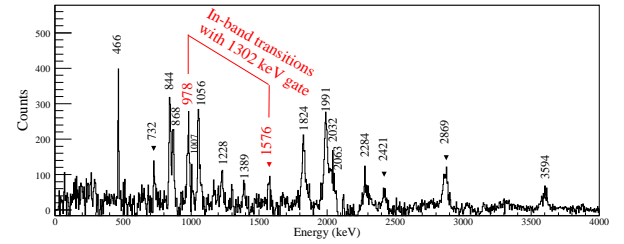
Figure 1: γ-ray energy spectrum gated on a 1302-keV transition. The 1576-, 1302- and 978-keV transitions belong to the same band transition. The peaks labeled with the triangles are new transitions of ^{35}S.

The relative intensities indicate the band structure from $19/2_1^-$ at 8756 keV to $7/2_3^-$ at 4900 keV. The 1302-keV transition from $15/2^-$ to $11/2_3^-$ states was observed while the direct transitions from the $15/2^-$ level to the $11/2_{1,2}^-$ levels were not observed in spite of the dominance of higher energy transitions expected from Weisskopf estimates. In addition, the 978-keV transition from $11/2_3^-$ to $7/2_3^-$ was observed while the transition from $11/2_3^-$ to $7/2_1^-$ was not. These facts imply that the transitions, 1576-, 1302- and 978-keV, from $19/2_1^-$ at 8756 keV to $7/2_3^-$ at 4900 keV belong to the same band.

The high-collectivity of the band is indicated by the half-life of the in-band transition. The half-life of the 1576-keV transition was determined to be 25^{+26}_{-23} fs from the amount of the residual Doppler shift. The half-life was deduced from the comparison with Monte-Carlo simulations considering the velocity of the fusion product in the target [15]. The velocities were calculated by the stopping power of the target [16, 17] and the kinematics of the fusion-evaporation reaction. Since the no feeding state was observed in the experiment, the feeding effect was negligible. The obtained half-life is 340 times shorter than the Weisskopf estimate, which means that the transition has collective character.

[17] E. K. Warburton *et al.*, Phys. Rev. C **40** (1989) 2823.
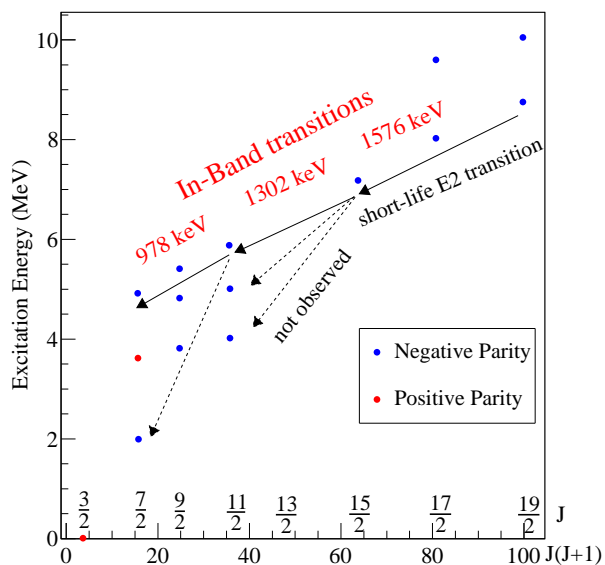
Figure 2: $J(J+1)$ vs. level energy for ^{35}S. The red and blue points are positive and negative parity states, respectively. The short-life E2 transition from $19/2_1^-$ to $15/2^-$ was observed and the relative intensities from $15/2^-$ to $11/2_3^-$ and $11/2_3^-$ to $7/2_3^-$ characterize the band structure of ^{35}S.

These experimental facts indicate that the negative-parity band from $19/2_1^-$ to $7/2_3^-$ has superdeformed band structure. However, the superdeformed band head which is expected to be $K^\pi = 3/2^-$ by the down-sloping $3/2^-[321]$ of $f_{7/2}$, was not observed in this study. The possible reason is that the intensity of the intra-band transition from $7/2^-$ to $3/2^-$ is not so strong due to the other paths of the transition to the low-spin levels. Further study with increased statistics would be important to identify the band head $3/2^-$ and higher spin states in the band. It will enables us to discuss the superdeformed shell structure in more detail.

References

[1] C. E. Svensson *et al.*, Phys. Rev. Lett. **85** (2000) 2693.
[2] E. Ideguchi *et al.*, Phys. Rev. Lett. B **686** (2010) 18.
[3] E. Ideguchi *et al.*, Phys. Rev. Lett **87** (2001) 222501.
[4] C. D. O'Leary *et al.*, Phys. Rev. C **61** (2000) 064314.
[5] R. K. Sheline *et al.*, Phys. Lett. B **41** (1972) 115.
[6] M. Girod *et al.*, Phys. Rev. C **27** (1983) 2317.
[7] J. Brenneisen Z. Phys. A **357** (1997) 377.
[8] P. G. Zint *et al.*, Phys. Lett. B **58** (1975) 269.
[9] S. Go *et al.*, JAEA-Tokai Tandem Annual Report 2012 (2012) 13.
[10] T. Kuroyanagi *et al.*, Nucl. Instr. and Meth. A **316** (1992) 289.
[11] C. W. Beausang *et al.*, Nucl. Instr. and Meth. A **313** (1992) 37.
[12] S. Aydin *et al.*, Phys. Rev. C **89** (2013) 014310.
[13] M. Piiparinen *et al.*, Nucl. Phys. A **605** (1996) 191.
[14] E. Ideguchi *et al.*, CNS Ann. Rep. 2010 (2010).
[15] S. Go, Ph. D. thesis, University of Tokyo (2014).
[16] J. F. Ziegler, Particle Interactions with Matter.

Excitation function measurements to investigate high-spin states of A∼40 nuclei

E. Ideguchi, T. Ishigaki[a], D. Suzuki[b], R. Yokoyama[c], K. Kobayashi[d], I. Matea[b], S. Michimasa[c],
S. Momiyama[e], M. Niikura[e], S. Shimoura[c], H. Suzuki, Mn. Tanaka, D. Verney[b], T. Yamamoto, and
Y.D. Fang

Research Center for Nuclear Physics, Osaka University
[a]*Department of Physics, Osaka University*
[b]*Institut de Physique Nucleaire, IN2P3-CNRS, Universite Paris-Sud*
[c]*Center for Nuclear Study, Graduate School of Science, University of Tokyo*
[d]*Department of Physics, Rikkyo University*
[e]*Department of Physics, University of Tokyo*

After the systematic investigations of superdeformed (SD) structure in various mass regions [1], a new 'island' of SD nuclei was found in A∼40 region (i.e., ^{36,40}Ar [2, 3], ^{40}Ca [4, 5], ^{44}Ti [6]). These nuclei are magic or near magic systems whose ground state have a spherical shape. However, in the excited states, these nuclei show strong collectivity after the cross-shell excitations involving both the sd and pf shells and the superdeformed structure emerges.

Among these A∼40 SD nuclei, high-spin level structure in ^{44}Ti was previously studied by C.D. O'Leary *et al.* [6] and the rotational band structure built on the 0_2^+ level up to 12^+ state was identified. It was interpreted as a SD band with 8p-4h configuration, but the size of deformation was not experimentally determined. By the life time measurement using the Doppler shift attenuation method, its transition quadrupole moment can be measured and the size of deformation will be deduced. In addition, the observation of higher spin levels above 12^+ level will further elucidate the properties of SD structure such as a role of $g_{9/2}$ intruder orbitals. Therefore, it is important to populate high-spin states of ^{44}Ti and deduce life times of excited levels.

Figure 1: Excitation function of ^{24}Mg + ^{24}Mg fusion-evaporation reaction calculated by the statistical model code PACE4 [7].

In order to examine the SD structure of ^{44}Ti, we plan to perform an in-beam gamma-ray spectroscopy experiment using ^{24}Mg + ^{24}Mg fusion-evaporation reaction. The choice of beam energy should be optimized to maximize the production cross section. According to the statistical model calculation (PACE4 [7]) as shown in Fig. 1, the cross sec-

tion to populate ^{44}Ti in the ^{24}Mg+^{24}Mg fusion-evaporation reaction is gradually increasing as a function of ^{24}Mg beam energy from 80 to 110 MeV region. Among the other evaporation channels, ^{39}K and ^{45}Ti will be strongly populated. In order to examine the population of A∼40 nuclei in the ^{24}Mg+^{24}Mg reaction, an excitation function measurement was performed.

The experiment was performed at the ALTO facility of Institut de Physique Nucleáire d'Orsay. The ^{24}Mg beam was extracted as a ^{24}MgH$^-$ molecule to inject the tandem accelerator, and the positive ions of ^{24}Mg were accelerated after the carbon stripper at the terminal. In order to avoid the possible contaminant of ^{12}C^{4+} ions, which has the same A/q values of ^{24}Mg^{8+} ions, the charge state of 7^+ was selected for the ^{24}Mg beam. For the excitation function measurements, the beam energies of 84, 96, 104 MeV were used. A ^{24}Mg target of 0.5 mg/cm^2 with Pb backing of 13 mg/cm^2 was used. The γ rays were measured by using the Compton suppressed Ge detector array, ORGAM, based on the EUROGAM coaxial HPGe detectors [8]. A total of 17 coaxial detectors and 2 clover type Ge detectors were used. The charged particles emitted in the reaction were measured by using the array of silicon detectors, Si-Ball [9].

Figure 2 shows the measured γ-ray energy spectra for three different beam energy settings. The peak at 1369 keV, which corresponds to the 2^+ to 0^+ transition in ^{24}Mg, is due to the target Coulomb excitation. The γ-ray energy peak at 2813 keV, which corresponds to the low-lying transition of ^{39}K as one of the strongest channels, was observed. The relative intensity of the 2813 keV peak is increasing with changing the beam energy from 84 to 104 MeV. Other γ-ray peaks associated with the ^{24}Mg + ^{24}Mg reaction were not clearly observed. The intensity of 2813 keV peak was relatively weaker than the other intense peaks observed in the spectra. The origin of these γ peaks were examined by the γ-γ coincidence analysis and attributed to ^{35}Cl (filled circle), ^{36}Cl (open circle), ^{33}S (filled diamond), ^{35}P (filled square), ^{29}S (open square), ^{34}S (filled spade), and ^{30}K (open triangle). These nuclei have lower Z numbers than those estimated by the PACE4 calculation and they cannot be populated strongly in the ^{24}Mg+^{24}Mg reaction. This may indicate the contaminant of other ions of low Z particles in the beam such as carbon, nitrogen, and oxygen, and these particles reacted with the ^{24}Mg target to make above mentioned nuclei.

The relative intensities of the observed strong contaminants were plotted as a function of ^{24}Mg beam energies

Figure 2: Gamma-ray energy spectra for three different beam energy of ^{24}Mg, i.e. 84 MeV (a), 96 MeV (b), 104 MeV (c).

as shown in Fig. 3. In this plot, the ^{35}Cl peak observed at 84 MeV ^{24}Mg beam setting was normalized to 100. As shown in the figure, γ peaks associated with the ^{35}Cl nucleus strongly appeared in the spectra. One of the possible reactions to populate ^{35}Cl and other observed nuclei strongly is ^{14}N + ^{24}Mg reaction.
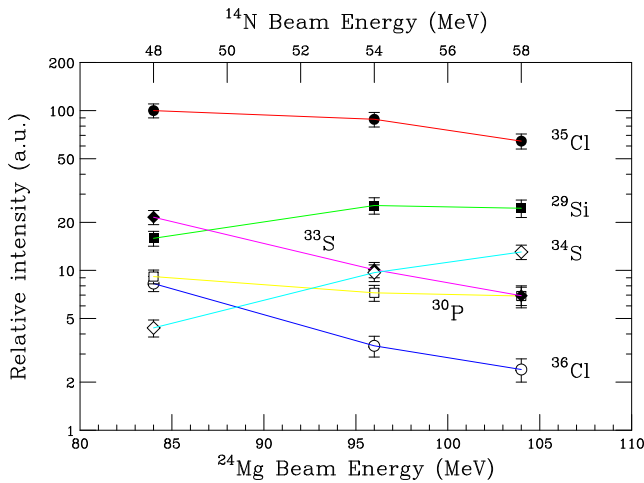
Figure 3: Relative γ yields of strong peaks appeared in three different beam energy settings. Corresponding beam energy of ^{14}N contaminant is also indicated on top of the figure.

Excitation function for the ^{14}N + ^{24}Mg reaction was estimated by the PACE4 [7] calculation as shown in Fig. 4. Dashed lines in the figure correspond to the three different energy setting of ^{24}Mg beam, i.e. 84, 96, and 104 MeV. By assuming the charge state of ^{14}N is 4^+ and the same Bρ values of ^{24}Mg^{7+} beams, energies of ^{14}N beam are estimated to be 47.0, 53.7, and 58.2 MeV, respectively. As shown in Fig. 4, the overall trend of observed contaminant are reproduced by the PACE4 calculation although ^{29}Si appears stronger than ^{35}Cl. This result may indicate the existence of ^{14}N contaminant in the ^{24}Mg beam.

Further analysis is now in progress.
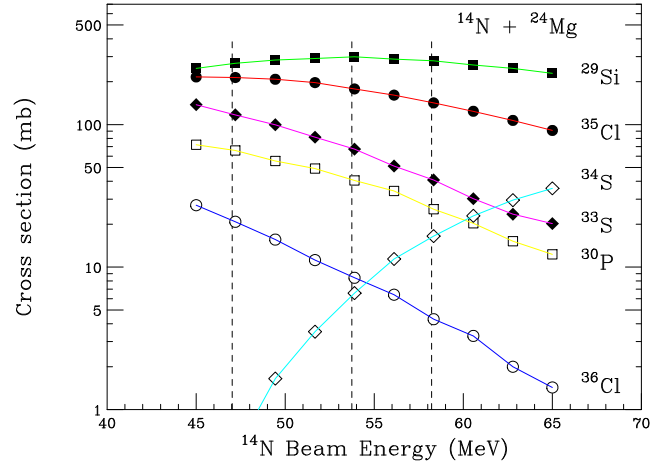
Figure 4: Calculated excitation function for ^{14}N+^{24}Mg reaction using PACE4 [7].

References

[1] B. Singh, R. Zywina, R.B. Firestone, Nucl. Data Sheets **97** (2002) 97.

[2] C.E. Svensson *et al.*, Phys. Rev. Lett. **85** (2000) 2693.

[3] E. Ideguchi *et al.*, Phys. Lett. **B** 686 (2010) 18.

[4] E. Ideguchi *et al.*, Phys. Rev. Lett. **87** (2001) 222501.

[5] C.J. Chiara *et al.*, Phys. Rev. C **67** (2003) 041303(R).

[6] C.D. O'Leary *et al.*, Phys. Rev. C **61** (2000) 064314.

[7] O.B.Tarasov, D.Bazin, Nucl. Instr. and Meth. B 204 (2003) 174.

[8] C.W. Beausang *et al.*, Nucl. Instr. and Meth. A 313 (1992) 37.

[9] T. Kuroyanagi *et al.*, Nucl. Instr. and Meth. A 316 (1992) 289.

Isomer study on neutron-rich Pm isotopes using EURICA at RIBF

R. Yokoyama, E. Ideguchi[a], G. Simpson[b], Mn. Tanaka[a], S. Nishimura[c], P. Doornenbal[c],
P.-A. Söderström[c], G. Lorusso[c], Z.Y. Xu[d], J. Wu[c,e], T. Sumikama[f], N. Aoi[a], H. Baba[c], F. Bello[g],
F. Brown[h,c], R. Daido[i], Y. Fang[i], N. Fukuda[c], G. Gey[b,c,j], S. Go, S. Inabe[c], T. Isobe[c], D. Kameda[c],
K. Kobayashi[k], M. Kobayashi, T. Komatsubara[l], T. Kubo[c], I. Kuti[m], Z. Li[e], M. Matsushita,
S. Michimasa, C.B. Moon[n], H. Nishibata[i], I. Nishizuka[f], A. Odahara[i], Z. Patel[c,o], S. Rice[c,o],
E. Sahin[j], L. Sinclair[c,p], H. Suzuki[c], H. Takeda[c], J. Taprogge[q,r], Zs. Vajta[m], H. Watanabe[s], and
A. Yagi[i]

Center for Nuclear Study, the University of Tokyo
[a]*Research Center for Nuclear Physics, Osaka University*
[b]*LPSC, UJF, INP Grenoble, CNRS/IN2P3*
[c]*RIKEN Nishina Center*
[d]*Department of Physics, the University of Tokyo*
[e]*Department of Physics, Peking University*
[f]*Department of Physics, Tohoku University*
[g]*Department of Physics, University of Oslo*
[h]*School of Computing Engineering and Mathematics, University of Brighton*
[i]*Department of Physics, Osaka University*
[j]*ILL, Grenoble*
[k]*Department of Physics, Rikkyo University*
[l]*Department of Physics, University of Tsukuba*
[m]*MTA Atomki*
[n]*Department of Display Engineering, Hoseo University*
[o]*Department of Physics, University of Surrey*
[p]*Department of Physics, University of York*
[q]*Instituto de Estructura de la Materia, CSIC*
[r]*Departamento de Fisica Teórica, Universidad Autónoma de Madrid*
[s]*Department of Physics, Beihang University*
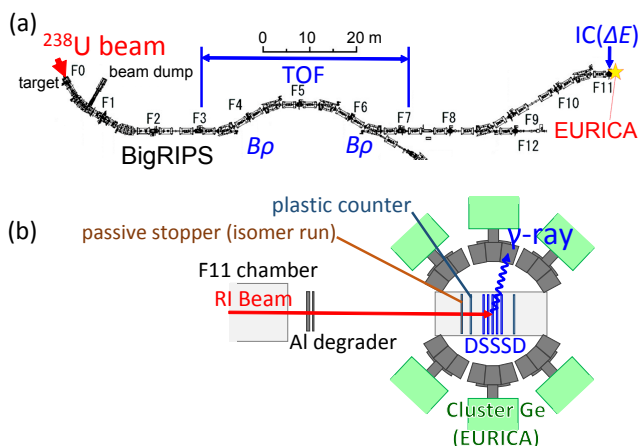
Figure 1: Schematic diagrams of the BigRIPS and ZeroDegree spectrometer beam line (a), and the stopper and detector setups at F11 (b). A passive stopper was installed in front of the WAS3ABi system only in the isomer runs.

Neutron-rich $Z \sim 60$ nuclei have been known to have large prolate deformation as shown by the systematics of excitation energies of first 2^+ states of even-even nuclei. (See FIG.1 of [1].) The deformed nuclei in this region have attracted much attention due to the existence of many quasi-particle K-isomers with μs half-lives. These isomers have been studied by delayed γ-ray measurements of spontaneous or neutron-induced fission of heavy nuclei [2, 3]. By compairing the experimental results with QPRM calculations, they obtained information on the structure of single particle orbitals around Fermi surface. Isomer spectroscopy also provides information on the low-lying collective states of the ground state. The existence of K-isomers in large numbers of nuclides in this region enables systematic study on the development of deformation and single particle structure in highly neutron-rich nuclei.

In $N = 100$ isotones, $K^\pi = 4^-$ isomers have been systematically observed in $Z = 62$ to 68 [4,5] nuclei. Simillar K-isomers are expected in more neutron-rich ($Z < 62$) isotones. Such neutron-rich nuclei had not been studied well on their excited states due to the experimental difficulties in their production and identification. Systematic studies of quasi-particle states with lower-Z isotopes by isomer spectroscopy will give further insight to the development of single particle states in the neutron-rich deformed nuclei.

We have performed isomer and β-γ spectroscopy on neutron-rich $Z = 56$ to 61 isotopes at the RI Beam Factory at RIKEN Nishina Center. By using in-flight fission of 345 MeV/u ^{238}U beam at RIBF, it became possible to produce such neutron-rich nuclei with high production rates for the first time. The primary ^{238}U beam bombarded 4-mm thick Be production target. The typical intensity of the primary beam was ~ 7 pnA. Fission fragments were separated and identified in the BigRIPS in-flight separator [6]. The particle identification was carried out by measuring the
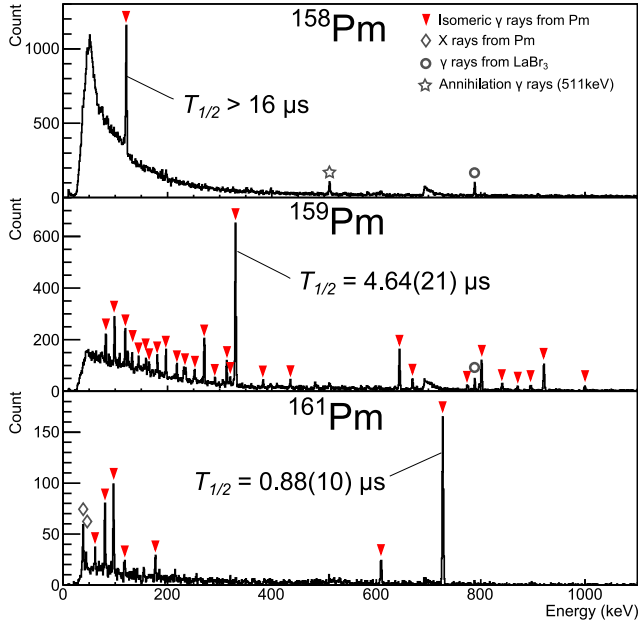
Figure 2: Preliminary γ-ray energy spectra of ^{158}Pm, ^{159}Pm and ^{161}Pm. The time windows of ^{158}Pm and ^{159}Pm are up to 5 μs and that of ^{158}Pm is up to 16 μs. Events close to the timing of the ion implantation are excluded. Half-lives of ^{159}Pm and ^{160}Pm are obtained from the 330 keV and 728 keV γ rays respectively. A γ-ray peak of ^{138}Ce is observed in the spectra of ^{158}Pm and ^{159}Pm. This originates in the activity of LaBr$_3$ detectors placed at vacant slot of the EURICA array, which is not mentioned in the text.

time-of-flight (TOF) and magnetic rigidity ($B\rho$) in the second stage of the BigRIPS and by measuring the energy loss (ΔE) in an ion chamber at the final focal plane, F11. The schematic view of the beam line is shown in Fig.1 (a). The TOF was obtained from the time difference between plastic scintillators at the F3 and F7 focal planes. The $B\rho$ value was obtained by the trajectory reconstruction from position and angular information measured by position-sensitive parallel plate avalanche counters (PPACs) at F3, F5 and F7. Detailed explanation of the particle identification at the BigRIPS is found in [7].

The measurement was conducted in two different stopper setups at F11. One was optimized for isomer spectroscopy by using a copper passive stopper in order to accept a wide range of nuclides with high implantation rates ~ 1 kHz. In the other setup, an active stopper WAS3ABi [8] which consists of five layers of Double-Sided-Silicon-Strip-Detectors (DSSSDs) with 40×60 strips was used in order to measure β-γ events. In the latter setup, the total implantation rate of ions was limited up to ~ 100 Hz.

The delayed γ rays from the implanted ions were detected by EURICA [9] array with 12-cluster Ge detectors. Each cluster consists of seven crystals that enable adding back Compton-scattered events in the neighbouring crystals. The total detection efficiency of the array for photons of 1332 keV was 8.4%. The energies and timigs of delayed γ rays were measured in a time window of 16 μs following the ion implantation for isomer spectroscopy. The detector setup at the F11 focal plane is shown in Fig.1 (b).

Figure 2 shows the delayed γ-ray spectra of neutron-rich Pm isotopes observed in this work. Half-lives of each γ ray were obtained by likelihood fitting of the timing spectrum

gated by the γ-ray energy with a function that consists of exponential decay and constant background. A single γ-ray peak was observed at 121 keV in ^{158}Pm. The half-life of this γ ray is much longer than the 16-μs time window. Seven γ rays were observed in ^{161}Pm. The half-lives obtained from each γ ray agree with each other within the errors, which means that only one isomeric state with microsecond-or-longer half-life is present. The weighted mean value of the half-life of ^{161}Pm was 0.89(6) μs. More than 30 delayed γ rays were observed in ^{159}Pm. The half-life of ^{159}Pm obtained from the most intense peak at 330 keV was 4.64(21) μs.

The obtained half-life of ^{161}Pm in this work is similar to those of $K^\pi = 4^-$ isomers in other $N = 100$ isotones. We expect that the isomer of ^{161}Pm also has the same two quasi-particle excitation of neutrons with a configuration of $\nu 7/2[633] \otimes \nu 1/2[521]$. Detailed analysis including relative intensities and coincidences between γ rays are being examined to construct decay schemes of the observed isomers. Analysis of β-decay events are also in progress. This may help understanding low-lying states of those nuclei. Results of these Pm isomers will give further information on the sigle particle and collective structures of neutron-rich nuclei in mass 160 region.

References

[1] R. F. Casten *et al.* Phys. Rev. Lett. **47** (1981) 1433.
[2] G. S. Simpson *et al.* Phys. Rev. C **80** (2009) 024304.
[3] G. S. Simpson *et al.* Phys. Rev. C **81** (2010) 024313.
[4] G. D. Dracoulis *et al.* Phys. Rev. C **81** (2010) 054313.
[5] S. Go *et al.* RIKEN Accel. Prog. Rep. **46** (2013) 182.
[6] T. Kubo *et al.* NIM B **204** (2003) 97.
[7] T. Ohnishi *et al.* J. Phys. Soc. Jpn. **79** (2010) 073201.
[8] S. Nishimura *et al.* Nucl. Phys. News **22** (2012) No.3.
[9] S. Nishimura *et al.* RIKEN Accel. Prog. Rep. **46** (2013) 182.

Isomer spectroscopy of neutron-rich $_{60}$Nd isotopes

Mn. Tanaka, E. Ideguchi, G. Simpson[a], R. Yokoyama[b], S. Nishimura[c], P. Doornenbal[c], G. Lorusso[c], P.-A. Söderström[c], Z. Xu[s], J. Wu[c,k], N. Aoi, H. Baba[c], F. Bello[d], F. Browne[c,e], R. Daido[f], Y. Fang[f], N. Fukuda[c], G. Gey[a,c,g], S. Go[b,c], N. Inabe[c], T. Isobe[c], D. Kameda[c], K. Kobayashi[h], M. Kobayashi[b], T. Komatsubara[i], T. Kubo[c] I. Kuti[j], Z. Li[k], M. Matsushita[b], S. Michimasa[b], C.-B. Moon[l], H. Nishibata[f], I. Nishizuka[m], A. Odahara[f], Z. Patel[c,n], S. Rice[n], E. Sahin[d], L. Sinclair[c,o], T. Sumikama[m], H. Suzuki[c], H. Takeda[c], J. Taprogge[p,q], Zs. Vajta[j], H. Watanabe[r], and A. Yagi[f]

Research Center for Nuclear Physics, Osaka University,
[a]*LPSC, Université Grenoble-Alpes, CNRS/IN2P3,* [b]*Center for Nuclear Study, The University of Tokyo,*
[c]*RIKEN Nishina Center,* [d]*University of Oslo,* [e]*The University of Brighton,* [f]*Department of Physics, Osaka University,*
[g]*ILL, 38042 Grenoble Cedex,* [h]*Department of Physics, Rikkyo University,* [i]*University of Tsukuba,*
[j]*MTA Atomki,* [k]*Peking University,* [l]*Hoseo University,* [m]*Department of Physics, Tohoku University,*
[n]*The University of Surrey,* [o]*University of York,* [p]*Instituto de Estructura de la Materia, CSIC,*
[q]*Universidad Autónoma de Madrid,* [r]*Beihang University,* [s]*Department of Physics, The University of Tokyo*

Prolate-deformed nuclei are found to appear in the neutron-rich part of the nuclear landscape around $Z = 60$ and beyond $N = 90$, after the systematic studies of excited states. In strongly deformed nuclei, quantum number K is known to be a good quantum number. Since transitions with large changes in K are suppressed, many nuclei in this region have isomeric states. In addition to the quadrupole deformation, appearances of higher-order deformations such as octupole and hexadecapole deformations have been predicted [1]; however, they are not yet understood well. Isomer spectroscopy is a useful method to gain information on such structures of these nuclei.

Neutron-rich $_{60}$Nd isotopes have been investigated by means of isomeric γ-ray spectroscopy. Such isotopes were produced by the in-flight fission of ^{238}U beam accelerated up to 345 MeV/u at RI Beam Factory in RIKEN Nishina Center, and were selected and identified by using the BigRIPS [2] separator. The identification of the nuclei was performed on the basis of the ΔE-TOF-$B\rho$ method, where ΔE, TOF, and $B\rho$ denote energy loss, time of flight and magnetic rigidity. These quantities were measured using an
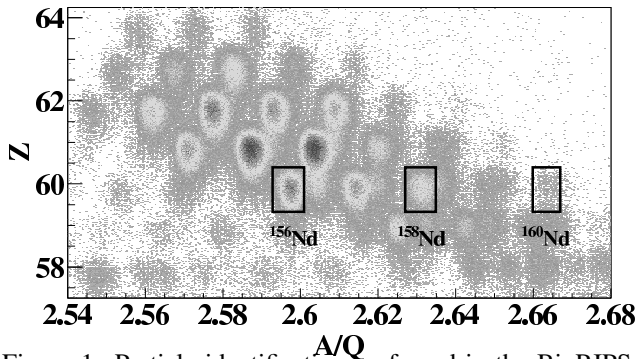
Figure 1: Particle identification perfomed in the BigRIPS separator.

ion chamber at the F11 final focal plane, plastic scintillation counters and PPACs at focal planes in the second stage, and calculated by the trajectory reconstruction method. This allows an event-by-event determination of atomic number Z and the mass-to-charge ratio A/Q. Fig. 1 shows the particle

identification plot for the ions of interest in our study.

The identified particles were implanted into passive and active stoppers. A passive stopper made of Cu was used for the measurement at a high count rate, while the WAS3ABi [3] active stopper consisting of five double-sided silicon strip detectors was used for the β-γ spectroscopy.

Delayed γ rays emitted by implanted particles were detected by a high-efficient γ-ray spectrometer, EURICA [4]. The spectrometer consists of 12 cluster germanium detectors, and each cluster detector consists of 7 crystals. By gating on the particle identification plot shown in Fig. 1, γ rays from the previously known 5^- K-isomeric state of ^{156}Nd [5] were observed as shown in Fig. 2 (a). To obtain half-life, time spectrum gated on each γ-ray energy peak was fitted as shown in Fig. 3 (a). The obtained half-life of the isomer in ^{156}Nd is consistent with the previously reported value.

In the same way, new isomeric states of heavier even-even isotopes, i.e., ^{158}Nd and ^{160}Nd were discovered as shown in Fig. 2 (b) and (c). The data taken with the passive and active stoppers were both included in these spectra. We have observed three strong peaks at 151.6, 233.4, and 1198.2 keV for ^{158}Nd, and two strong peaks at 150.2 and 893.0 keV for ^{160}Nd. Fig. 3(b) and (c) shows time spectra for ^{158}Nd and ^{160}Nd. The half-lives of γ rays were deduced as 0.339(20) μs and 1.63(21) μs, respectively.

From the systematics of Nd isotopes, the energy of the first 2^+ states is expected to be around 70 keV. However, such low-energy γ transition is mostly converted, and accordingly, the 70-keV peaks could not be observed clearly.

According to ref. [5], 67.2-, 155.0- and 238.6-keV γ rays of ^{156}Nd are understood as intraband transitions of ground state rotational band and the 970.6- and 1209.0-keV are transitions from the K isomeric state to 6_1^+ and 4_1^+ states. Assuming similar level structures in neighboring isotopes, $\sim$70-, 151.6- and 233.4-keV γ-rays of ^{158}Nd and $\sim$70-, 150.2-keV of ^{160}Nd are assigned as intraband transitions of ground state rotational bands. The other γ rays at 1198.2-keV in ^{158}Nd and 893.0 keV in ^{160}Nd are considered as transitions decaying from the isomer to the ground state band. Transition energies from 4_1^+ to 2_1^+ are increasing as neutron number increases. This may indicate that collectiv-
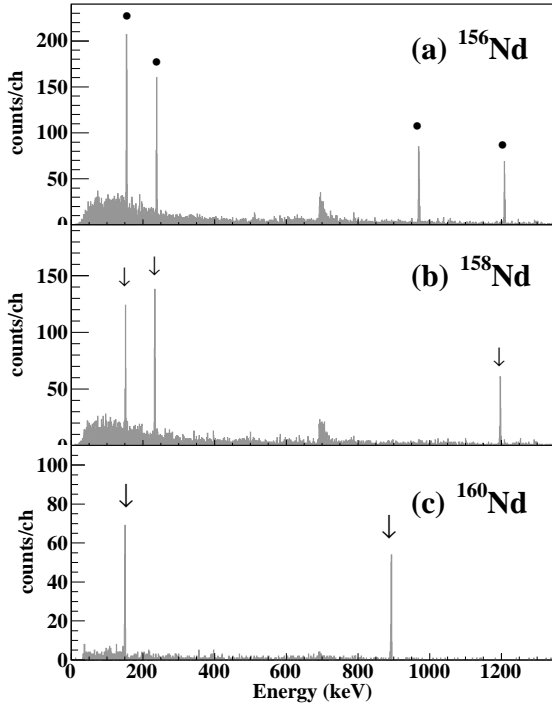
Figure 2: Gamma-ray energy spectra for (a)$^{156}_{60}$Nd$_{98}$, (b)$^{158}_{60}$Nd$_{98}$ and (c)$^{160}_{60}$Nd$_{100}$. Marked peaks are the γ rays of ^{156}Nd that previously known [5], and arrowed peaks are the γ rays identified newly. The spread peak at ~ 700 keV comes from (n, n$'$) reaction with Ge.
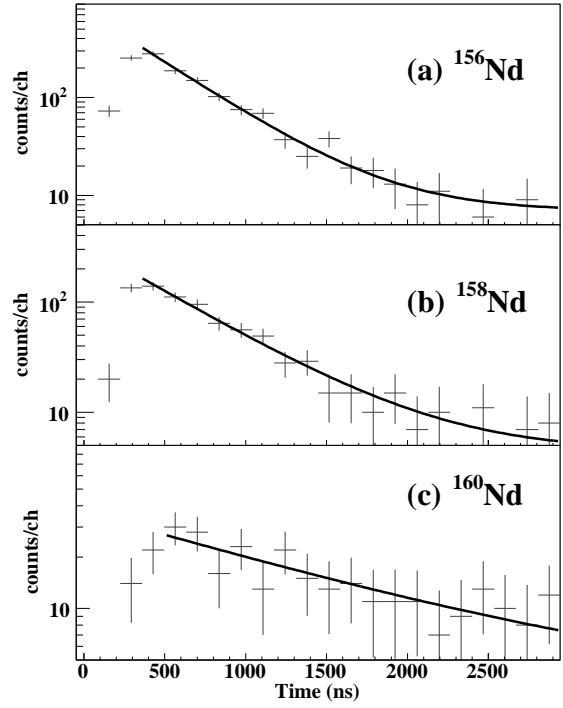
Figure 3: Gamma-ray time spectra for (a)^{156}Nd(gated on 155, 238, 970 and 1209 keV), (b)^{158}Nd(152, 233 and 1197 keV) and (c)^{160}Nd(895 keV).

[6] K. E. G. Löbner, Phys. Lett. B **26** (1968) 369.

ity is increasing in neutron-rich Nd isotopes.

For a further understanding of new isomers, the hindrance factor F_w was calculated. Here, F_w is defined as

$$F_w = \frac{T_{1/2(\text{exp})}}{T_{1/2(\text{Weisskopf})}}$$

where $T_{1/2(\text{exp})}$ and $T_{1/2(\text{Weisskopf})}$ denote measured and Weisskopf estimated half-life. In ^{158}Nd and ^{160}Nd, the hindrance factors are deduced to be 2.4×10^9 and 3.8×10^9, respectively. Such strong hindrance may imply the onset of a transition with large-ΔK in the deformed nucleus. From the systematic study of K isomers [6], it is known that such large hindrance emerges in $\Delta K = 4$, 5, 6 or 7 trainsitions. Based on the coincidence relations and the decay pattern, spin parity of new isomers are supposed to be 7^- for ^{158m}Nd and 4^- for ^{160m}Nd. The isomers in ^{156}Nd and ^{160}Nd can be understood as K isomers with $K^\pi = 7^-$ and $K^\pi = 4^-$, respectively.

To investigate non-yrast state of Nd isotopes and spin parity of neighboring odd-even and odd-odd nuclei β-γ analysis is now in progress.

References

[1] P. Möller et al., Atomic Data and Nuclear Data Tables **59** (1995)185.
[2] T. Kubo et al., Prog. Theor. Exp. Phys. 03C003 (2012).
[3] S. Nishimura et al., RIKEN Accel. Prog. Rep. **46** (2013) 182.
[4] S. Nishimura, Prog. Theor. Exp. Phys. 03C006 (2012).
[5] G. S. Simpson et al., Phys. Rev. C **80** (2009) 024304.

Quadrupole Collectivity in Island-of-Inversion Nuclei

S. Michimasa, Y. Yanagisawa[a], K. Inafuku,[b] N. Aoi[c], Z. Elekes[d], Zs. Fülöp[d], Y. Ichikawa[a], N. Iwasa[b], K. Kurita[e], M. Kurokawa[a], T. Machida[e], T. Motobayashi[a], T. Nakamura[f], T. Nakabayashi,[f] M. Notani[g], H. J. Ong[c], T. K. Onishi[h], H. Otsu[a], H. Sakurai[a,h], M. Shinohara[f], T. Sumikama[b], S. Takeuchi[a], K. Tanaka[a], Y. Togano[e], K. Yamada[a], M. Yamaguchi[a], and K. Yoneda[a]

Center for Nuclear Study, Graduate School of Science, University of Tokyo
[a]*RIKEN (The Institute of Physical and Chemical Research)*
[b]*Department of Physics, Tohoku University*
[c]*RCNP, Osaka University*
[d]*ATOMKI, Hungary*
[e]*Department of Physics, Rikkyo University*
[f]*Department of Physics, Tokyo Institute of Technology*
[g]*Argonne National Laboratory, USA*
[h]*Department of Physics, University of Tokyo*

We report here on the in-beam γ-ray spectroscopy in very neutron-rich even-even nuclei of ^{28,30}Ne and ^{34,36}Mg using a liquid hydrogen target with inverse kinematics. The ^{30}Ne has a conventional magic number of 20, and ^{36}Mg nucleus is located in the middle of the shell closures of $N = 20$ and 28. They are closer to the neutron drip line than nuclei belonging to the so-called "island of inversion (IOI)" [1]. We have studied evolution of quadrupole deformation in the side with more neutrons and less protons than IOI. The report is a condensed matter of our published paper [2].

The experiment was performed using the RIPS beamline at the RI Beam Factory. The radioactive secondary beam, containing neutron-rich nuclei ^{32,34,36}Mg and ^{28,30}Ne, was produced by fragmentation reactions from 63-MeV/nucleon ^{48}Ca. Details about the experimental setup around the secondary target and beam conditions are provided in Ref. [2]. The average energies of secondary beam particles were approximately 50 MeV/nucleon at the center of the reaction target. Total intensities of ^{30}Ne and ^{36}Mg were 1.5 and 0.3 particles per second, respectively, in the present experiment. The secondary target was a 95-mg/cm^2 thick liquid hydrogen that was produced and maintained by the CRYPTA system [3]. The γ rays were detected by the DALI2 array [4].

The angle-integrated cross sections for population of the 2_1^+ states were calculated from the yields of the $2_1^+ \rightarrow 0_1^+$ transition with γ-detection multiplicity (M_γ) equal to one. The cross sections for population of the excited states were observed by a decomposition analysis using simulated response functions of the de-excitation γ rays [5,6]. The spectra are referred to Figs. 3–6, 8 in Ref. [2], since there is no space in this report. The deduced cross sections are summarized in Table 1. The deduced deformation lengths and parameters are also summarized in Table 1.

The present results extend the measurements of quadrupole collectivity along Ne and Mg isotopic chains by providing improved deformation lengths in ^{28,30}Ne, ^{34}Mg and a new measurement for ^{36}Mg. The systematic trends of the deformation lengths are displayed in Fig. 1(a) and (b). In the panels, the filled and open circles indicate the deformation lengths deduced in the present work and those that have been estimated using the WP09 potential from the previous results [6–8], respectively. The thin black and thick orange error bars on the circles represent statis-

tical and systematic errors, respectively. The squares in the panels indicate results determined from Coulomb excitation [9–15]. The deformation lengths of ^{28}Ne and ^{32,34}Mg deduced from the both reactions are identical within experimental uncertainties. It indicates that neutron collectivities of these systems are similar to their proton collectivities. Accordingly, the closed-shell structure of neutron orbitals is not significant in these systems.

Figures 1(a) and (b) also display several theoretical studies that can be compared to the experimental results; The solid blue, dashed red lines are predictions by AMPGCM [16] and the shell model with the SDPF-M effective interaction [17], respectively. The shell model calculations in a $0\hbar\omega$ model space are shown by the green dotted [18] and orange dotted [19] lines. For Mg isotopes, the AMPGCM and SDPF-M calculations, which implement configuration mixing around $N = 20$, reproduce the systematic trend of experimental deformation lengths obtained in a satisfactory manner. Also, they agree with the trend of the Ne isotopic chain, although they both systematically overestimate the experimental results.

In order to clarify a difference of deformation evolutions in Ne and Mg chains, we consider here the ratio of deformation lengths of Ne and Mg isotones, $\delta(\mathrm{Ne})/\delta(\mathrm{Mg})$. Figure 1(c) provides the ratios as a function of neutron number. The lines in the figure show theoretical predictions in the same manner of the panels (a) and (b). The experimental tendency is flat and does not depend on whether the isotones lie inside or outside of IOI, although the theoretical calculations predict that an increase of the ratio occurs in IOI. This suggests that the structures of Ne and Mg isotones develop in a similar manner as the function of neutron number.

In order to verify the development of $2\hbar\omega$ configuration in Mg isotopes more thoroughly, Fig. 1(d) provides the ratio of deformation lengths of Mg and Si isotopes with the same neutron number, $\delta(\mathrm{Mg})/\delta(\mathrm{Si})$. The experimental deformation lengths of the Si isotopes were adopted from Refs. [9, 20]. The experimental ratio gradually increases with neutron number, starting from isotopes at stability, and then begins to decrease beyond $N = 20$. It should be realized that the low-lying states in Si isotopes discussed here are described well by $0\hbar\omega$ configurations and therefore the enhancement of $\delta_\mathrm{C}(\mathrm{Mg})/\delta_\mathrm{C}(\mathrm{Si})$ highlights the devel-

Table 1: Angle-integrated cross sections for the 2_1^+ states in ^{28,30}Ne and ^{32,34,36}Mg, and deformation lengths deduced from these cross sections.

Nucleus	$\sigma(2_1^+)$ (mb)	$\delta_{(p,p')}$ (fm)	$\beta_{(p,p')}$
^{28}Ne	23(2)	1.33 ± 0.06 (stat) ± 0.05 (syst)	0.39 ± 0.02 (stat) ± 0.01 (syst)
^{30}Ne	37(4)	$1.59^{+0.08}_{-0.09}$ (stat) ± 0.07 (syst)	$0.45^{+0.02}_{-0.03}$ (stat) ± 0.02 (syst)
^{32}Mg	40^{+9}_{-8}	1.85 ± 0.20 (stat) ± 0.08 (syst)	$0.51^{+0.06}_{-0.05}$ (stat) ± 0.02 (syst)
^{34}Mg	63(5)	$2.30^{+0.09}_{-0.10}$ (stat) ± 0.16 (syst)	0.62 ± 0.03 (stat) ± 0.05 (syst)
^{36}Mg	47(8)	$1.90^{+0.16}_{-0.17}$ (stat) ± 0.16 (syst)	$0.50^{+0.04}_{-0.05}$ (stat) ± 0.04 (syst)

opment of intruder configurations in Mg isotopes relative to their Si isotonic counterparts. The SDPF-M shell model predicts an increase in the intruder configuration mixing from ^{30}Mg to ^{32}Mg, and then a decrease from ^{32}Mg to ^{36}Mg. The overall trend of SDPF-M expresses well the evolution of the intruder configuration mixing along the Mg isotopic chain.

Concerning configuration mixing in ^{36}Mg, the decrease in the experimental ratio of the deformation lengths can be considered to be ascribed to the reduction in the dominance of intruder configurations from ^{34}Mg to ^{36}Mg, since SDPF-M also reproduces the the 2_1^+ energies of ^{34}Mg and ^{36}Mg in a satisfactory manner. The SDPF-M shell model predicts that intruder (normal) configurations are present at 60% (40%) in the ground state, and the previous study [21] stated that ^{36}Mg contains a $0\hbar\omega$ component at a level of approximately 40%. The present result for ^{36}Mg is also consistent with the SDPF-M shell model. Furthermore, the result may indicate that ^{36}Mg is located in a competitive region between normal and intruder configuration, since the ratio deduced in the present work is located between the predictions of SDPF-M and the $0\hbar\omega$ shell model.

[6] S. Takeuchi *et al.*, Phys. Rev. C **79** (2009) 054319.
[7] Zs. Dombrádi *et al.*, Phys. Rev. Lett. **96** (2006) 182501.
[8] Y. Yanagisawa *et al.*, Phys. Lett. B **566** (2003) 84.
[9] S. Raman *et al.*, Atomic Data Nucl. Data Tables **78** (2001) 1.
[10] O. Niedermaier *et al.*, Phys. Rev. Lett. **94** (2005) 172501.
[11] T. Motobayashi *et al.*, Phys. Lett. B **346** (1995) 9.
[12] H. Iwasaki *et al.*, Phys. Lett. B **522** (2001) 227.
[13] J.A. Church *et al.*, Phys. Rev. C **72** (2005) 054320.
[14] J. Gibelin *et al.*, Phys. Rev. C **75** (2007) 057306.
[15] H. Iwasaki *et al.*, Phys. Lett. B **620** (2003) 118.
[16] R.R. Rodríguez-Guzmán *et al.*, Eur. Phys. J. A **17** (2003) 37; Nucl. Phys. A **709** (2002) 201; Phys. Lett. B **474** (2000) 15.
[17] Y. Utsuno *et al.*, Rhys. Rev. C **60** (1999) 054315.
[18] E. Caurier *et al.*, Rhys. Rev. C **58** (1998) 2033.
[19] F. Nowacki and A. Poves, Phys. Rev. C **79** (2009) 014310.
[20] R.W. Ibbotson *et al.*, Phys. Rev. Lett. **80** (1998) 2081.
[21] A. Gade *et al.*, Phys. Rev. Lett. **99** (2007) 072502.
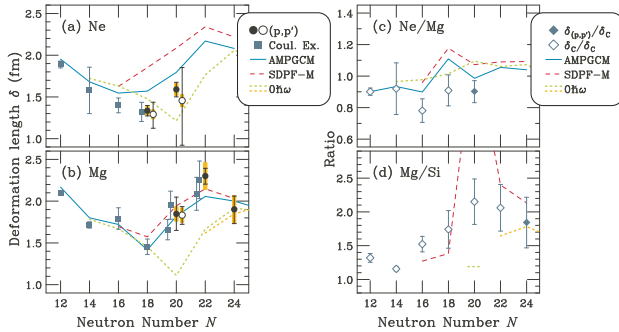
Figure 1: Systematics of deformation lengths around the island-of-inversion region. Panels (a) and (b) show deformation lengths of Ne and Mg isotopes, respectively. Panels (c) and (d) show ratios of deformation lengths of isotones around the island of inversion. Panel (c) [(d)] is the ratios of Mg and Ne [Si and Mg] isotones. Details are described in the text.

References

[1] E.K. Warburton *et al.*, Phys. Rev. C **41** (1990) 1147.
[2] S. Michimasa *et al.*, Phys. Rev. C **89** (2014) 054307.
[3] H. Ryuto *et al.*, Nucl. Instrum. Methods Phys. Res. Sect. A **555** (2005) 1.
[4] S. Takeuchi *et al.*, Nucl. Instrum. Methods Phys. Res. Sect. A **763** (2014) 596.
[5] S. Michimasa *et al.*, Phys. Lett. B **638** (2006) 146.

A new nuclear 'magic' number from the structure of ^{54}Ca

D. Steppenbeck, S. Takeuchi[a], N. Aoi[b], P. Doornenbal[a], M. Matsushita, H. Wang[a], H. Baba[a],
N. Fukuda[a], S. Go, M. Honma[c], J. Lee[a], K. Matsui[d], S. Michimasa, T. Motobayashi[a],
D. Nishimura[e], T. Otsuka, H. Sakurai[a,d], Y. Shiga[f], N. Shimizu, P.-A. Söderström[a], T. Sumikama[g],
H. Suzuki[a], R. Taniuchi[d], Y. Utsuno[h], J. J. Valiente-Dobón[i], and K. Yoneda[a]

Center for Nuclear Study, Graduate School of Science, University of Tokyo
[a]*RIKEN Nishina Center for Accelerator-Based Science*
[b]*Research Center for Nuclear Physics, University of Osaka*
[c]*Center for Mathematical Sciences, Aizu University*
[d]*Department of Physics, University of Tokyo*
[e]*Department of Physics, Tokyo University of Science*
[f]*Department of Physics, Rikkyo University*
[g]*Department of Physics, Tohoku University*
[h]*Japan Atomic Energy Agency*
[i]*Istituto Nazionale di Fisica Nucleare, Laboratori Nazionali di Legnaro*

Experimental studies of nuclei that lie far from stability on the chart of nuclides have become possible over recent years owing to the advent of very intense radioactive beams. Investigations into the evolution of nuclear shell structure in systems with large neutron-to-proton ratios has been one of the focal points in the fields of both experimental and theoretical nuclear physics. For example, the onset of a new magic number at $N = 16$ has been reported in exotic oxygen [1, 2], while the disappearance of the standard neutron magic number $N = 28$ has been investigated in ^{42}Si [3, 4]. In the neutron-rich fp shell, the onset of a new subshell closure at $N = 32$ in the radioactive isotones ^{52}Ca [5, 6], ^{54}Ti [7, 8], and ^{56}Cr [9, 10] has been documented by measuring excited state energies and reduced transition probabilities. More recently, the $N = 32$ subshell gap was confirmed by high-precision mass measurements of exotic calcium isotopes [11]. Moreover, a large subshell closure at $N = 34$ in calcium isotopes was predicted over a decade ago [12]; however, investigations of ^{54}Ca on the experimental front were hindered in the past owing to the insufficient intensities of appropriate radioactive beams. It is noted that experimental investigations into the structures of ^{56}Ti [8, 13] and ^{58}Cr [9, 10], which lie closer to stability relative to ^{54}Ca, indicate that no significant $N = 34$ subshell closure is present in those nuclei.

In the framework of tensor-force-driven nuclear shell evolution [14], development of the $N = 32$ and 34 subshell closures occurs because the strength of the attractive monopole interaction between protons in the $\pi f_{7/2}$ single-particle orbital (SPO) and neutrons in the $\nu f_{5/2}$ SPO decreases as the proton number is reduced from $Z = 28$ to 20. Thus, the $\nu f_{5/2}$ SPO shifts up in energy relative to the $\nu p_{3/2}$–$\nu p_{1/2}$ spin-orbit partners, consequently forming new subshell closures above $N = 32$ and 34. In order to confirm the presence of the predicted $N = 34$ subshell closure in calcium, excited states in ^{54}Ca were investigated in the present work for the first time.

The experiment was performed at the RIKEN Radioactive Isotope Beam Factory using in-beam γ-ray spectroscopy with ^{9}Be(^{55}Sc,^{54}Ca$+\gamma^n$)X and ^{9}Be(^{56}Ti,^{54}Ca$+\gamma^n$)X (where $n \geq 1$) proton knockout reactions. The total number of events recorded to disk for the respective reactions were $\sim 1.4 \times 10^4$ and 9.1×10^3.

The structure of ^{53}Ca was also investigated; in this case the ^{9}Be(^{55}Sc,^{53}Ca$+\gamma^n$)X and ^{9}Be(^{56}Ti,^{53}Ca$+\gamma^n$)X multi-nucleon removal reactions were adopted. The secondary beam, which contained ^{55}Sc and ^{56}Ti amongst other constituents, was produced using the particle fragmentation technique with a primary beam of ^{70}Zn^{30+} ions at 345 MeV/u and a maximum intensity of ~ 100 pnA. Particle identification of the secondary beam was performed by measuring ion magnetic rigidities ($B\rho$), times of flight (T), and energy losses (ΔE) with the BigRIPS separator [15]; the particle identification plot is displayed in Fig. 1. The rates of ^{55}Sc and ^{56}Ti transmitted through BigRIPS were ~ 12 and 125 ions per second per pnA of primary beam, respectively. The radioactive beam was focused on a 10-mm-thick ^{9}Be reaction target at the eighth focal plane of the BigRIPS separator to induce nucleon removal reactions; the reaction products, which are presented in Fig. 1, were identified with the ZeroDegree spectrometer [15] using the same general ($B\rho$–T–ΔE) techniques as discussed for BigRIPS. The reaction target was surrounded by DALI2 [16], an array of 186 high-efficiency NaI(Tl) γ-ray detectors positioned at angles of $\sim 20°$–$150°$ relative to beam line, to measure γ rays emitted from nuclear excited states.

The γ-ray energy spectrum, measured in coincidence with ^{54}Ca ions in the ZeroDegree spectrometer and either ^{55}Sc or ^{56}Ti ions in the BigRIPS separator, is displayed in Fig. 2(a) for events with a total γ-ray multiplicity (M_γ) of
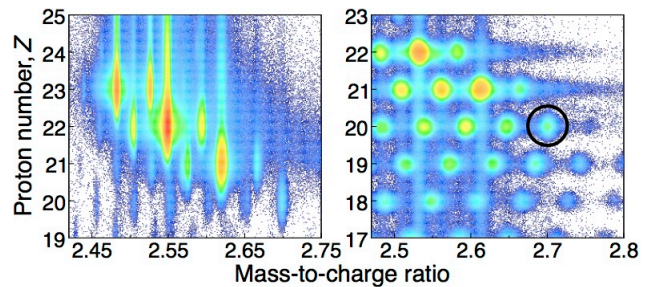
Figure 1: Particle identification plots for ions measured using the BigRIPS separator (left) and ZeroDegree spectrometer (right). Events enclosed by the circle (right panel) are ^{54}Ca.

$M_\gamma = 1$. All γ-ray peaks are reported in the present study for the first time. The most intense γ-ray line in the spectrum, the peak at 2043(19) keV, is assigned as the transition from the first 2^+ state (2_1^+) to the 0^+ ground state. Thus, the energy of the 2_1^+ state in ^{54}Ca is comparable to the value in ^{52}Ca (2.56 MeV) [5, 6] and is, therefore, suggestive of a sizable subshell closure at $N = 34$ in calcium. In order to investigate the nature of the $N = 34$ gap in more detail, shell-model calculations using a modified GXPF1B Hamiltonian [17] were performed in the full fp model space without restrictions. Indeed, the calculations indicate that the $N = 34$ subshell gap (the $\nu p_{1/2}$–$\nu f_{5/2}$ SPO energy gap) in ^{54}Ca is similar in magnitude to the $N = 32$ gap (the $\nu p_{3/2}$–$\nu p_{1/2}$ SPO energy gap) in ^{52}Ca, thus, providing direct evidence for a new nuclear magic number in calcium for the first time. Other transitions were measured at 1656(20) and 1184(24) keV and are assigned to ^{54}Ca. The 1656(20)-keV γ ray is proposed to depopulate the first 3^- state at 3699(28) keV based on $\gamma\gamma$ coincidences, which are presented in Fig. 2(b), γ-ray relative intensities, systematics observed in lighter Ca isotopes, and predictions of shell-model calculations performed in the $sdfp$ model space. Placement of the 1184(24)-keV transition in the level scheme is rather ambiguous; however, it is suggested to run in parallel to the 1656(20)-keV line based on the observation of a transition at ~ 472 keV in the $\gamma\gamma$ coincidence spectrum of Fig. 2(b).

The structure of ^{53}Ca, which may also reflect the magnitude of the $N = 34$ subshell closure, was also investigated in the present work. The Doppler-corrected γ-ray energy spectrum ($M_\gamma = 1$), measured in coincidence with ^{53}Ca ions in the ZeroDegree spectrometer and either ^{55}Sc or ^{56}Ti ions in the BigRIPS separator, is presented in Fig. 2(c); two transitions at 1753(15) and 2227(19) keV were identified. The line at 2227(19) keV is consistent in energy with a peak previously assigned to ^{53}Ca in a decay study [18], while the 1753(15)-keV peak is reported in the present work for the first time. The $\gamma\gamma$ coincidences displayed in Fig. 2(d) indicate that the two γ rays are not in coincidence and, therefore, the transitions are placed in parallel in the ^{53}Ca level scheme where two excited states at 1753(15) and 2227(19) keV both decay directly to the ground state. The spins and parities of the two excited states are tentatively assigned $5/2^-$ and $3/2^-$, respectively, based on the result of Ref. [18] and predictions of the modified GXPF1B effective interaction and other nuclear theories, for example, Refs. [19–21]. The excited states at 1753(15) and 2227(19) keV are primarily understood as single neutron excitations across the $N = 34$ ($\nu p_{1/2} \to \nu f_{5/2}$) and 32 ($\nu p_{3/2} \to \nu p_{1/2}$) subshell closures, respectively. Further details on ^{53}Ca and ^{54}Ca are provided in Ref. [22].

Figure 2: Doppler-corrected γ-ray energy spectra for (a) ^{54}Ca and (c) ^{53}Ca. Insets (b) and (d) indicate $\gamma\gamma$ coincidences with energy gates (hatched regions) placed on the 2043- and 1753-keV γ rays, respectively.

[11] F. Wienholtz *et al.* Nature (London) **498** (2013) 346.
[12] T. Otsuka *et al.* Phys. Rev. Lett. **87** (2001) 082502.
[13] S. N. Liddick *et al.* Phys. Rev. Lett. **92** (2004) 072502.
[14] T. Otsuka *et al.* Phys. Rev. Lett. **95** (2005) 232502.
[15] T. Kubo *et al.* Prog. Theor. Exp. Phys. (2012) 03C003.
[16] S. Takeuchi *et al.* Nucl. Instrum. Meth. Phys. Res. A **763** (2014) 596.
[17] M. Honma, T. Otsuka, and T. Mizusaki. RIKEN Accel. Prog. Rep. **41** (2008) 32.
[18] F. Perrot *et al.* Phys. Rev. C **74** (2006) 014313.
[19] M. Rejmund *et al.* Phys. Rev. C **76** (2007) 021304(R).
[20] L. Coraggio *et al.* Phys. Rev. C **80** (2009) 044311.
[21] G. Hagen *et al.* Phys. Rev. Lett. **109** (2012) 032502.
[22] D. Steppenbeck *et al.* Nature (London) **502** (2013) 207.

References

[1] R. Kanungo *et al.* Phys. Rev. Lett. **102** (2009) 152501.
[2] C. R. Hoffman *et al.* Phys. Lett. B **672** (2009) 17.
[3] B. Bastin *et al.* Phys. Rev. Lett. **99** (2007) 022503.
[4] S. Takeuchi *et al.* Phys. Rev. Lett. **109** (2012) 182501.
[5] A. Huck *et al.* Phys. Rev. C **31** (1985) 2226.
[6] A. Gade *et al.* Phys. Rev. C **74** (2006) 021302(R).
[7] R. V. F. Janssens *et al.* Phys. Lett. B **546** (2002) 55.
[8] D.-C. Dinca *et al.* Phys. Rev. C **71** (2005) 041302(R).
[9] J. I. Prisciandaro *et al.* Phys. Lett. B **510** (2001) 17.
[10] A. Bürger *et al.* Phys. Lett. B **622** (2005) 29.

Experiment Nuclear Physics: PHENIX Experiment at BNL-RHIC and ALICE Experiment at CERN-LHC

GEM-TPC Upgrade for the ALICE Experiment

T. Gunji, H. Hamagaki, Y. L. Yamaguchi, K. Terasaki, K. Yukawa,
for the ALICE Collaboration

Center for Nuclear Study, Graduate School of Science, The University of Tokyo

1. ALICE Upgrade after LS2

The ALICE experiment is dedicated to the studies of the properties of the strongly interacting QCD medium (Quark-Gluon Plasma, QGP) by conducting ultra-relativistic heavy-ion collisions at the LHC [1]. A significant increase of the luminosity for heavy ions is expected in RUN 3 after Long Shutdown 2 (LS2), which implies a collision rate of about 50 kHz and $\mathcal{L}_{\mathrm{int}}$ = 10 nb^{-1}. This luminosity upgrade provides a substantial enhancement of capabilities for measuring the sensitive observables for the characterization of the QGP at the highest temperatures [2]. In order to exploit the scientific potential of the high-luminosity heavy-ion program in RUN 3, ALICE plans to extend its physics reach by upgrading the ALICE detector.

2. ALICE TPC Upgrade

The Time Projection Chamber (TPC) is one of the main devices in the central barrel of the ALICE detector. It provides precise charged-particle tracking, momentum measurement, and particle identification in very high-multiplicity heavy-ion collisions [3]. The readout rate of the TPC is currently limited by the necessity to prevent ions generated in the amplification region of the MWPC-based readout chambers from drifting back into the drift volume, which is achieved through active ion gating by operating a dedicated gating grid. The relevant ion drift times limit the maximum trigger rate of the TPC to about 3.5 kHz.

Operation of the current TPC with the MPWC-based readout scheme and the current active ion gating scheme at 50 kHz Pb-Pb collisions in RUN 3 cannot be possible. On the other hand, operation of the current TPC with continuously open gating grid cannot be the solution since back-drifting ions from the amplification region will lead to excessive ion charge densities and distortions of the electric field in the drift volume. The proposed scheme to acquire high rate operational capability and a small number of the back-drifting ions is to replace the existing MWPC-based readout chambers and gating grid system by a multi-layer Gas Electron Multiplier (GEM) system and to run the TPC in an ungated continuous mode. GEMs have been developed to cope with the stringent requirements for high-luminosity experiments [4] and have proven to provide excellent position resolution, to have very high rate capability, and to have better ion blocking capability compared to MWPC. The main considerations for the TPC upgrade and the design requirements are as follows [5]:

- The maximum ion backflow (IBF) that can be tolerated is about 1% at a gain of 2000 in Ne-CO$_2$-N$_2$ (90-10-5), i.e 20 back-drifting ions per incoming primary electron.

- In case of IBF=1%, space charge field distortions reach 20 cm and 8 cm in r and $r\phi$ at small r and z ($|\eta| \sim 0$) in the TPC, respectively. In order to preserve the present momentum resolution, online and offline distortion corrections with a precision better than 500 μm, i.e. a few times 10^{-3}, are required.

- Due to the limited bandwidth of the data acquisition system, reduction of data flow size by a factor of 20 is needed in the online reconstruction by finding the clusters associated to tracks.

- The upgraded TPC must preserve the performance of the existing system in terms of particle identification via dE/dx, implying a local energy resolution better than 12% for ^{55}Fe (5.9 keV).

3. Status of R&D Activities

An extensive R&D program has been started in 2012 to study the performance of GEM-based detectors (IBF, gain stability, discharge probability), technology choice (GEM stacks including the combination of GEMs with different pitches, COBRA-GEM, 2 GEM + Micromegas system), large prototype production by single mask technology, electronics R&D, and simulation studies to establish the strategy for space charge distortion corrections.

Our baseline solution comprises stacks of 4 GEM layers, where 1st and 4th GEMs are standard GEMs with 140 μm pitch, 50 μm thickness, and 70 (50) μm outer (inner) hole diameter, and 2nd and 3rd GEMs are large pitch GEM foils with 280 μm pitch, 50 μm thickness, and 70 (50) μm outer (inner) hole diameter. This setup allows to block ions efficiently by employing low/high fields above/below GEMs and foils with low optical transparency. Figure 1 shows the results of the measured IBF and energy resolution at 5.9 keV at a gain of 2000 for a 4-GEM system, where the voltage across GEM1 increases from left to right along the x-axis. It can be seen that an IBF of 0.7% is achieved at an energy resolution of 12% (at 5.9 keV). The observed anti-correlation between ion backflow and resolution is related to the gains of the first two GEMs: higher electron multiplication at the early stages improves energy resolution but also increase the number of ions escaping into the drift volume.

Detailed simulations based on Garfield++ [6] were performed to describe the observed IBF performance. It was found that IBF is very sensitive to the alignment of the GEM holes in consecutive layers, which can not be controlled experimentally. The measured IBF values are best reproduced in simulations, if a random misalignment of the holes is assumed, corresponding to the most probable relative geometrical position of GEM foils in a stack.

An alternative solution is a system combining 2 GEMs with a Micromegas detector. Micromegas (MM) provides low IBF due to the larger ratio of the electric field values in the small amplification gap to the drift field above the MM. If the MM employs a fine mesh (400-1000 LPI), IBF is close to the ratio between two fields itself [7]. The IBF and energy resolution for this hybrid 2-GEM + MM system were measured using 10×10 cm^2 prototype detector. The results are shown in Fig. 2, where an IBF of 0.2% is reached at an energy resolution of 12% (at 5.9 keV). A large-scale
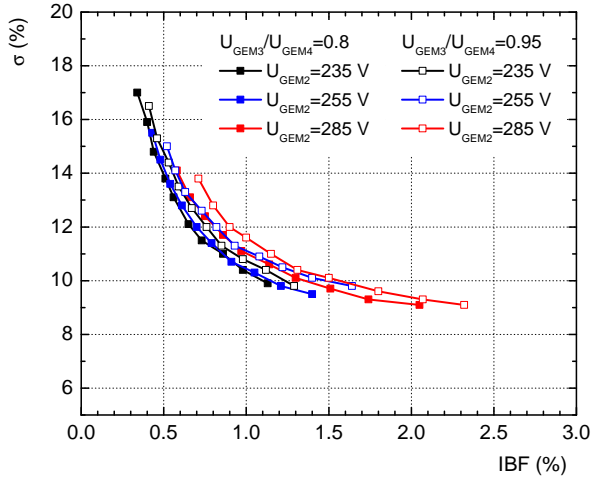
Figure 1: Correlation between ion backflow and energy resolution at 5.9 keV in a 4 GEM setup (S-LP-LP-S) in Ne-CO_2-N_2 (90-10-5) for various settings of voltage of GEM2.

GEM pitches provide the required IBF and energy resolution. Also a design based on a hybrid configuration of GEMs and Micromegas is studied. Large size of the prototypes (IROC) for 4 GEM stacks and 2 GEM + MM system are being built and beam test will be carried out at the PS and the SPS in 2014.

References

[1] ALICE Collaboration, "The ALICE experiment at the CERN LHC", JINST 3.08 (2008), S08002.

[2] ALICE Collaboration, "Upgrade of the ALICE Experiment: Letter Of Intent", CERN-LHCC-2012- 012 / LHCC-I-022. 2012.

[3] ALICE Collaboration. Technical Design Report of "the Time Projection Chamber". CERN/LHCC 2000-001. 2000

[4] F. Sauli. Nucl. Instr. Meth. A 386.2-3 (1997), pp. 531-534

[5] ALICE Collaboration, Technical Design Report of "Upgrade of the ALICE Time Projection Chamber", CERN-LHC C-2013-020 (2013)

[6] R. Veenhof. URL: http://garfield. web.cern.ch.

[7] P. Colas, I. Giomataris, and V. Lepeltier, Nucl. Instr. Meth. A 535.1-2 (2004), pp. 226-230.

solution for the inner and outer TPC readout chambers and the operational stability will be verified in the future.
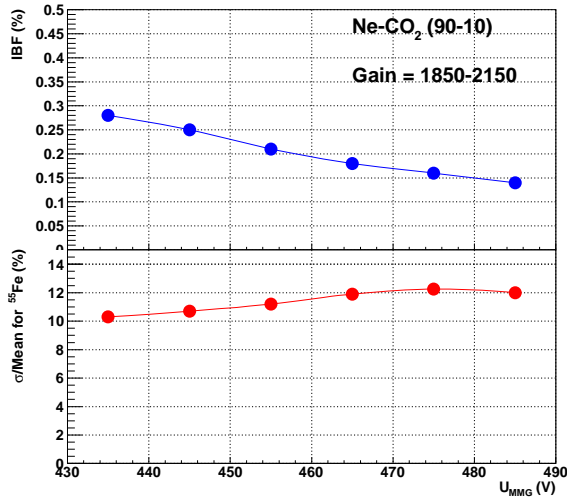
Figure 2: Upper: IBF as a function of voltage at mesh for 2-GEM + MM system. Bottom: Energy resolution as a function of voltage at mesh for 2-GEM + MM system

4. Summary and Outlook

To exploit the full potential of the high luminosity of the LHC in RUN 3, the ALICE program for RUN 3 requires an upgrade of the TPC. The current idea to fulfill the requirements is to replace the MWPC-based readout chambers by detectors employing micro-pattern detectors including GEMs to allow TPC operation in continuous mode. Extensive detector R&D and simulations have been conducted and a baseline scenario for the detector design has been established. Quadruple stacks of GEM layers with different

Measurements of π^0 v_2 in Pb-Pb collisions at $\sqrt{s_{NN}}$=2.76 TeV at LHC-ALICE

T. Tsuji, H. Hamagaki, T. Gunji, for the ALICE collaboration

Center for Nuclear Study, Graduate School of Science, University of Tokyo

1. Introduction

It has been observed that the yield of charged particles at a high transverse momentum (p_T) is strongly suppressed in central Pb+Pb collisions at ($\sqrt{s_{NV}}$) = 2.76 TeV at the Large Hadron Collider (LHC) facility at CERN compared to the expected yield from the scaling with the number of nucleon-nucleon binary collisions. This suppression is attributed to the energy loss of hard scattered partons within quark-gluon plasma (QGP) created in heavy ion collisions. This suppression is called jet quenching. This suppression can be quantified by to the nuclear modification factor (R_{AA}) where the ratio between the measured yield and the expected yield from the $p + p$ result is scaled by the thickness function $\langle T_{AA} \rangle$ of the two nuclei

$$R_{AA}(p_T) = \frac{1}{<T_{AA}>} \frac{(1/N_{AA}^{evt})d^2 N_{AA}/dp_T dy}{d^2 \sigma_{pp}/dp_T dy}. \quad (1)$$

R_{AA} can be equally well described by several theoretical models with different approaches that calculate the energy loss by the hard scattering partons as they traverse the dense medium. To discriminate among these models we need to increase our experimental control of the path length L, since these theoretical models can be discriminated using their different path length dependence. A quadratic dependence on the path length is predicted for a static medium if the dominant energy-loss mechanism is the bremsstrahlung radiation of gluons surviving the destructive interference caused by multiple scattering [1]. For an expanding plasma the quadratic increase should be moderated to a linear dependence [2]. Thus, the measurement of the energy loss with respect to the path length is expected to enable us to obtain the detail information about the mechanism of the parton energy loss.

The single particle observable R_{AA} typically has smaller statistical errors and higher p_T reach. In semi-central ion-ion collisions, the overlap region of the nuclei is not azimuthally isotropic. The average path length of partons in QGP varies as a function of the angle with respect to the event plane. Therefore, differential observable $R_{AA}(\Delta\phi)$ directly probes the path length dependence of the energy loss.

The $R_{AA}(p_T, cent, \Delta\phi)$ with respect to the azimuthal angle is factorized as,

$$R_{AA}(p_T, cent, \Delta\phi) = F(\Delta\phi, p_T) \cdot R_{AA}(p_T, cent), \quad (2)$$

where $F(\Delta\phi, p_T)$ is ratio of the relative yield given as,

$$F(\Delta\phi, p_T) = \frac{N(\Delta\phi, p_T)}{\int d\phi N(\Delta\phi, p_T)}, \quad (3)$$

where $N(\Delta\phi, p_T)$ can be expressed in terms of a Fourier expansion with $\Delta\phi$.

$$N(\Delta\phi, p_T) \propto 1 + 2\sum_{n=1}^{\inf} (v_n \cos(n\Delta\phi)), \quad (4)$$

where v_n is the magnitude of the harmonics of n-th order. The second harmonics, v_2, represents the strength of elliptic azimuthal anisotropy. The anisotropy v_2 at low p_T is created by the collective flow, which is an origin of the background in measuring the $R_{AA}(p_T, \Delta\phi)$ for investigating the energy loss. Therefore, energy loss mechanism is studied with π^0 for a wide momentum range.

2. Basic performance of detectors

The π^0 yield is extracted using the photon spectrometer (PHOS) of the ALICE experiment. The present PHOS detector consists of three modules installed at a distance of 4.60 m from the interaction point. PHOS covers the acceptance of 260 ° $< \phi <$ 320 ° and $|\eta| < 0.12$ in pseudo rapidity. Each module has 3584 detection channels in a matrix of 64 × 56 cells. Each detection channel consists of a lead tungsten, PbWO$_4$, crystal of 2.2 × 2.2 cm × 18 cm^3, coupled to an avalanche photo diode with a low-noise charge-sensitive preamplifier. PHOS is operated at a temperature of -25 °C where the light yield of the PbWO$_4$ crystal is about 3 times larger than the yield at room temperature. PHOS was calibrated by equalizing mean deposited energies in each channel using events with pp collisions [4].

Event plane is measured in V0A and V0C detectors, which are scintillation detector and covering $2.8 < \eta < 5.1$ and $-3.7 < \eta < -1.7$, respectively. The V0A and V0C is fixed at the front face of the front absorber, 340 cm and 90 cm from the interaction point, respectively. Each detector is segmented into 4 rings in radial direction and each ring is divided into 8 sectors in azimuthal direction. The psudo-rapidity coverage of each ring ranges between 0.4 and 0.6. The elementary sector consists of scintillator material with embedded WaveLength Shifting (WLS) fibres. The light from the WLS is collected by clear fibers and transported to PhotoMultiplier (PM) installed at 3 - 5 m from the detectors, inside the L3 magnet [3].

3. Expectation of π^0 v_2 values

$\pi^0 v_2$ is extracted with relation between raw yield and the azimuthal angle from the event plane.
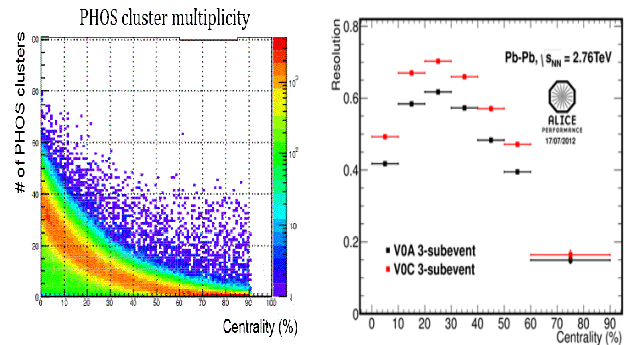
Figure 1: Left: Correlation between the number of PHOS clusters and centrality. Right: Trigger efficiency in p+p collisions as a function of p_T in each module. Higher values indicate better resolution.

Figure 1 (left) shows PHOS cluster multiplicity. Centrality is defined by V0 detectors. There is expected multiplicity correlation between V0 detectors and PHOS. Figure 1 (right) shows the event plane resolution of V0A and V0C. The event plane resolution with sub-event i can be calculated in the three sub-event method by as following:

$$R = \sqrt{\frac{\langle\cos[2(\Psi_i - \Psi_j)]\rangle\langle\cos[2(\Psi_i - \Psi_l)]\rangle}{\langle\cos[2(\Psi_j - \Psi_l)]\rangle}}, \quad (5)$$

where subscripts j and l represent other two sub-events. In this analysis, in order to calculate the V0A and V0C event plane resolutions, TPC standalone tracks at $-0.8 < \eta < 0.8$ are used. The resolution is centrality dependent and V0C has better resolutions, as shown in Fig. 1 (right).
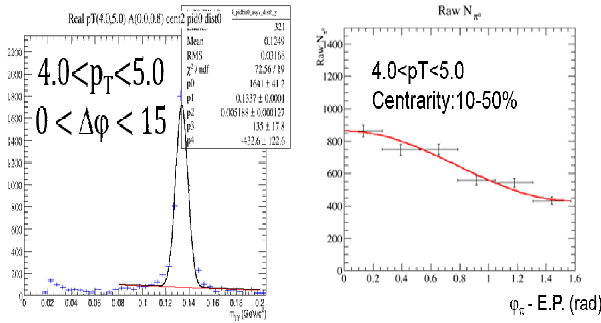
Figure 2: Left: Invariant mass distribution with $p_T = 4 - 5$ GeV/c and centrality = 10% - 50% with $\Delta\phi = 0° - 15°$. Right: The number of π^0 as a function of the azimuthal angle. Red line shows fitting function Eq. (1).

π^0 are identified using invariant mass with reconstructed energy by PHOS. Figure 2 (left) shows the invariant mass distribution with $p_T = 4 - 5$ GeV/c and centrality = 10% - 50% with $\Delta\phi = 0° - 15°$. The invariant mass distribution is fitted with Gauss function and linear function and the raw yield of π^0 is calculated to integrate the number of entries of the distribution within 3 σ. Figure 2 (right) shows the number of π^0 as a function of azimuthal angle for $p_T = 4 - 5$ GeV/c and centrality = 10% - 50%. It is confirmed that the number of π^0 depends on the azimuthal angle from the event plane. As shown Fig. 2 (right), v_2 is obtained by fitting the azimuthal angular distribution of π^0 with

$$N(\Delta\phi, p_T) = N(1 + 2v_2 \cos(2\Delta\phi)). \quad (6)$$

At first, π^0 was identified up to $p_T = 40$ GeV/c by PHOS with all data in 2011 run. Figure3 shows $\pi^0 v_2$ values as a function of p_T. In this figure, all data for semi-central triggered events in 2011 are analyzed. In this plot, $\pi^0 v_2$ values denote the same tendency of the v_2 values of the charged particles qualitatively [4]. The comparison of measured $\pi^0 v_2$ with several model predictions are presently ongoing.

4. Summary and Outlook

Jet quenching is sensitive to the density and path length of QGP. Study of dependencies of R_{AA} on path length and azimuthal angle has been started with the photon spectrometer (PHOS) at the ALICE experiment. Analysis with PHOS is advantaged that π^0 can be identified at widest p_T region. π^0 v_2 is extracted and calculations of $\pi^0 v_2$ are ongoing.
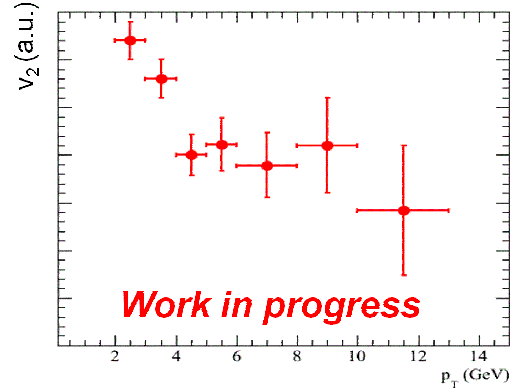
Figure 3: v_2 values as a function of p_T. Bars in each bins show statistical errors of fitting function Eq. (1).

References

[1] A. Majumber, J. Phys. G: Nucl. Part. Phys. **34** (2007) S377.

[2] M. Gyulassy, P. Levai and I. Vitev, Phys. Lett. **B538** (2002) 282.

[3] F Carminati *et al.* (ALICE Collaboration), J. Phys. G: Nucl. Part. Phys. **30** (2004) 1517.

[4] B. Abelev et al., for the ALICE Collaboration: Phys. Lett. **B719**, 18-28 (2013).

Study of dielectron production in p-Pb collisions at $\sqrt{s_{NN}} = 5.02$ TeV using ALICE-TRD triggered data

S. Hayashi, H. Hamagaki, and T. Gunji on behalf of ALICE Collaboration

Center for Nuclear Study, Graduate School of Science, University of Tokyo

1. Introduction

The principal aim of the heavy ion collisions at the Large Hadron Collider (LHC) is to investigate the properties of the deconfined matter, the quark-gluon plasma (QGP). Heavy quarks like charm and bottom quarks are produced in the hard scattering process at the initial stage of the collisions. The measurements of the transverse momentum spectrum, and the azimuthal angular correlation of $c\bar{c}$ and $b\bar{b}$ provide the key information on the interaction of heavy quarks in the medium.

Since heavy quarks are produced via gluon fusion, gluon splitting, and flavor excitation at the LHC energy, cold nuclear matter effects such as gluon shadowing, gluon saturation, and Cronin effect cannot be negligible [1]. p-A collisions are suitable to study cold nuclear matter effects. The measurement of electron-muon correlation at PHENIX in d+Au collisions, where the same Bjorken-x can be accessible in the midrapidity at the LHC ($x \sim 10^{-3}$), shows the large suppression of back-to-back correlation [2]. In p-Pb collisions at the LHC, transverse momentum spectra of open heavy flavors shows no modification from the heavy flavor production in pp collisions [3]. However, electron and charged hadron correlation from heavy flavor decays in p-Pb collisions shows the long-range azimuthal correlation which may be due to the gluon saturation or collective expansion of the system [4]. In the dielectron mass spectrum, electron-positron pairs from semi-leptonic decays of heavy quarks are dominant at $m_{ee} > 1$ GeV/c^2. The contributions from $c\bar{c} \rightarrow e^+e^-$ and $b\bar{b} \rightarrow e^+e^-$ can be separated with the invariant mass and pair p_T.

ALICE is one of the main experiments at the LHC and is dedicated for heavy ion collisions. The Transition Radiation Detector (TRD) is one of the detectors in ALICE, which provide the electron trigger. The integrated luminosity of the TRD triggered data in p-Pb collisions is 1.4 nb^{-1}. It corresponds to 20 times larger statistics than the minimum bias data (0.067 nb^{-1}). This report presents the status of the dielectron analysis with TRD triggered data.

2. TRD trigger performance

TRD consists of 6 layers of MWPCs and the radiators (polypropylene fiber mat) for the transition radiation [5]. It can be used for the electron identification at $p_T > 1$ GeV/c. During p-Pb runs, two different electron triggers with TRD were available. One (HSE) is the single electron trigger with an electron identification cut for $p_T > 3$ GeV/c. The other is the single electron trigger with tighter online electron identification for $p_T > 2$ GeV/c (HQU). Data taken by both triggers are used in the analysis.
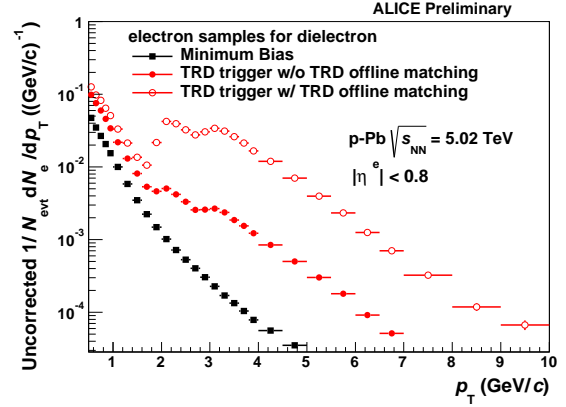
Figure 1: Single electron yields for the minimum bias trigger and TRD trigger.
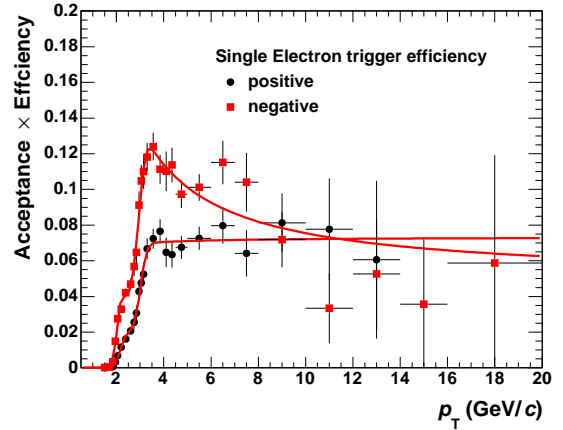
Figure 2: TRD trigger efficiency for the single electrons and positrons.

Figure 1 shows the number of electrons per events in minimum bias data and TRD triggered data. The event after rejections of HSE and HQU triggers are 1/170 and 1/240 of the original, respectively. To reject the events triggered by the late conversions, which are created at larger radii ($\sim$ 2.5-3 m from the collision point), online TRD tracks are associated with the offline global tracks reconstructed with the Inner Tracking System (ITS) and the Time Projection Chamber (TPC) [6]. This online-offline track matching further rejects the events by a factor of 20.

The trigger efficiency is estimated using the minimum bias data. Figure 2 shows the trigger efficiency calculated as the number of triggered electrons divided by the minimum bias electron samples The online tracking performance of TRD depends on the charge sign due to the Lorentz angle (the angle of drifting electrons with respect to the electric field lines). The trigger efficiency of negative and positive tracks is about 10% and 7%, respectively.
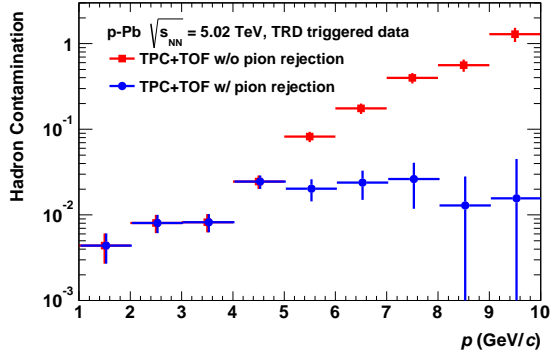
Figure 3: Hadron contamination for electron samples.

3. Electron identification

In the central barrel of the ALICE detector, charged tracks are reconstructed by ITS and TPC [7]. Electrons are identified by deposited charged in the TPC and hadrons are rejected by the ToF detector. ToF is essential to remove contaminations of kaons, protons and deuterons up to 2 GeV/c. The pion rejection cut with dE/dx in the TPC is also applied because TPC dE/dx distributions of electrons and pions merge at high p_T. Figure 3 shows the hadron contamination in electron samples. With the pion rejection cut, the hadron contaminations can be reduced less than 3% up to 10 GeV/c.

4. Pair analysis

In the pair analysis, conversion electrons are removed by using "ϕ_v" cut, where ϕ_v is defined as the angle between the pair plane and the direction of magnetic field. The photon conversion pairs are localized at $\phi_v = \pi$ in the small mass region. Therefore, more than 90% of conversion pairs can be rejected by applying ϕ_v and mass cut.

The background was estimated using the same event like-sign pairs. They should contain not only the combinatorial background but also correlated pairs such as cross pairs which are produced from hadron decays with two e^+e^- pairs in the final state, Jet contribution, and $B\overline{B}$ oscillation. Due to the acceptance difference between unlike-sign pairs and like-sign pairs, acceptance correction is needed. In this analysis, the acceptance correction factor is obtained using the mixed events as following,

$$R = \frac{N_{+-} + N_{-+}}{2\sqrt{N_{++}N_{--}}}_{mixed}, \quad (1)$$

where, N_{+-} and N_{-+} are the number of mixed unlike-sign pairs and N_{++} and N_{--} are mixed like-sign pairs. Figure 4 shows the invariant mass distributions of the unlike-sign pairs and like-sign background, while Fig. 5 shows the subtracted yield in p-Pb collisions. The clear J/ψ peak is seen. The signal-to-background reaches 1 at $m_{ee} > 5$ GeV/c^2. The extraction of the invariant yield up to 10 GeV/c^2 is ongoing.

5. Summary and outlook

The subtracted yield up to m_{ee} = 10 GeV/c^2 is obtained with the TRD triggered data. The single electron trigger efficiency of TRD trigger is extracted to be 10%. As a next step, the invariant cross section of the dielectron spectrum will be extracted. $c\bar{c}$ and $b\bar{b}$ cross section will also be deduced with the help of theoretical models.
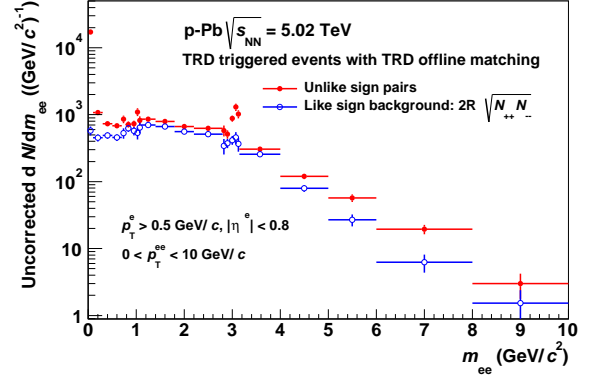
Figure 4: The unlike-sign pairs and the like-sign background spectrums for the TRD triggered data.
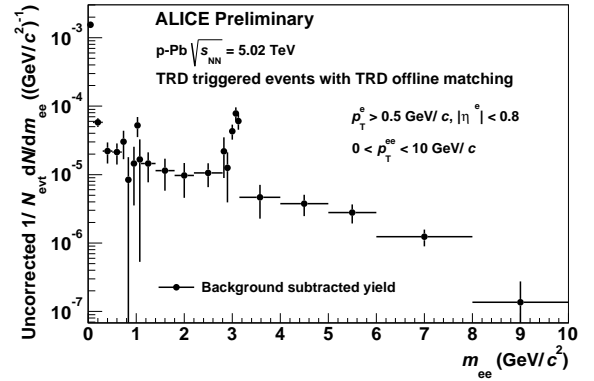
Figure 5: The dielectron spectrum after background subtraction for the TRD triggered data.

References

[1] H. Fuji, K. Watanabe, NPA 920, 78-93 (2013)
[2] A. Adare et al. (PHENIX Collaboration), Phys. Rev. C 89, (2014) 034915.
[3] ALICE Collaboration, arXiv:1405.3452 (2014).
[4] E. Pereira de Oliveira Filho, arXiv:1404.3983v2 (2013) NPA in press.
[5] J. Klein, NIMA 706 23-28 (2013).
[6] ALICE TRD Technical Design Report, Tech. Rep. CERN/LHCC 2001-021 (2001).
[7] F. Carminati et al., J. Phys. G: Nucl. Part. Phys. 30 1517 1763 (2004).

Accelerator and Instrumentation

Study of Space-charge effect on IBF in GEM-TPC detector

K. Yukawa, H. Hamagaki, T. Gunji, Y.L. Yamaguchi, and K. Terasaki

Center for Nuclear Study, Graduate School of Science, the University of Tokyo

1. Introduction

The Multi Wire Proportional Chamber (MWPC) is widely used for the amplification stage in a Time Projection Chamber (TPC). To prevent ions created in the amplification region from drifting back into the drift space (IBF, Ion BackFlow), gating grid system is widely used in the TPC. One of the drawbacks of the gating grid system in the TPC is the limitation of the data taking rate. Therefore, it is necessary to develop another technology to suppress the IBF in the high rate experiments.

Micro-Pattern Gaseous Detectors (MPGD) are the possible solutions to achieve sufficiently low IBF and high rate capability. Gas Electron Multiplier (GEM) can absorb positive ions on its electrode by applying relatively low electric field above GEM.

In this study, we study the capability of the suppression of the IBF with GEM and its dependence on the space-charge density in the drift space.

2. Experimental Setup
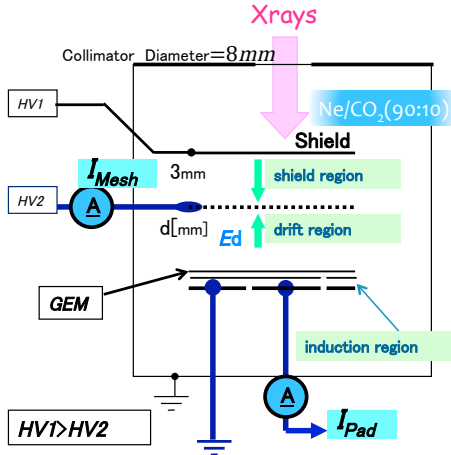
Figure 1: Setup for the measurements

The setup is shown in Fig. 1. The system consists of shield region, drift region, amplification region, and induction region. The induction region is the space between the readout pad and the bottom of GEM, and the length is 2 mm with the electric field of 3 kV/cm. The amplification region is between top and bottom electrodes of GEM, and field strength is the order of 50 kV/cm (ΔV_{GEM}/GEM thickness). The drift region is a space between top electrode of GEM and mesh, and its length d and the electric field E_d are varied in the measurements. The shield region is the space above mesh and the length is 3mm with the the opposite electric field of $-E_d$. Primary electrons created in the shield region do not contribute to the multiplication of the GEM.

The size of GEM is 10×10 cm^2 and the size of pad is 3×3 cm^2. The chamber is filled with Ne/CO$_2$ (90/10, 1atm), and the X-ray is injected perpendicular to GEM foil and collimated by 8 mm diameter.

I_{pad} and I_{mesh} are the current of pad and mesh respec-

tively. We define $I_{\mathrm{drift}}=I_{\mathrm{mesh}} - I_{\mathrm{prim}}$, where I_{prim} is the current of the primary ions at the mesh. The gas gain and IBF are defined as follows:

$$gain = \frac{I_{\mathrm{pad}}}{I_{\mathrm{prim}} \cdot \frac{d}{d+3mm}} \quad (1)$$

$$IBF = \frac{I_{\mathrm{drift}}}{I_{\mathrm{pad}}} \quad (2)$$

3. Space-charge effect on IBF
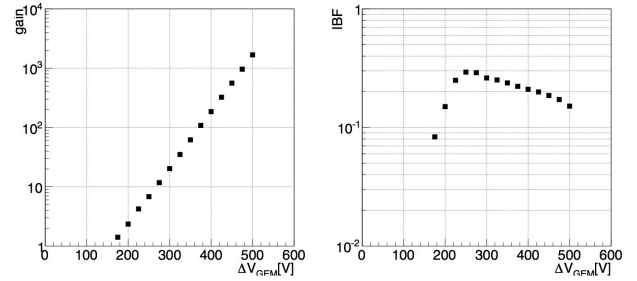
Figure 2: Gain and IBF of GEM

Gain and IBF as a function of ΔV_{GEM} is shown in shown in Fig. 2. The drift length and drift field are 3mm and 400 V/cm in these measurements. Gain reaches 1600 at $\Delta V_{GEM} = 500$ V and IBF decreases as ΔV_{GEM} increases and reaches 15%.

Left of Fig. 3 shows IBF as a function of the space-charge density for different drift length, where the space-charge density is estimated by Eq. (3), where A and v_{ion} are the spot size of the X-ray and ion mobility of Ne$^+$ in Ne/CO$_2$ (90/10), respectively,

$$\rho = \frac{I_{\mathrm{drift}}}{A \cdot \mathrm{v}_{\mathrm{ion}}} \quad (3)$$

Here A is a beam profile ($A = \pi r^2$, $r = 0.4$ cm). In these measurements, ΔV_{GEM} and E_d are fixed to be 500 V and 400 V/cm, respectively, and the rate of X-ray is varied. The velocity of Ne$^+$ ion in Ne gas is $v_{\mathrm{ion}} = 4.08E_d$ [V/cm]. We haven't taken into account the effect of drifting CO$_2^+$ ions [1].

Right panel of Fig. 3 shows the IBF as a function of ρd. One can see that the trend is better scaled by ρd and that the decrease of the IBF starts at $\rho d \sim 3 \times 10^4$ [fC/cm^2].

To consider the reason of sudden reduction of IBF, we roughly calculate the electric field with space-charge in drift region by assuming space-charge density is uniform. The electric field can be calculated as the following:

$$\frac{d^2\phi(z)}{dz^2} = -\frac{\rho}{\varepsilon} \quad (4)$$

$$E(z) = E_d - \frac{\rho d}{2\varepsilon} + \frac{\rho}{\varepsilon}z \quad (5)$$
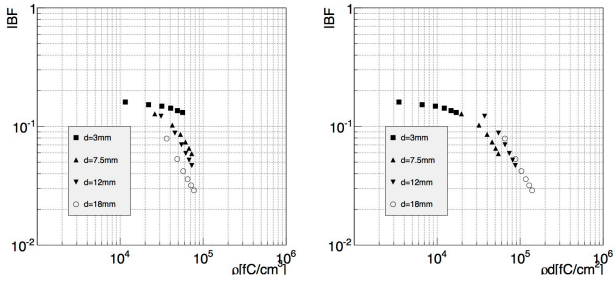
Figure 3: Space-charge dependence of IBF: ΔV_{GEM} and E_d are set to 500 V and 400 V/cm respectively.

where z is the distance from top of GEM. Fig. 4 shows IBF as a function of $\frac{\rho d}{2\varepsilon E_d}$. One can see that the trend is very similar for different E_d and onset of decrease of IBF is around $\frac{\rho d}{2\varepsilon E_d} \sim 0.3$, which doesn't strongly depend on E_d.
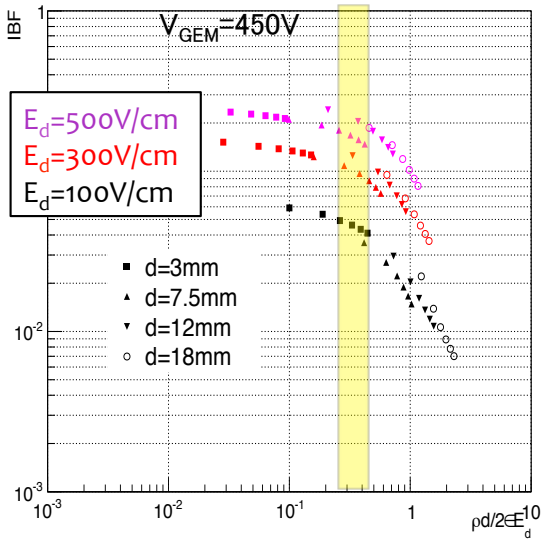
Figure 4: IBF dependence on space-charge

4. Summary and outlook

We studied the capability of the IBF suppression by GEM. We found that IBF strongly decreases as space-charge density gets higher and the onset of decrease of IBF is characterized as functions of drift length, drift field, and rate of X-ray. The onset starts at $\frac{\rho d}{2\varepsilon E_d} \sim 0.3$ and this doesn't depend on d and E_d.

We are going to examine the space-charge effect for the MicroMegas [2] detector which has different surface structure. We will evaluate IBF as a function of space-charge density for multi-GEM layers and GEM + MicroMegas systems.

References

[1] ALICE Collaboration, Technical Design Report of Upgrade of the ALICE Time Projection Chamber, CERN-LHCC-2013-020 (2013)

[2] Y. Giomataris *et al.*, Nucl. Instr. Meth. A376 (1996) 26-35

Reduction of Ion Backflow with COBRA-GEM and Application for the TPC

K. Terasaki, H. Hamagaki, T. Gunji, and Y. L. Yamaguchi

Center for Nuclear Study, Graduate School of Science, University of Tokyo

Table 1: The geometries of COBRA-GEMs (in μm).

	Insulator thickness	Hole pitch	Hole Diameter	Rim width	Metal width
COBRA200	200	577	150	50	50
COBRA100	100	400	100	0	50

1. Introduction

Secondary ions generated in an electron-avalanche process in gaseous detectors go back into the drift space, which is called as "Ion Backflow (IBF)." Because IBF distorts the electric field in the drift space, reduction of IBF is essential for the TPC in order to keep the performance of charged particle tracking and particle identification. Gating grid system is widely employed to reduce the IBF, however, operation of the gating grid system limits the data taking rate up to the order of kHz. Therefore, it is not suitable for high rate experiments. The rate of heavy-ion collisions at the LHC will be the order of 10 kHz in 2019. ALICE-TPC plans to read out the data of Pb-Pb collisions continuously, which requires IBF to be less than 1.0% at gain ~ 2000 in Ne/CO_2 (90/10) [1].

Gas Electron Multiplier (GEM) has some advantages in the point of high rate capability and suppression of IBF with stack configuration. COBRA-GEM, which was originally developed for RICH detector by F.D. Amaro *et al*. [2] has two isolated electrodes on a surface. By applying potential difference between these two electrodes, ions can be effectively trapped with one electrode and further reduction of IBF is achievable. We developed COBRA-GEMs for the application of the TPC and studied its basic performance.

2. Thick COBRA-GEM

A microphotograph of the surface and a schematic view of a cross section of COBRA-GEM are shown in Fig. 1. IBF can be efficiently reduced by applying a potential difference between these two COBRA electrodes, ΔV_{AC}. Here, ΔV_{AC} is defined as $V_{in} - V_{out}$, where $V_{in,out}$ are the potential at inner and outer COBRA electrodes, respectively. Two types of COBRA-GEMs were developed in collaboration with SciEnergy Co., Ltd. [3]; One has 200-μm-thick insulator (COBRA200) and the other has 100-μm thickness (COBRA100) (see Table 1). The glass epoxy laminate (FR5) and Liquid Crystal Polymer (LCP) are used as an insulator for COBRA200 and 100, respectively.

Figure 2 shows the drift lines of ions starting from bottom of COBRA-GEM for COBRA200 in Ar/CO_2(70/30)
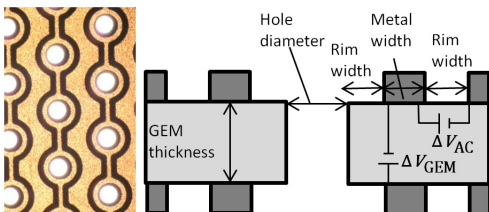
calculated by Garfield [4]; The left and right panels are for the case of $\Delta V_{AC} = 100$ and 300 V with the voltage across the GEM (ΔV_{GEM}) of 850 V. As is expected, higher ΔV_{AC} is more effective for the suppression of IBF.
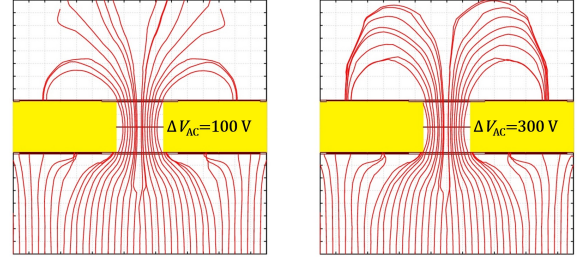
Figure 2: The drift lines of ions starting from bottom of COBRA-GEM (COBRA200) at $\Delta V_{GEM} = 850$ V for the case of $\Delta V_{AC} = 100$ V (left) and 300 V (right).

3. Measurement Setup

Figure 3 shows a schematic view of the measurement setup. The chamber gas is Ne/CO_2 (90/10) at atmospheric pressure and the X-ray beam is injected perpendicular to the surface of COBRA-GEM. The drift length, between the mesh and the top of GEM, is 3 mm. The induction length, between the bottom of the last GEM and the anode pad is 2 mm. The size of anode pad is 10×10 cm^2 and it has a isolated readout pad (3×3 cm^2) at the center.

The electric fields in the drift and induction regions, $E_{d,i}$ are 0.4 kV/cm and 3 kV/cm, respectively. Then, two different configurations are adopted; One single COBRA-GEM is installed to measure its characteristics (Fig. 3(a)) and one standard GEM and two COBRA-GEMs to investigate the performance with stack configuration (Fig. 3(b)).

Gain is calculated as $I_a/(I_c^0/2)$ and IBF is defined as $(I_c - I_c^0)/I_a$, where I_c and I_a are the current readout at the mesh and the pad plane, respectively, and I_c^0 is the mesh current from primary ionization. Energy resolution is determined as peak width (standard definition) / position of peak with ^{55}Fe source.

4. Gain and IBF with the stack configuration

Figure 4 shows gain and IBF for the stack configuration of COBRA200 as a function of ΔV_{AC}. ΔV_{GEM} of the standard GEM was 200 V and those of two COBRA-
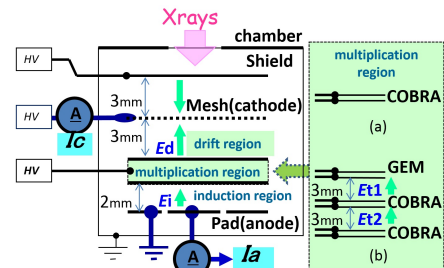
Figure 3: A schematic view of the measurement setup: (a) the single COBRA configuration, (b) the stack configuration.

Figure 1: A microphotograph of COBRA-GEM surface (left). Cross-section drawing of COBRA-GEM (right).

GEMs were varied as follows; $(\Delta V_{\mathrm{GEM2}}, \Delta V_{\mathrm{GEM3}}) = (430\,\mathrm{V}, 430\,\mathrm{V})$, $(350\,\mathrm{V}, 510\,\mathrm{V})$, and $(260\,\mathrm{V}, 590\,\mathrm{V})$. The primary current density was tuned to match the value expected in 50 kHz Pb-Pb collisions. At $\Delta V_{\mathrm{AC}} = 250$ V, IBF reached 0.1-0.5% with gain around 1000.
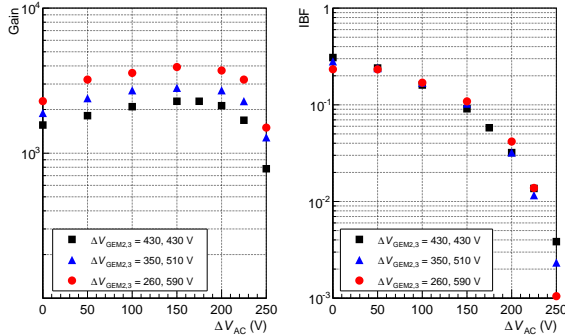
Figure 4: Gain (left) and IBF (right) for the stack configuration of COBRA200 as a function of ΔV_{AC}. $\Delta V_{\mathrm{GEM2,3}} = 430, 430$ V (square), $350, 510$ V (triangle), $260, 590$ V (circle).

ΔV_{AC} dependence of gain has been evaluated by the simulations based on ANSYS [5] and Garfield++ [6]. The increase of gain (with $\Delta V_{\mathrm{AC}} < 150$ V) is described by the increase of the field inside the hole due to a higher ΔV_{AC}. The gain decrease (with $\Delta V_{\mathrm{AC}} > 150$ V) is due to the fact that the electric field above GEM starts to be reversed and that less number of seed electrons reach the hole of GEM.

5. Charging-up effect and energy resolution

Measurements of long-time stability of gain were performed with the stack configuration for both COBRA-GEMs. The cathode mesh was replaced by a 10×10 cm^2 cathode pad. ^{55}Fe source was placed in the chamber.

The gas gain of COBRA200 gradually increased until $t \sim 200$ min. This was due to the charging-up effect. After gain reached the plateau, energy resolution became around 20%, which was worse by a factor of 2 compared to the one achieved with a triple-standard-GEM configuration. This worse energy resolution was also observed in the single COBRA-GEM measurements. From the simulation studies, the worse energy resolution with COBRA200 is due to the fact that the collection efficiency of seed electrons is not 100% because of the large pitch between GEM holes. Since the collection efficiency and the gain depend on the relative position between seed location and the hole of GEM, the deviation of effective gain can be large. The gain distribution given by the simulation studies for the single COBRA200 is about 14%, which is about twice worse than that for single standard 100 μm-thick GEM (6%).

The charging-up effect was more clearly visible for CO-BRA100. Figure 5 shows gain and energy resolution for the single COBRA100. The horizontal axis shows the accumulation of the seed electron density. It shows that we need to wait until the charge density of the order of 10^{-7} C/cm^2 is accumulated on COBRA-GEM, which takes ~ 1 day in 50 kHz Pb-Pb collisions. Simulation studies reveal that the charging-up effects happen at the insulator surface between inner and outer electrodes and the trend of the gain as a function of the total charge density is reproduced. It shows that the collection efficiency of electrons is almost zero at the beginning of the irradiation and incremented as
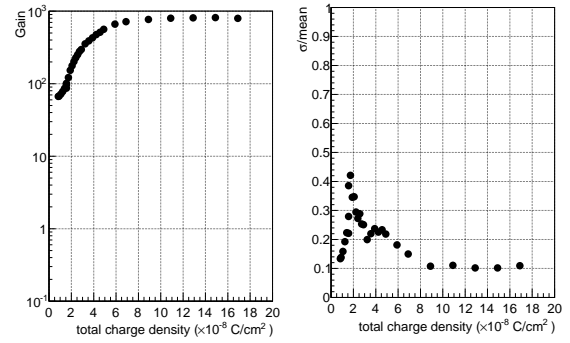
Figure 5: Gain (left) and energy resolution (right) in the single configuration of COBRA100 as a function of the total charge density of electrons produced by the strong X-ray.

the number of electrons on insulator increases because the potential around the insulator becomes lower.

6. Summary and outlooks

Two types of COBRA-GEMs with different geometries have been fabricated and IBF reaches 0.1-0.5% with the stack configuration. Measurement of long-time stability of gain shows that gain varies significantly due to the charging-up effect. Simulation studies show that the collection efficiency of seed electrons depends on their positions and that bare insulator between two electrodes is responsible for the charging-up effect. For the application in the TPC, further investigation of the charging-up effect, energy resolution, and the optimization of the geometry of COBRA-GEM is required.

References

[1] ALICE Collaboration, "Technical Design Report of Upgrade of the ALICE Time Projection Chamber," CERN-LHCC-2013-020 (2013)
[2] F. D. Amaro *et al.*, JINST **5** (2010) P10002.
[3] SciEnergy Co., Ltd. http://www.scienergy.jp/.
[4] Garfield: http://garfield.web.cern.ch/garfield/.
[5] ANSYS: http://www.ansys.com/
[6] Garfield++: http://garfieldpp.web.cern.ch/garfieldpp/

Development of SOI pixel sensor for radiation monitor

Y. Sekiguchi, Y. Arai[a], H. Hamagaki, and T. Gunji

Center for Nuclear Study, Graduate School of Science, University of Tokyo
[a]Institute of Particle and Nuclear Studies, High Energy Accelerator Research Organization (KEK)

1. Introduction

We have developed a prototype SOI pixel sensor, called RADPIX, for a radiation monitor. This is based on the silicon-on-insulator (SOI) pixel CMOS technology being developed by Y. Arai et al [1]. The RADPIX is to be used for natural environmental radiation measurements. The RADPIX has many advantages in the cost and the parasitic capacitance over hybrid pixel detectors. The aim of the RADPIX is to count the rate of the radiation and to visualize the hit pattern. The analysis of hit patterns allows to identify the components of unknown radiation field, similar to the strategy described in [2]. There are two main features in RADPIX; one is the leakage compensation circuit in each pixel for long exposure, and the other is both analog and digital readout from each pixel to develop a particle identification. Figure 1 shows the schematic view of the Nested-Well structure SOI detector (p-in-n type sensor). The RADPIX is a monolithic pixel detector that consists of a thin CMOS readout array (40 nm, 10 Ω), a buried oxide layer (200 nm), and a thick high resistivity Si-sensor (260 μm, 700 Ω) vertically on a single chip. The holes generated within the fully depleted bulk drift onto the buried p-well (BPW) by application of a sufficiently high positive voltage to a backside and result in the modulation of the channel current. The buried n-well (BNW) is fixed to 1.8 V to reduces the back gate effect and the sensor cross talk. The result of basic performance test is reported in this paper.
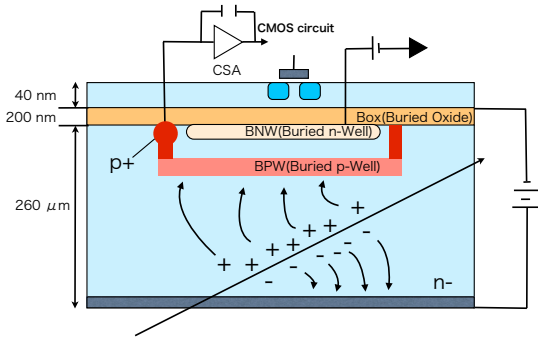
Figure 1: A schematic view of SOI structure with BPW and BNW.

2. Detector Specification

RADPIX is fabricated with 0.2 μm FD-SOI CMOS technology developed by LAPIS Semiconductor. Co., Ltd. [3]. It is 2.9×2.9 mm^2 size and active area is 1mm x 1mm. There are 32×32 pixels, where each pixel has a size of 40 μm $\times$ 40 μm. For comparison sake, the test chip has 4 different kinds of preamplifiers simple; source follower (simple SF), low gain and high gain charge sensitive amplifiers (CSA), and high gain CSA with current mirror. A microscopic photo is shown in Fig. 2. The analog and dig-

ital signal signals are readout through each column buffer and readout pixel is selected by the address decoder. Wire-ORed digital signals are used as trigger. Figure 3 shows the schematics diagram for the CSA type pixels. Leakage current compensation circuit is employed in the charge sensitive preamp to measure the radiation for a long time [4]. The high gain CSA type and the low gain CSA type have 1 fF and 5 fF feedback capacitors, respectively. Two inverter-chopper type comparators are used to generate a digital output. The comparator output is latched by SR latch circuit and also delayed to store the analog signal.
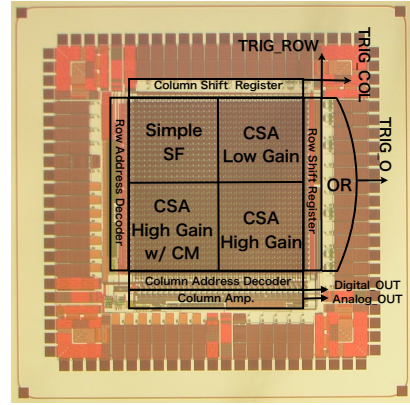
Figure 2: A microscopic photo of RADPIX.
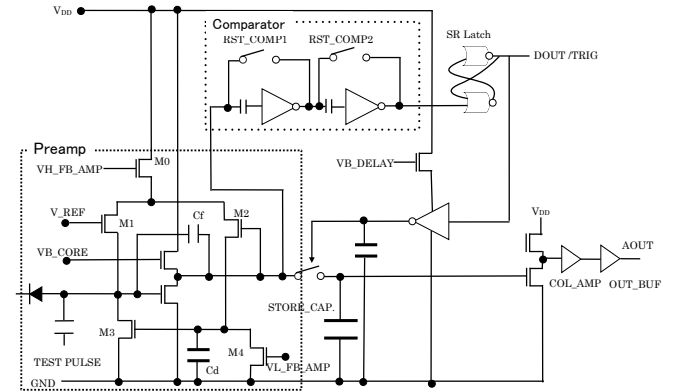
Figure 3: Schematics of for the high gain CSA type and the low gain CSA type.

3. Results
3.1. Gain

$$Gain[\mu V/electron] = \frac{V_{out} \times e}{4[\text{fF}] \times V_{\text{test}}} \quad (1)$$

Sensor nodes are connected to a test input with 4 fF capacitor (See Fig. 3). A negative output pulse (V_{out}) result

from positive input (V_{test}). The gain is calculated by Eq. (1). e is the elementary charge. Figure 4 shows the pixel-to-pixel gain variation in the low gain CSA type and the high gain CSA type at $V_{test} =200$ mV. The average gain is 20 μV/electron (RMS~1.3) and 80 μV/electron (RMS~5.1) for the low gain CSA type and the high gain CSA type, respectively. It shows a good pixel-to-pixel gain uniformity.

Figure 6: Pulse height histogram of Cd (left) and Ba (right).

Figure 4: The pixel-to-pixel gain variation in the low gain CSA type (Upper) and the high gain CSA type (down).

3.2. Comparator

We reset the comparator by adjusting V_{REF} (See Fig. 3). When V_{REF} is set to threshold voltage (reset voltage), this comparator is inactive (active). The difference between the threshold voltage and the reset voltage is denoted as Vth. Figure 5 shows the number of events triggered by the comparator as a function of threshold voltage without any signal inputs. To keep the noise hit rate significantly low Vth should be set at 150 mV (the low gain CSA type) and 350 mV (the high gain CSA type). These voltages correspond to the energy of gamma-ray of 26 keV and 15 keV for the low gain CSA type and the high gain CSA type, respectively. The reason of the large noise is under investigation.

Figure 7: The calibration with Cd and Ba.

4. Summary

We are developing a prototype detector for radiation monitor, called RADPIX. Individual leakage current compensation circuit is integrated to be able to measure for a long time. RADPIX is designed to readout both analog and digital signals. We evaluated the basic performance for the high and the low gain CSA type. The gain is ~20 μV/electron and ~80 μV/electron for the high gain CSA type and the low gain CSA type, respectively. Threshold voltage must be set relatively high value at present. The reason is under investigation. By irradiating with [109]Cd and [133]Ba X rays and the gain is consistent with the one with the test pulse.

References

[1] Y. Arai, et al. , Nucl. Instr. and Meth. A636 (2011) 31
[2] T. Holy, et al., Nucl. Instrum. Methods A 591, 287-290 (2008) .
[3] Lapis Semiconductor Co. Ltd., http://www.lapis-semi.com/en/
[4] F. Krummenacher, Nucl. Instrum. Methods A 305, 527-532 (1991)

Figure 5: The number of the digital output counts with different threshold voltage for four pixels. (These pixels are the third pixel from the outside for column and law).

3.3. Response to the radiation

We irradiated RADPIX with 22.4 and 31 keV X rays from [109]Cd and [133]Ba sources, respectively. Figure 6 shows the pulse height histogram for the low gain CSA type. As shown in Fig. 7, the gain is ~18μV/electron by fitting two energy points. The gain is consistent with the one performed with test pulse.

CNS Active Target Development in FY2013

S. Ota, H. Tokieda, C.S. Lee, Y.N. Watanabe[a] A. Corsi[b], M. Dozono[c], S. Gotanda[d] T. Gunji,
H. Hamagaki, S. Kawase, R. Kojima, Y. Kubota, Y. Maeda[d] S. Michimasa, A. Obertelli[b], H. Otsu[c]
C. Santamaria[b], M. Takaki, T. Uesaka[c], H. Yamaguchi, J. Zenihiro[b], E. Takada[e]

Center for Nuclear Study, Graduate School of Science, University of Tokyo
[a] *Department of Physics, the University of Tokyo*
[b] *Service de Physique Nucéaire (SPhN), CEA-Saclay*
[c] *Nishina Center for Accelerator-Based Science, RIKEN*
[d] *Department of Applied Physics, Miyazaki University*
[e] *Heavy Ion Medical Accelerator in Chiba, National Institute of Radiological Science*

Equation of State (EoS) of nuclear matter governs the bulk property of nuclei in femto-scale and the property of neutron stars in universe at the same footing. Isoscalar Giant Monopole Resonance (ISGMR) is related to the incompressibility of the nucleus, which is one of the parameters in the EoS. The ISGMR can be studied via the inelastic scattering (d, d'). To extract the ISGMR strength, the differential cross-section at the forward angle is important since the monopole strength has peak at the forward angle. As well as the forward angle scattering, the wide angular acceptance is required for the multipole decomposition analysis to deduce the ISGMR strength distribution in the continuum region above the particle emission threshold.

We are developing the gaseous active target system, CNS Active Target (CAT) to measure the low-energy recoil particles corresponding to the forward angle scattering [1]. The CAT consisted of the time projection chamber (TPC) and NaI detector array surrounding the field cage of TPC. It was operated with 1-atm deuterium gas in the measurement of (d, d') reaction on ^{14}O nucleus. The status of the data analysis is reported by Tokieda *et al.* [2]. The CAT will be employed in the series of the ISGMR measurements in the $A = 132$ isobar such as ^{132}Sn measurement at RIBF in RIKEN and ^{132}Xe measurement at HIMAC in NIRS. In this report the developments in FY2013 toward these measurements will be summarized.

The CAT has been modified to have high sensitivity to the forward angle scattering and to have smaller inactive gap between the TPC and the solid detector [1]. The NaI detector array surrounding the TPC has been replaced by Si detector array to reduce the inactive region produced by the entrance window of the NaI detector. In order to measure the low-energy recoil particle at the forward angle scattering, the gas pressure was optimized. The rough yield estimation was performed for the deuteron inelastic scattering off ^{132}Sn. Figure 1 shows the relative yield deduced using the Monte-Carlo simulation without the tracking efficiency for various pressure settings. Lower gas pressure provides the higher efficiency for the forward angle scattering. However, the number of target particles becomes smaller with the lower gas pressure. The gas pressure of 0.4 atmosphere was chosen to have the sensitivity at around the 2-degrees in the center-of-mass frame and to have the moderate number of target particles. In the low-pressure gas, the Thick Gas Electron Multiplier (THGEM) is known to have higher gas gain. The gas gain of THGEM in low pressure gas has been studied by C.S. Lee *et al.* [3] and the achieved gain was 10^4 with three layers of THGEMs, which is the typical value for the detection of high energy recoil deuterons. The other
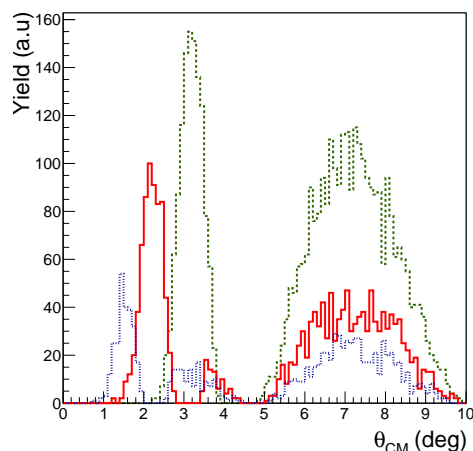
Figure 1: Relative yeld estimation of the deuteron scattering off ^{132}Sn assuming the angular distribution of the 0-th order of spherical Bessel function and the tracking efficiency of 100%. Blue dotted, red solid and green dashed line show the estimated acceptance for 0.2-, 0.4- and 1-atm deuterium gas, respectively.

gas properties such as drift velocity, diffusion and the effect of oxygen contamination are reported by Y.N. Watanabe *et al.* [4].

The test experiment (HIMAC collaborative research 12H307) for the low-pressure operation of CAT was performed at HIMAC in Chiba. Stable nucleus beam of ^{132}Xe was directed into the CAT at the incident energy of 100 MeV/u and 190 MeV/u. The trajectory of recoil particle was successfully measured even in the cloud of the delta electrons produced by the beam particle. Two MWDCs were located at upstream of the CAT to provide the reference trajectory for the evaluation of the resolution and the effect of the distortion of the electric field by the space charge created by the heavy ion beam. The data analysis is in progress.

The measurements of the ISGMR in $A = 132$ isobar will be performed with high intensity heavy ion beam at the incident energy of 100 MeV/u. The goal of the intensity of ^{132}Xe stable beam is 10^6 particles per spill (pps), which is almost equivalent to 1 MHz. The energy loss of ^{132}Xe in 0.4-atm. deuterium gas is 140 keV/mm. If the electrons created by the ionization are multiplied by THGEM with 10^4 gain, the current at the last stage of the multipli-

cation part become 56 μA along the 10-cm flight path in active area. This current value is too high for the stable operation of the THGEMs. We need to reduce the effective gain for the beam region by two orders of magnitude with keeping the gain for the recoil region high enough. To overcome this difficulty, we tried two different methods to reduce the effective gain along the beam path. One method is to change the hole and pitch size of THGEM in the region and the other is to introduce a meth grid along the beam path. It was turned out from the offline measurement that the change of hole and pitch size was not enough to reduce the effective gain. The other method is to set a mesh grid. It has been turned out from the experiment performed at HIMAC same as described previously that the mesh grid can reduce the effective gain by two orders of magnitude successfully and the intensity of 10^5 pps can be used in the measurement. However the change of the voltage value of THGEM was observed during the irradiation of higher intensity beam such as 10^6 pps. The detail of this measurement will be reported by C.S. Lee *et al.* [5]. It was also found that the energy resolution became worse since the number of the primary electrons was reduced by the absorption by the mesh grid. In order to solve these problems, the modification of the protection circuit to reduce the voltage drop at this circuit and the new electrode structure of THGEM will be introduced in near future.

In summery, the CAT was operated with low-pressure deuterium gas at 0.4 atmosphere for the first time and the trajectory of recoil particle was measured in deuteron scattering off ^{132}Xe. The gas properties of low-pressure deuterium gas was studied for the first time. The effective gain of THGEMs along the beam path was successfully reduced by using the mesh grid although the energy resolution became worse. The farther development for the gain reduction with keeping energy resolution will be performed toward the measurements of ISGMRs in ^{132}Sn and ^{132}Xe with high intensity beams.

References

[1] S. Ota *et al.*, CNS Annual Report 2011, (2013), 70-71.
[2] T. Tokieda *et al.*, to be published in CNS Annual Report 2013, (2014)
[3] C.S. Lee *et al.*, JINST 9, C05014 (2014)
[4] Y.N. Watanabe *et al.*, to be published in CNS Annual Report 2013, (2014)
[5] C.S. Lee *et al.*, to be published in CNS Annual Report 2013, (2014)

Development of a dual gas gain multiplication at CNS Active Target for high-intensity beam conditions

C. S. Lee[a,b] S. Ota[a], R. Kojima[a], Y.N. Watanabe[c], H. Tokieda[a], and T. Uesaka[b]

[a]*Center for Nuclear Study, Graduate School of Science, The University of Tokyo*
[b]*Nishina Center for Accelerator-based Science, RIKEN*
[c]*Department of Physics, Graduate School of Science, The University of Tokyo*

1. Introduction

We are developing a GEM-TPC-based gaseous active target with a pure deuterium gas, called CNS Active Target (CAT) [1], for the measurement of deuteron inelastic scattering. The CAT is operated with a low-pressure (0.2-0.5 atm) deuterium gas for measuring the scattering to the forward angle closer to $0°$. Three 400-μm Thick Gas Electron Multipliers (THGEMs) are used for the CAT to achieve a gas gain of 10^4 in a low-pressure deuterium gas ; its performance was investigated for the first time in our previous work [2, 3]. The gas gain of THGEMs is set to 10^4 in order to detect high-energy recoil particles (dE/dx ≈ 5 keV/cm for ^{132}Sn(d,d') at 100 MeV/u with 0.4-atm D_2) as well as low-energy recoil particles (dE/dx ≈ 50 keV/cm for the same condition). However, this gain is too large for the measurement of beam particle since the energy loss of heavy ion beam such as ^{132}Xe is 10-100 times larger than that of recoil particle and the high intensity beam irradiation with such a high gain causes the instability of the THGEMs.The effective gas gain along the beam trajectory (BT) area should be reduced by an order of 10-100, keeping the effective gas gain in the region where the recoil particles (RP) are measured.

2. Development of a dual gas gain multiplication
2.1. Dual-Gain THGEM : DGGEM

A new type of THGEM, called DGGEM (Dual-Gain THGEM), was manufactured via mechanical drilling. Table 1 shows the design of DGGEM which is investigated in this work. The DGGEM was used to study the dependence of the gain on the hole diameter.

Property	BT region	RP region
Thickness [μm]	400	400
Hole diameter [μm]	450	300
Pitch [μm]	700	900

Table 1: Design of DGGEM with a comparison between Beam Trajectory (BT) and Recoil Particle (RP) regions.

Considering a weaker electric field strength and a smaller Townsend coefficient at the larger hole diameter, a gas gain in the RP region is expected to be lager by a factor of four than that in the BT region with a single DGGEM. Figure 1 shows the obtained gain curves in single, double, and triple DGGEM layer setups as functions of the induction field strength $E_{induction}$ in kV/cm/atm. The measured difference of gas gain between the BT and RP regions was much smaller than expected. The dependence of the gas gain on the hole diameter seems to be smaller than our expectation. It should be investigated by a full simulation study with various hole diameter conditions.
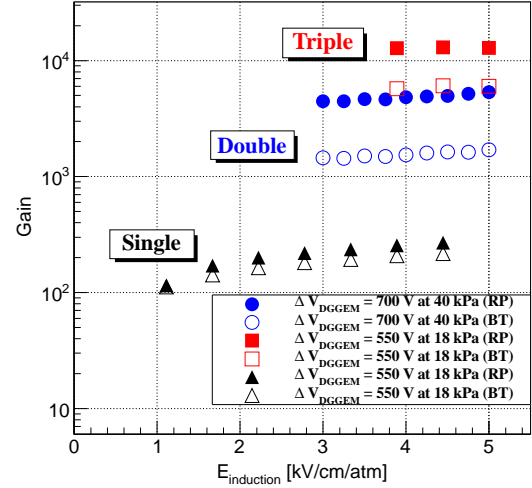
Figure 1: Results for each configuration of DGGEM. For each measurement, the drift field strength was 1 kV/cm/atm and the transfer field strength was 2 kV/cm/atm.

2.2. Combination of THGEM and a mesh-type grid

Another method to reduce the effective gas gain was tested. A mesh grid was put inside the drift region. The mesh grid covered only the area along the beam path. By changing the strength of the electric field in the drift field using the mesh grid along the beam path, a partial gain reduction and a more stable operation of CAT is to be available. An offline test to evaluate the effect of the grid with a triple THGEM configuration was done with a setup as shown in Figure 2. The specification of the mesh grid is summarized in Table 2. The mesh grid with 2-cm width was set 2-mm above the THGEMs along the alpha particle path. Figure 3 shows the gain ratio of BT to RP as a function of the electric field between the mesh grid and the top electrode of THGEM3, E_{grid}. The effective gas gain at RP region was set to around 7000.

Material	SUS304
Type	Mesh
Pitch	0.05 mm
Diameter of wire	18 μm
Aperture ratio	41 %

Table 2: Specification of the grid.

A gain reduction down to 1.6 % was achieved with a combination of the mesh grid and the triple THGEM configuration, and this setup is adopted to the CAT to perform experiments at high-intensity heavy-ion beam conditions. Figure 6 shows the relation between the sampled charges after multiplication and readout pad ID. The widely covered area, pad ID 60-340, corresponds to the entire beam trajec-
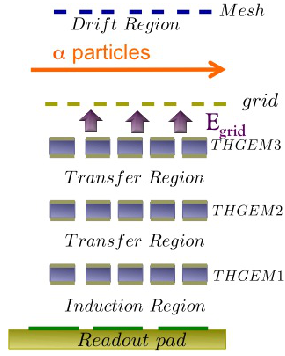
Figure 2: A schematic view of the offline measurement by using an alpha source ^{241}Am.
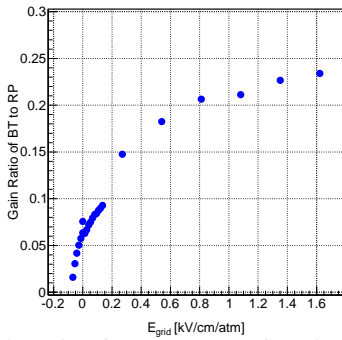
Figure 3: Gain ratio of BT to RP as a function of E_{grid}. Each electric field strength was 1 kV/cm/atm, 2.7 kV/cm/atm and 3.6 kV/cm/atm at the drift, transfer and induction regions, respectively.

tory region and the narrowly covered area, pad ID 130-270, includes the grid. A significant reduction of gain only on the grid area was achieved.

A test experiment was performed with a high-intensity $^{132}_{54}$Xe (100 MeV/u) beam at the HIMAC. Figure 4 shows the obtained gain curve at BT region as a function of E_{grid}. The effective gas gain of the RP region was set to around 5000 and a gain reduction up to 0.86 % was achieved. Figure 5 shows a correlation between the charge resolution and the effective gas gain. The charge resolution is gradually getting worse below the gas gain of about 90, even δQ/Q at a gas gain of 90 is about 10 %.
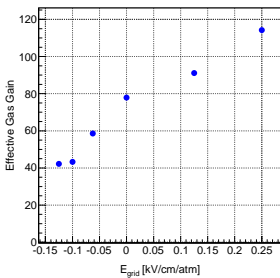
Figure 4: Obtained gain curve at the BT region. The effective gas gain of RP region was set to around 5000.
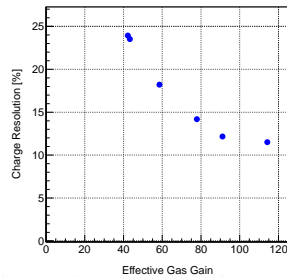
Figure 5: A correlation between the charge resolution and the effective gas gain.
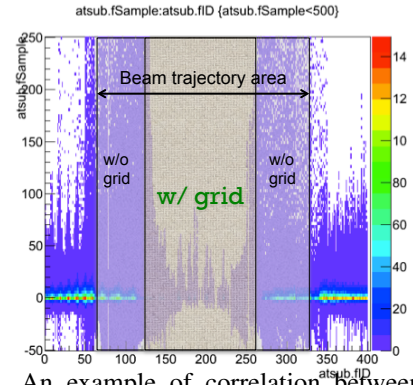
Figure 6: An example of correlation between sampled charges after the multiplication and readout pad IDs with a defocused beam injection. Reduced multiplication of charges is achieved under the grid area.

3. Summary and Outlook

Development of a dual gas gain multiplication at CNS Active Target was tested with i) the Dual-Gain THGEM (DGGEM) and ii) a combination of the mesh grid and the triple THGEM configuration. For the case of DGGEMs, the gain reduction at BT region was insufficient to perform experiments at high-intensity beam conditions, on the other hand, for the case of the mesh grid, a sufficient gain reduction order of about 100 was achieved and its performance test was done by using ^{132}Xe beam. The charge resolution was evaluated and it is getting worse below the gas gain of about 90. The CAT was stably operated via the optimized grid operation under a high-intensity injection of ^{132}Xe beam up to 10^5 particles per pulse, in combination with tuning of the protection circuit for the high-voltage supply. However, further development is needed with the aim of the CAT operation at 10^6 Hz heavy-ion beam condition as well as the gain reduction on the beam trajectory region, keeping the resolution in a few percent level. The drift field is slightly distorted by the grid inside in the mesh grid case, such an effect should be taken into account by further analysis and simulation study.

References

[1] S. Ota et al.: *CNS Annual Report 2011 CNS-REP-90* (2013) 70-71.

[2] C.S. Lee et al.: *CNS Annual Report 2012 CNS-REP-92* (2014) 53-54.

[3] C.S. Lee et al.: *2014 JINST 9 C05014*.

Measurement of Properties of Hydrogen-gas for the Low Pressure Operation of CNS Active Target

Y. N. Watanabe, S. Ota[a], R. Kojima[a], C. S. Lee[a], H. Tokieda[a]

Department of Physics, Graduate School of Science, University of Tokyo
[a] *Center for Nuclear Physics, Graduate School of Science, University of Tokyo*

1. Introduction

We are developing a deuterium gas active-target called CAT (CNS Active Target), to perform the missing-mass spectroscopy via (*d,d'*) reaction with heavy ions in inverse kinematics [1]. To measure low energy recoil particles, CAT is operated in low pressure deuterium gas at around 40 kPa. For the track reconstruction of charged particles, understanding of the properties of drifting electron in an electric field such as drift velocity and diffusion are very important. As a first step, we measured the properties of electron in pure hydrogen gas and compare the measured properties with the properties calculated using Garfield.

2. Measurement and results

2.1. Overview of CAT

CAT consists of a deuterium gas-filled TPC and surrounding silicon detectors. Inside the chamber, there is a height field cage where electric field of around 1 kV/cm/atm is applied into downward direction and electrons drift upward. The height of the field cage is 25 cm and the cross section is 21.5×11.0 cm^2. Above the field cage, triple stacked 10×10 cm^2 THGEMs are installed. Electrons are multiplied by the GEMs and then read by a 10×10 cm^2 by a electrode which has triangular readout pads. The pulse shape is recorded by Flash-ADC. During the measurements, the pressure of CAT was kept around 40 kPa and hydrogen gas was used instead of deuterium gas.

2.2. Measurement of drift velocity

The setup of drift velocity measurement is shown in Fig. 1 (a). An alpha source was set on a flange and two 500 μ-thick 10×10 cm^2 silicon detectors were installed on the opposite side. An acryl cover with three horizontal slit of 2 mm was attached in front of the silicon detectors (see Fig.1 (b)).This cover limited the path of α particles which enters the silicon detectors. We can calculate the drift velocity by measuring the time difference between the pulse at the readout pads and that in the silicon detectors at the slit positions. The measurement was done for three points around E$\sim$ 1 kV/cm/atm.

Fig. 2 shows the relationship between the arrival time of pulse and the z position. In the figure, there are three clusters corresponding to each drift path. Each clusters were fitted by a linear function. In order to estimate the drift velocity, two methods were employed:

- (1) angle of each fitted linear functions

- (2) time difference of each paths at the center of readout pad in z direction

Fig. 3 shows the result of each method. Square points represents the result of method (1), and triangle points are method (2). Garfield calculation are also plotted in the circle points. Although the points at 0.97 keV/cm/atm voltage deviate from the Garfield calculation, the other points are well reproduced by the calculation. This deviation was explained by a small discharge around a feed-through con-

nector, which decreased the field cage voltage and made the drift velocity slower.
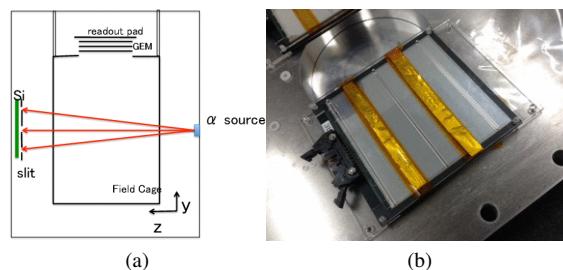
Figure 1: (a) Setup for drift velocity and attachment measurement. An alpha source was put on a flange and two silicon detectors was installed on the opposite side. An acryl cover with three horizontal slit was put in front of the silicon detector to limit the path of alpha particle. (b) Silicon detector with an acryl cover.
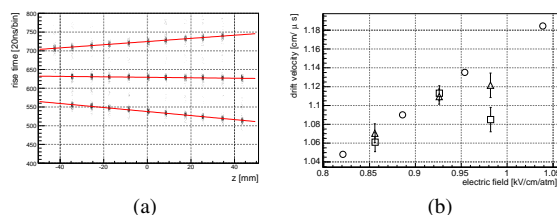
Figure 2: (a) Time difference between the pulse at readout pads and the silicon detectors vs its z position. (b) Measured drift velocity(square points are method (1) and triangle points are method (2) and Garfield calculation results (circle points).

2.3. Measurement of attachment

When electrons drift in a gas, some electrons are captured by gas molecules. The number of electron surviving after drift distance y is

$$N(y) = N(0) \times \exp(-\frac{y}{\eta}),$$

where N(0) is the number of initial electron, and η the is attachment coefficient.

Although hydrogen gas has small attachment coefficient, contaminants such as O_2 or H_2O molecule have the large attachment coefficients. There was a leakage of air and hydrogen gas was contaminated with about 0.5% O_2 and possibly H_2O molecules. This situation was improved by replacing a bad flange, and the contaminants are kept low now. We estimated the effect of attachment before and after exchanging the flange using the same setup as the measurement of drift velocity.

Fig. 4 shows the pulse shape distribution when the O_2 was around 0.5% (a) and 0.03% (b). In Fig.3 (a), the pulse shape becomes smaller due to the attachment with longer drift time. We can estimate the attachment coefficient from

these results. The deduced attachment coefficient was about 0.1 /cm. From the Garfield calculation, the attachment coefficient of the gas mixture of 97.5% H_2, 2.0% N_2 and 0.5% O_2 is around 0.6 /cm. The measurement corresponds to the calculation with 0.1% O_2. The measured value was smaller than calculated one. This difference is considered to be due to the gas flow system and position of O_2 monitor. During the measurement, H_2 gas was continuously flowed and was discharged from the bottom of chamber, which will serve efficient O_2 venting. The O_2 contamination was monitored at the exit of the chamber. Therefore, the actual O_2 concentration in the chamber may be lower than the measured value.

On the other hand, Fig. 3 (b) shows relatively small pulse height decrease and the effect of attachment is now very limited with low contamination of O_2.

(a)   (b)
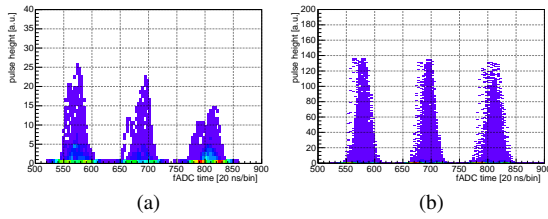
Figure 3: TPC pulse shape distribution taken by fADC. O_2 contamination was 0.5% in (a) and 0.03% in (b). (a) indicates the pulse height decreases with longer drift time when O_2 contamination is large. On the other hand, only small attachment was observed in (b).

2.4. Measurement of transverse diffusion

In an electric field, electrons drift along the electric field in average, but they diffuse from the line due to collisions.The distribution of electrons in transverse direction can be expressed as,

$$f(x) \propto exp(\frac{-x^2}{2(D\sqrt{y})^2}),$$

where D is diffusion constant, x is the deviation from the drift line and y is the drift path length.

To estimate the diffusion constant in low pressure hydrogen gas, let us consider an event in which alpha particles go through the center of the pad(See Fig.4 (a)) . Here, we defined a quantity R which characterises the magnitude of diffusion defined as below:

$$R = \frac{Q_A}{Q_A + Q_B + Q_C},$$

where Q_A, Q_B and Q_C represent the observed charge in pad A, B and C, respectively. Fig. 4 (b) shows the relationship between R and diffusion size, which is equivalent to $D\sqrt{y}$. R becomes small with larger diffusion and vice versa. Therefore, we can estimate the diffusion constant by measuring R and the drift path.

In the measurement, an alpha source was attached to a side wall of CAT, and the data was taken with TPC self-trigger. O_2 concentration was about 0.05%. We measured the R ratio with drift length of 6.0 cm and 14.0 cm by changing the alpha source position. Fig. 6 shows the distribution of R for each measurement. With 6.0 cm drift length, R was around 0.83 and with 14.0cm drift R was around 0.74. These results indicate the diffusion constant is about 400 $\mu m/\sqrt{cm}$. The diffusion constant calculated by Garfield is 380 $\mu m/\sqrt{cm}$, which is in good agreement with the measurement.

(a)   (b)
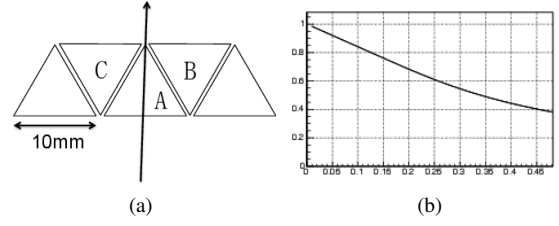
Figure 4: (a) A schematic drawing of the event which is considered in the measurement of diffusion. (b) R, which is defined in the text, vs diffusion. As the diffusion increases, R becomes small.

(a)   (b)
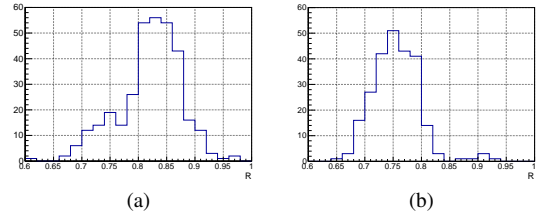
Figure 5: R ratio distribution for drift length of 6.0 cm (a), and 14.0 cm(b). With longer drift length, R becomes smaller and large diffusion is observed.

3. Summary and Future prospect

We measured drift velocity, diffusion and attachment of electrons in a low pressure hydrogen with an electric field of 1 kV/cm/atm. The measurement of drift velocity except for one point and diffusion was well reproduced by the Garfield calculation although attachment was not reproduced.

Since the cause of the discharge is now fixed, we will measure the drift velocity at the last point of voltage again. Furthermore, the next step would be measurement with deuterium gas instead of hydrogen gas.

References

[1] S. Ota *et al*., CNS-REP 2013.
[2] R. Vein's, Garfield, a Gaseous-Detector Simulation Program, http://consult.cern.ch/writeup/garfield/

OEDO project

Susumu Shimoura, Shin'ichiro Michimasa, Masafumi Matsushita, Shinsuke Ota,
Kentaro Yako, Hidetoshi Yamaguchi, Eiji Ideguchi[a], and Kazunari Yamada[b]

Center for Nuclear Study, Graduate School of Science, University of Tokyo
[a]*Research Center for Nuclear Physics, Osaka University*
[b]*RIKEN Nishina Center*

In order to extend scientific opportunities in nuclear physics experiments at the RIBF, we propose a new energy-degrading scheme of RI beams produced by fragmentation or in-flight fission of intermediate-energy heavy-ion beams. The RIBF provides numerous kinds of exotic isotope beams with $A > 100$ typically above 200 A MeV via the Bi-gRIPS separator [1, 2]. This energy region is unique and suitable for studies by using impulse interaction such as inelastic, charge exchange, and knockout reactions, which mainly provide information on ground states, low-excited states and impulse response of exotic nuclei. On the other hand, low-energy nuclear reactions with energies comparable with or below the Fermi momentum in nuclei have additional kinds of aspects on the studies of nuclear structure and nuclear dynamics, since nucleon, cluster and angular momenta as well as energies can be transferred to nuclear systems.
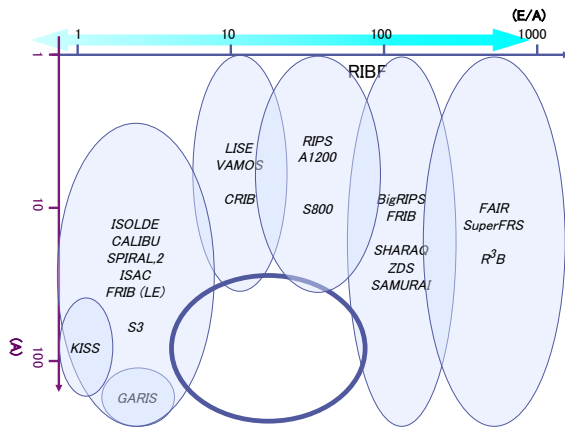
Figure 1: Territory of major RI-beam Facilities on the map of the incident-energy versus mass.

Figure 1 shows a map of several RI beam facilities (separators and spectrometers; operating and future) on the incident energy versus mass number plane. We can find untouched region of 5 to 100 A MeV for $A > 50$. In this region, the following physics programs for heavy exotic nuclei can be expected:

- Nucleon transfer reactions (10 – 50 A MeV)
  Evolution of shell structure seen in unoccupied orbitals are studied by single-particle states populated by (d,p) and (d,n) reactions below 20 A MeV. Cross sections of nucleon transfer also provide information on neutron/proton capture cross section via the asymptotic normalization constants (ANC).
  For orbitals with higher angular momenta are studies by (α,t), (α,^{3}He) reactions at 30–50 A MeV.

- Pair transfer / Cluster transfer (10 – 20 A MeV)
  Di-neutron pickup reactions such as (p,t) provide us

information on di-neutron correlation in nuclei especially for very neutron-rich region where BCS-BEC cross-over is predicted.
Cluster transfer reactions, such as (^{6}Li,d), (^{7}Li,p) and so on, are expected to populate excited cluster states in neutron-rich nuclei, where new degrees-of-freedom from weakly bound neutrons may affect clustering such as glue-effects, interplay between molecular and atomic orbitals, deformation in mean fields, and so on.

- Deep inelastic collisions (incomplete fusion) (5 – 30 A MeV) / Fusion reaction (~ 5 A MeV)
  Dynamics of dissipating reactions of exotic nuclei is interested as leading candidates of synthesizing methods for heavy-mass nuclei, various kinds of deformed/high-spin states, and so on. Use of unstable nuclei provides opportunities to control reaction Q-values, excitation energies of compound system, maximum angular momenta by changing combination of reactions.

- Coulomb excitation reactions for low-energy γ-rays (~ 50 A MeV)
  In-beam spectroscopy using inelastic scattering at high incident energies above 100 A MeV suffers from huge backgrounds of low-energy photons from atomic processes, which limits the gamma-ray energies above several hundreds of keV. Beams at 50A MeV or less enable us to measure Coulomb excitation for highly deformed neutron-rich nuclei.

In order to approach this vacant region, energy degrading methods are proposed at the RIBF facility [3]. However, there are inevitable difficulties in degrading procedure, which causes large image sizes and energy spreads due to increase of phase spaces, charge-state distribution, and contaminants in the beam. For example, in ref. [3], the beam size is estimated to be a 10-cm for mass-100 nuclei with a few A MeV, where higher-order aberrations are neglected.

As a simple example, we examine optics with mono-energetic degrader. Figure 2 schematically shows the optics as well as the phase space in x vs δp. A wedge-shaped degrader at dispersive focus acts as both degrading energy and compressing energy spread. However, after the degrader the beam size (x) becomes large and cannot be focus by static optical devices. The reducing factor of the energy spread is the same as enlargement factor of the beam size (x) at achromatic focus.

The difficulty can be solved by introducing another degree-of-freedom, t, which is conjugate to δ. Fortunately, the primary beam at RIBF is produced by the cyclotron having RF structure. All the produced RI has the same RF structure at the production target. Because of velocity spread, the arrival time (t) of a beam particle at a dispersive focus depends on its horizontal position (x): higher (lower)
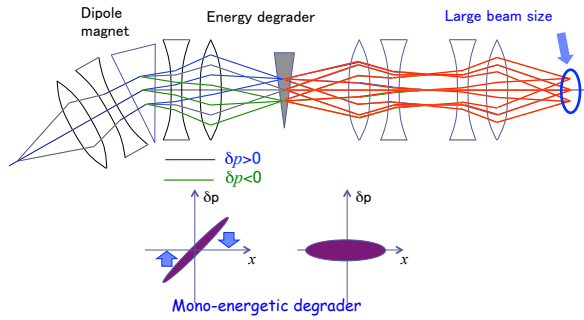
Figure 2: Schematic optics of beam line with mono-energetic degrader.

momentum corresponds to earlier (later) timing. As shown in Fig. 3, an RF deflector placed in the point-to-parallel position kicks beam particles back by means of timing so as to focus the beam.
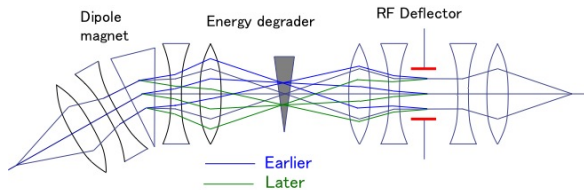
Figure 3: Beam optics with mono-energetic degrader and RF deflector.

The basic specification of the RF deflector is determined based on the experience in the presently used RF deflector at the RIPS facility in RIKEN [4], which is a vertically kick system for purification of RI beams. It is noted that the proposed RF deflector is operated after energy degrading to about 50 A MeV, which is almost same as the RIPS facility. Present design of the new RF deflector is about twice in size in order to increase acceptances and quality (Table 1).

Frequency	17.6 ± 1.5 MHz
Maximum voltage	300 kV
Gap between electrodes	200 mm
Length of electrodes	1000 mm
Width of electrodes	400 mm
Vacuum	5×10^{-6} Pa

Table 1: Specification of RF deflector.

Among possible sites for the OEDO system in the RIBF, we decided to construct it in the SHARAQ beam line [5] under the following consideration:

- There should be a suitable dispersive focal plane before an enough length of straight line, which is satisfied by the FH8 focus in the SHARAQ beam line satisfies.

- The height of the roof should be enough for the size of the RF cavity (about 4m).

- Some possible physics programs require a spectrometer for charged particles. The first part (QQD) of

the SHARAQ can be used for a broad-range magnetic spectrometer. It is noted that the SHARAQ is rotatable to 15°.

Figure 4 shows our conceptual design of the beam line. Two STQ's and RF deflector are placed in the E20 experimental room.
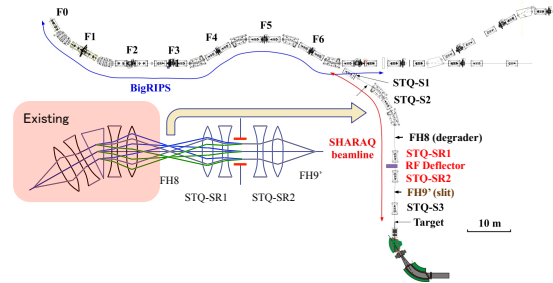
Figure 4: Design of Beamline.

Based on the above scheme and design, we call the new project as OEDO (**O**ptimized **E**nergy **D**egrading **O**ptics for RI beam:　　　, which is the old name of the Tokyo metropolitan area). Detailed optical simulation including aberrations, charge states, energy straggling is started for actual design of the beam line.

References

[1] T. Kubo, *Nucl. Instrum. Meth. in Phys. Res.* **B204**, 97 (2003)

[2] T. Kubo, et al., *Prog. Theor. Exp. Phys.* **2012** (2012) 03C003

[3] E. Ideguchi, *Prog. Theor. Exp. Phys.* **2012** (2012) 03C005

[4] K. Yamada, T. Motobayashi, and I. Tanihata, *Nucl. Phys. A* **746** (2004) 156c

[5] T. Uesaka, et al., *Prog. Theor. Exp. Phys.* **2012** (2012) 03C007

Production of beams from solid materials with Hyper ECR ion source

Y. Ohshiro, S. Yamaka, S. Watanabe, H. Muto[a], H. Yamaguchi, and S. Shimoura

Center for Nuclear Study, Graduate School of Science, University of Tokyo
[a]Center of General Education, Tokyo University of Science, Suwa

1. Introduction

The AVF cyclotron in RIKEN has been providing gaseous and solid ion beams for the users, such as the CRIB group [1]. In the year 2013, we produced solid ion beams such as $^7Li^{2+}$, $^7Li^{3+}$, $^{11}B^{4+}$, $^{40}Ca^{12+}$ and $^{56}Fe^{15+}$ by using the Hyper ECR ion source and injected those beams to the AVF cyclotron.

The beam intensities from the non-gaseous material increased to be twice by improving the evaporation system of the ion source. For the refractory elements, a rod of the solid material (SMR) such as CaO or FeO was installed near the wall of the plasma chamber, while for the non-refractory elements a micro oven (MO) filled with ^6Li or ^7Li was used. By using either method, we obtained beam currents of 280, 75, 28, and 7 eμA for $^7Li^{2+}$, $^7Li^{3+}$, $^{40}Ca^{12+}$, and $^{56}Fe^{15+}$, respectively. We describe the two methods in this report.

2. Evaporation system of Hyper ECR Ion Source

The SMR or MO was inserted near the ECR zone to evaporate the material elements. Figure 1 shows a cross-sectional view of the Hyper ECR ion source with the SMR. In the case of Fe beams, a rod of FeO with a geometry of $60 \times 4 \times 4$ mm^3 was inserted into the plasma chamber through a window of the RF wall. The tip of the rod was bombarded by the electrons from the ECR plasma for heating the rod.

Star-shaped scorches were observed at the both edge walls of the ion source. Figure 2 (a) shows the scorch patterns by electrons stopped at the RF wall. When SMR was inserted through the scorch region, the beam intensity was turned to be fluctuated [2]. Furthermore, the beam intensity reduced when the SMR was placed closer to the ECR zone. To avoid the problems, SMR was inserted through the 210° window F at a radius 17.5 mm from the center of the RF wall outside the star-like scorch.

Figure 3 (a) shows a front view of the new MO with 5 holes with 2-mm diameters for extraction of the material. Another hall of 4 mm diameter was made to supply the material sample. The hall was closed after the supplement. Figure 3 (b) shows a heat shield surrounding the vessel to keep a constant temperature gradient. With the previous MO method [3], it was difficult to sustain a high voltage because too much current was generated. Consequently, the high-voltage power supply sometimes tripped when the RF power of 480 W was fed into the ECR ion source.
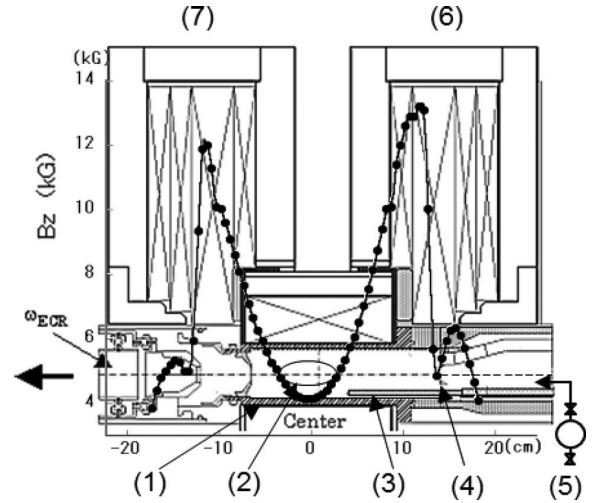
Fig. 1: Cross-sectional view of Hyper ECR Ion Source. (1): Plasma chamber, (2): ECR zone, (3): Solid material rod, (4): RF wall, (5): Vacuum Vessel, (6): Mirror Coil 1 (MC1), and (7): Mirror Coil 2 (MC2).
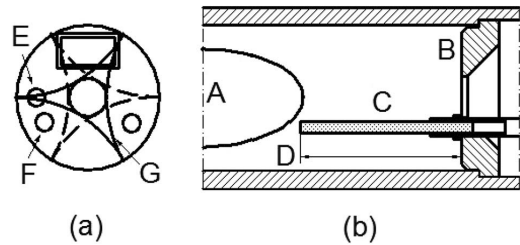
Fig 2: (a) and (b) Schematic view of the new SMR method. A: ECR zone, B: RF wall, C: SMR, D: distance between the RF wall and tip of SMR, E and F: windows inserting rod, and G: Area of star-shaped plasma scorch (solid line: gas inlet side and dashed line: beam extraction side).
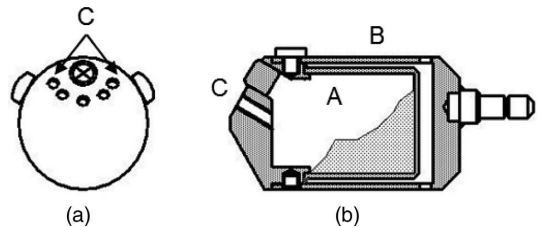
Fig. 3: Cross-sectional view of new MO. A: vessel filling solid material, B: heat shield and C: holes.
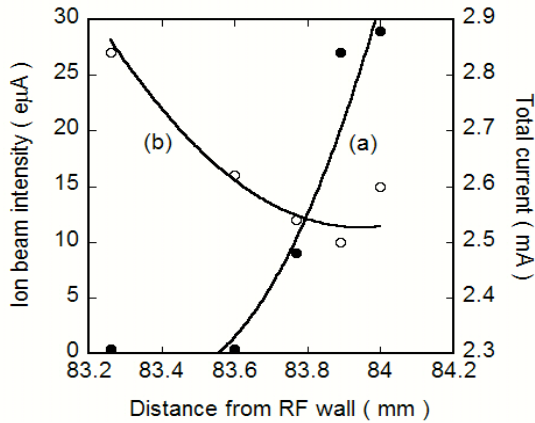
Fig. 4: Ion beam intensity of $^{40}Ca^{12+}$ as a function of the distance of CaO rod inserting from opening F. (a) ion beam intensity and (b) total current of extraction electrode. The solid lines are eye-guides.

3. Operation of the evaporation system

High intensity beams were provided constantly by using the new SMR method. A $^{40}Ca^{12+}$ ion beam, for example, was generated by inserting the SMR of CaO from the window (F) (see Fig. 2(a)). Figure 4 shows the ion beam intensity of $^{40}Ca^{12+}$ as a function of the distance of CaO rod from the RF wall. Total current from the ion source decreased slowly, while the analyzed ion beam current (a) increased rapidly as the distance increased. The tip of the rod was close to the ECR zone when the distance was 84mm. In this case, an ion beam intensity of 28 eµA was obtained by using the SMR. Now we are using the insertion method from window (F) as a standard method, since the control of the vapor pressure of refractory material is possible.

4. Consumption rate and beam intensities of the non-gaseous ion beams

When the tip of the SMR is close to the ECR zone, a stable and high intensity beam can be obtained. Table 1 shows beam intensities of the typical ion species from the ion source. The new SMR method is being applied to high melting point (m.p.) materials. Typical examples are $^{28}Si^{9+}$, $^{40}Ca^{12+}$, $^{59}Co^{15+}$ ions, produced from materials of SiO_2 CaO, Co, respectively. The melting points and extracted beam intensities of these ions are listed in the table. In these operations, the vacuum pressures and the RF power were adjusted in order to achieve the best currents.

In the case of the new MO method, we optimized number of openings of the crucible to control the evaporation rate of low m.p. materials. Typical examples are $^7Li^{2+}$, $^6Li^{3+}$ and $^{32}S^{9+}$ ion beams, produced by the new MO with the numbers of the open holes 5, 3, and 1, respectively.

Table 1: Beam intensities of the typical ion species.

Ion Species	Beam Intensities (eµA)	Charged Materials	m.p. (°C)
$^7Li^{2+}$	280	^7Li pure metal (Oven)	180
$^6Li^{3+}$	75	^6Li pure metal (Oven)	180
$^{11}B^{4+}$	50	$B_{10}H_{14}$ (MIVOC)	99
$^{24}Mg^{8+}$	45	Mg pure metal (Oven)	650
$^{28}Si^{9+}$	35	SiO_2 (Rod)	1500
$^{31}P^{9+}$	29	P_2O_5 (Oven)	563
$^{32}S^{9+}$	47	S grain (Oven)	119
$^{40}Ca^{12+}$	28	CaO (Rod)	2572
$^{56}Fe^{15+}$	7	FeO (Rod)	1420
$^{59}Co^{15+}$	20	Co pure metal (Rod)	1495

The beam intensities of these ions are listed in Table 1. In the case of the $^7Li^{2+}$ ion, an intense beam of 280 eµA was obtained. The consumption rate of the material was about 13 mg/h and the capacity of the crucible was 10 ml.

By employing the new MO method, we achieved continuous evaporation and even under the high RF power condition we could keep stably high extraction voltage. After the ion source operation, excess material remaining in the plasma chamber was mostly in small granules, and they could be easily removed. The consumption rate of materials by evaporation also reduced to 1/3. This method is good for the low melting point materials.

5. Contribution to the Nuclear Experiments

Development of the evaporation system is contributing significantly to the nuclear physics experiments. For example, the $^{28}Si^{9+}$ ion beam was continuously and stably operated for 17 days. With the new MO method, we also achieved a continuous 12-days operation for the $^6Li^{3+}$ ion beam.

6. Summary

We succeeded in development of the new evaporation systems of solid materials used for the extraction stable and high intensity beams, which is adequate for most of the nuclear physics experiments at CNS and RIKEN.

References

[1] Y. Yanagisawa, S. Kubono, T. Teranishi et al., Nucl. Instrum. Methods Phus. Res. A 539, 74-83 (2005)
[2] Y. Ohshiro, S. Yamaka et al., RIKEN Accel. Prog. Rep. 38, 253 (2005).
[3] Y. Ohshiro, S. Yamaka et al., RIKEN Accel. Prog. Rep. 39, 231 (2006).
[4] W. Yokota, T. Nara, K. Arakawa, M. Ide, and Y. Kaminura, Nucl. Instrum. Methods Phys. Res. B 122, 141 (1997).

Optical emission spectroscopy of the Hyper-ECR ion source

H. Muto[a], Y. Ohshiro[b], S. Yamaka[b], S. Watanabe[b,c], M. Oyaizu[d], H. Yamaguchi[b], K. Kobayashi[c], Y. Kotaka[c], M. Nichimura[c], S. Kubono[c,e], M. Kase[a], T. Hattori[e,f], and S. Shimoura[b]

[a]Center of General Education , Tokyo University of Science, Suwa, [b]Center for Nuclear Study, University of Tokyo, [c]Nishina Center for Accelerator-Based Science, RIKEN [d]Institute of Particle and Nuclear Studies, High Energy Accelerator Research Organization [e]eInstitute of Modern Physics, Chinese Academy of Sciences, Heavy Ion Cancer Therapy Center, National Institute of Radiological Sciences

1. Introduction

Hyper-ECR ion source has been successfully used for RIKEN Azimuthal Varying Field (AVF) cyclotron as an injector and in the process of production of the multi-charged ion beams of high intensity [1]. A grating monochromator was installed at the Hyper-ECR ion source, and optical line intensities of gaseous and metallic ion beams were observed during tuning [2,3]. During beam tuning, the charge distribution of ions extracted from ECR plasma which has selected by a Faraday cup. After a q/m selected, the ion beam intensity was maximized. Since the ECR plasma can ionize any species in the plasma chamber, some background ions which have close q/m are contaminated in the beam. The separation of such contaminants are almost impossible only by using the magnet. Conceptual diagram of this work is shown in Fig. 1. In this study the optical line spectra of multi-charged $^{24}Mg^{8+}$ and $^{7}Li^{3+}$ ions were measured and the relation between light intensity of optical line spectrum and their ion beam intensities was investigated.
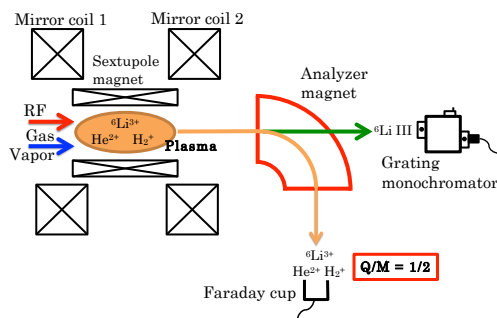
Fig. 1. Beam separation by an optical monochromator. Among the ions produced by the ECR plasma which have q/m=1/2, we observed the light emission from the $^{6}Li^{3+}$ ions.

2. Experimental set up

The straight course of the beam analyzer magnet of the hyper- ECR ion source is equipped with a fused quartz window. A grating monochromator (JASCO CT-25C) was located outside of the window and connected to a photomultiplier (Photosensor module H11462-031, Hamamatsu Photonics) [2,3]. The distance from the ECR plasma to the entrance slit of the monochromator is 1.5 m. The spectral bandwidth determined by the grating is 0.1 nm (FWHM). Gratings of 1200 lines/mm was used. L-37 and R-64 filters are used for preventing both second and third order light signals. The grating dial is remotely controlled. The light intensity spectra were recorded by a X-Y pen recorder.

3. Results and discussions

Figures 2 (a) and (b) show the optical line spectra of the Hyper-ECR plasma under the plasma chamber baking and during operation of $^{24}Mg^{8+}$ ion beam respectively. High intensity $^{24}Mg^{8+}$ ions were produced by the Hyper-ECR ion source using a metal rod method [1]. MgO rod was installed through the RF wall. The rod was heated by the ECR plasma. Before an ordinary beam tuning, a degassing of the plasma chamber must be conducted for one or two days.
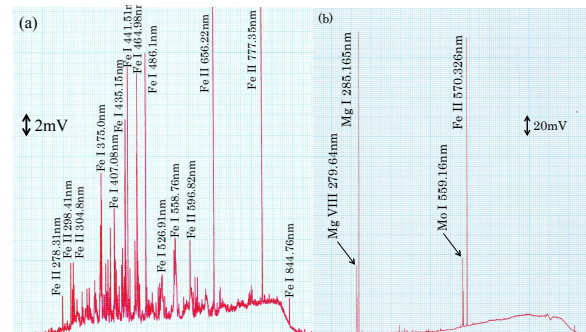
Fig. 2. (a) Optical line spectrum during chamber baking; (b) Optical line spectrum during $^{24}Mg^{8+}$ beam tuning.

During this process, a high RF power (~500W) has been sustained without a metal rod until obtaining a required vacuum condition. The light

intensities of Fe I and II lines were observed in the plasma during baking the chamber as shown in fig. 2 (a), because the previous beam time was $^{56}Fe^{15+}$ beam, and FeO rod method had been used for one week before the baking so that some of Fe atoms were attached to the plasma chamber. Plasma chamber is made of stainless steel. After baking the chamber, tuning of a $^{24}Mg^{8+}$ beam was started. The light luminescence of Mg VIII was clearly observed as shown in Fig. 2 (b). Almost all Fe lines disappeared after baking. Usually, Fe and O optical lines are disturbing observation of the desired lines. Those contaminated lines are of a substantial number, and a major issue. In this operation we succeeded in reducing Fe line intensities drastically. However, it is not clear, whether Magnesium has a pomp effect like Titanium, or not. Mo I line was also observed in the spectrum. Molybdenum cover is usually used for a smooth heat transfer to the tip of the metal rod from the plasma [3]. Wavelengths of the lines were assigned in accordance with the NIST Atomic Spectra Database [4].

Figure 3 shows an optical line spectrum of the Hyper-ECR plasma under operation for $^{7}Li^{3+}$ ion beam. Light luminescence of ^{7}Li III line was observed at $\lambda = 449.83$ nm. Figure 4 shows time charts of $^{7}Li^{3+}$ beam current and ^{7}Li III light intensity during beam tuning recorded by a pen recorder. The result clearly shows a linear correlation of these two values. Therefore, the light luminescence signal from the photomultiplier is obviously an essential information for tuning the only the beam interested.
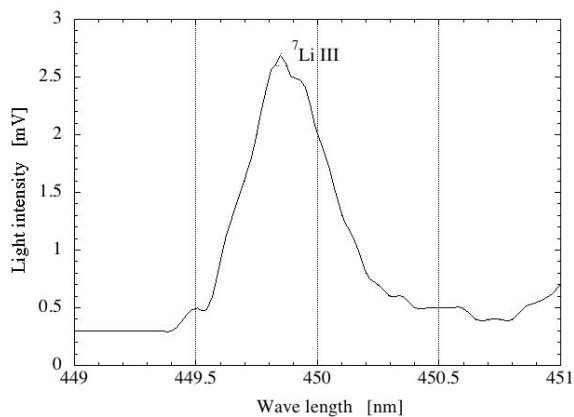
Fig 3. Optical line spectrum of ^{7}Li III observed at $\lambda = 449.83$ nm.

4. Conclusions

Optical emission spectroscopy of the ECR plasma has been proved to be a useful technique for tuning the ion source. By this method, the observation of the desired ion species in the plasma has been simplified, and tuning of the ion source without interrupting beam time by an observation of the light intensity voltage of photomultiplier was successfully demonstrated. In this experiment we conducted the $^{7}Li^{3+}$ beam tuning. The $^{6}Li^{3+}$ beam is thought to be a considerably more difficult to separate from He^{2+} and H_2^{+} etc. He gas is usually used as a supporting gas for keeping a necessary plasma condition. Therefore, a further development of our plasma observation technique must be needed.
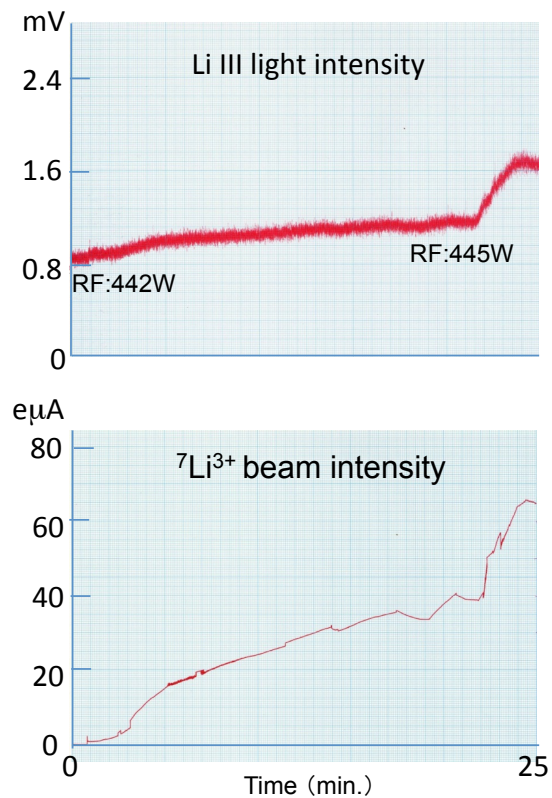
Fig. 4. Time charts of $^{7}Li^{3+}$ beam intensity (down panel) and ^{7}Li III light luminescence (upper panel) during beam tuning. In this figure both beam intensity and light intensity were increasing because of raising RF power from 442 to 445 W.

References

[1] Y. Ohshiro and H. Muto et. al., Rev. Sci. Instrum. **85**, 02A912 (2014).
[2] H. Muto and Y. Ohshiro et. al., Rev. Sci. Instrum. **84**, 073304 (2013).
[3] H. Muto and Y. Ohshiro et. al., Rev. Sci. Instrum. **85**, 02A905 (2014).
[4] See www.nist.gov/pml/data/asd.cfm for NIST Atomic Spectra Database.

Theoretical Nuclear Physics

Large-scale shell model calculation project for double-beta decay

Y. Iwata[a], N. Shimizu[a], Y. Utsuno[b], M. Honma[c], T. Abe[d], and T. Otsuka[a,d,e]

[a]*Center for Nuclear Study,School of Science, The University of Tokyo, 113-0033 Tokyo, Japan*
[b]*Japan Atomic Energy Agency, 319-1184 Tokai, Japan*
[c]*Center for Mathematical Sciences, University of Aizu, 965-8580 Fukushima, Japan*
[d]*Department of Physics, The University of Tokyo, 113-0033 Tokyo, Japan*
[e]*National Superconducting Cyclotron Laboratory, Michigan State University, East Lansing, MI 48824, USA*

Neutrino is a mysterious particle, which is a candidate for the Majorana particle. The identification of neutrino as the Majorana particle is expected to bring about a high impact on physics that even requires the modification of the standard model of electro-weak interaction. At present such an identification can be verified only by observing neutrino-less double-beta decay processes, where two types of double-beta decay exist depending on whether neutrino is emitted or not: zero-neutrino double-beta decay and two-neutrino double-beta decay. There are more than 50 candidates known as the double-beta decay nuclei, among which the two-neutrino double-beta decay has been observed for ^{48}Ca, ^{76}Ge, ^{82}Se, ^{96}Zr, ^{100}Mo, ^{116}Cd, ^{128}Te, ^{130}Te, ^{150}Nd, and ^{238}U [1]. Zero-neutrino double-beta decay and two-neutrino double-beta decay are the processes:

$$^{A}X \rightarrow {}^{A}Y + 2e^{-},$$

$$^{A}X \rightarrow {}^{A}Y + 2e^{-} + 2\bar{\nu},$$

where X and Y mean the proton numbers satisfying Y-X=2, and A denotes the mass number. Zero-neutrino double-beta decay does take place only if the neutrino is the Majorana particle, while two-neutrino double-beta decay takes place if the neutrino is either the Majorana particle or the Dirac particle. The lepton number conservation is violated in the former case, but not in the latter case.

Two-neutrino double-beta decay has already been observed, and the corresponding half-life is measured. The half-lives of the double-beta decay are represented by

$$[T_{1/2}^{0\nu}]^{-1} = G^{0\nu}|M^{0\nu}|^2 \, m_{\beta\beta}^2, \tag{1}$$

$$[T_{1/2}^{2\nu}]^{-1} = G^{2\nu}|M^{2\nu}|^2, \tag{2}$$

where $T_{1/2}^{n}$, G^{n}, and M^{n} are the half life, the phase space factor and the nuclear matrix element, respectively; the index n $= 0\nu$ corresponds to the zero-neutrino double-beta decay, and n $= 2\nu$ to the two-neutrino double-beta decay. Here $m_{\beta\beta}$ denotes the effective mass of neutrino, so that zero-neutrino double-beta decay takes place only if $m_{\beta\beta}$ is not equal to zero. It is worth mentioning that the neutrino oscillation has been observed, which is a strong suggestion for neutrino to have nonzero mass. There are many experimental efforts to observe zero-neutrino double-beta decay all over the world: e.g., AMoRe, CANDLES, COBRA, CUORE, DCBA/MTD, EXO, GAGG, GERDA, KamLAND-Zen, LUCIFER, Majorana, MOON, NEXT, SNO+, SuperNEMO, Xe ELCC, XMASS, and Zr-loaded LS. In these experiments the half-life of zero-neutrino double-beta decay is expected to be measured. If it is measured, the effective mass of neutrino is determined by means of Eq. (1).

$$m_{\beta\beta}^{-2} = G^{0\nu}|M^{0\nu}|^2 \, T_{1/2}^{0\nu}.$$

Table 1: Concerning the double-beta decay of ^{48}Ca, m-scheme diagonalization dimension is shown for two different conditions. The model space and the truncation adopted in shell calculations are presented in the first column. The dimension in case of "$sdpf$, $0\hbar\omega$" is exactly the same as that in case of "pf, no truncation".

	^{48}Ca (0^+)	^{48}Ti (0^+)	^{48}Sc (1^+)
$sdpf, 0\hbar\omega$	12,022	634,744	135,741
$sdpf, 2\hbar\omega$	$10^{8.21}$	$10^{9.30}$	$10^{8.85}$

Since the neutrino mass is quite light, the precise calculation of $M^{0\nu}$ is indispensable. Indeed, the twice of $M^{0\nu}$ value results in the half value of the mass, while the twice of $G^{0\nu}$ value or $T_{1/2}^{0\nu}$ value results in $1/\sqrt{2}$ times smaller value of the mass. The precise calculation of $M^{0\nu}$ is the primal aim of our project.

The large-scale shell model calculations are carried out, where the shell model code KSHELL [2] is used. KSHELL, which is designed for the hybrid parallelization (MPI and OpenMP parallelization) available in the latest supercomputers, realizes the diagonalization of matrix based on the Lanczos method. The ultimate goal of our research project is, for the candidate nuclei, to present the matrix element of zero-neutrino double-beta decay with the highest accuracy so far, and to predict both possible half-life of neutrino-less double-beta decay and possible effective mass of neutrino. This project is executed as one of the HPCI Strategic Program for Innovative Research (SPIRE) Field 5 "The origin of matter and the universe" [3]. Among HPCI facilities in Japan, FX10 supercomputer system at the Information Technology Center, The University of Tokyo has been exploited as far as the research for the double-beta decay is concerned. The FX10 supercomputer system consists of Oakleaf-FX and Oakbridge-FX, where the total theoretical performance of Oakleaf-FX and Oakbridge-FX are 1.1300 PFLOPS and 0.1362 PFLOPS, respectively. This system enables us to take the model space as large as the two-major shell, in which the excitation across the two different major shells can be taken into account.

In terms of increasing the precision of the calculations, it is preferable to choose one of the candidate nuclei, whose two-neutrino double-beta decay half life and the corresponding Gamow-Teller transition strength are known. In particular, the results form Gamow-Teller transition experiments provide rather detail constraint on the structure of initial and final states of double beta decay. Accordingly we have decided to begin with studying the double-beta decay of ^{48}Ca, where ^{48}Ca is the lightest double-beta decay candidate. Particularly we performed two-major shell calculations (considering sd and pf shells) of ^{48}Ca. Since the
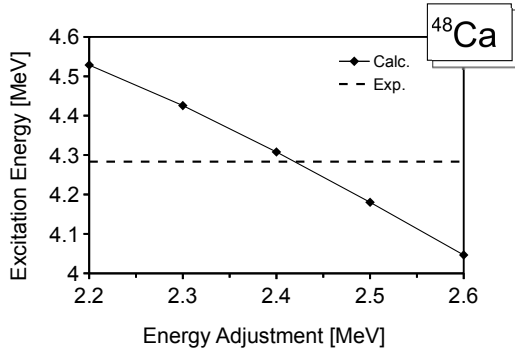
Figure 1: Adjustment of the gap between sd-shell and pf-shell. The vertical axis (corresponding to the criterion) shows the excitation energy of second 0^+ state of ^{48}Ca. The experimental value is taken from Ref. [7].
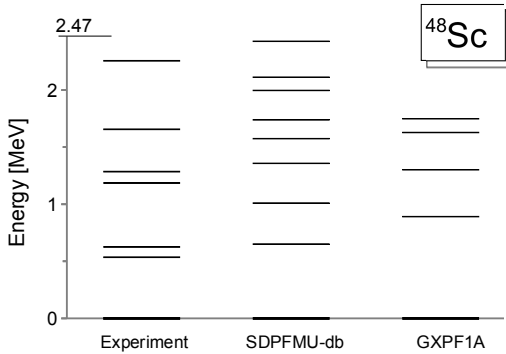
Figure 2: Energy levels of 1^+ states of ^{48}Sc. The energy along the vertical axis is that measured from the first 1^+ state of ^{48}Sc. Experimental values are taken from Ref. [8], in which the Gamow-Teller transition up to 5.0 MeV from the ground state (corresponding to 2.47 MeV from the first 1^+ state of ^{48}Sc in experiment) has been observed. The former one-major shell calculation employing GXPF1A [9] is shown for comparison.

size of two-major shell calculations is quite large, it is necessary to introduce suitable truncation. Here we truncate the possible excitations up to $2\hbar\omega$. The dimension of the matrix in the calculations are shown in Table I, where in fact more than 10^{10} dimension is necessary to perform non-truncated calculation in $sdpf$-shell.

In terms of studying zero-neutrino double-beta decay of ^{48}Ca, a procedure consisting of two steps is scheduled. In the first step, utilizing existing two kinds of experimental data as reference, we find/obtain nuclear interaction with the precise description of two-neutrino double-beta decay, and we obtain precise initial, final and virtual intermediate states. In the second step, utilizing those obtained in the first step, we calculate the matrix element of zero-neutrino process. That is, the two-neutrino double-beta decay is mainly considered in the first step, and the zero neutrino double-beta decay is considered in the second step.

SDPF-MU interaction [4] is employed in our launch calculation to investigate

$$^{48}\text{Ca} \rightarrow ^{48}\text{Ti} + 2e^- + 2\bar{\nu}.$$
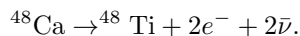
The obtained result does not provide so precise description as reproducing the high energy part of the Gamow-Teller

transition strength (for the detail, see Figures of Ref. [5]). In Ref. [5] one crucial factor for such a discrepancy has been pointed out to be a small number of proton excitation in the second 0^+ state of ^{48}Ca (see Table I of Ref. [5]). Indeed, 0^+ state of ^{48}Ca is experimentally suggested to be a proton excitation state [6]. It is expected that the gap between sd and pf shells are so large that the proton excitation from sd to pf shells is hindered. We adjust the gap by reducing the single particle energies of the pf-shell orbits (for both protons and neutrons). The gap-adjustment incremented by 0.10 MeV (Fig. 1) for fitting the excitation energy of second 0^+ state of ^{48}Ca shows that the suitable reduction of the gap is 2.40 MeV. The energy levels obtained after the adjustment is compared to the experiment in Fig. 2. Several levels are obtained around the observed state at 2.26 MeV by the SDPFMU-db interaction (adjusted one), while the corresponding level is missing in case of GXPF1A interaction.

The adjustment brings about more proton excitation across the major shells. For the second 0^+ state of ^{48}Ca the excited proton number across the shell is up to 1.64 (for non-adjusted case, see typically 0.10 to 0.25 as in Table I of [5]). As a result, the proton and neutron excitations across the major shells are mixed into the initial and final states; the corresponding proton and neutron numbers are 0.27 and 0.17 for the ground state of ^{48}Ca, and 0.37 and 0.29 for the ground state of ^{48}Ti, respectively.

References

[1] List of Adopted Double Beta Decay Values, NNDC database; http://www.nndc.bnl.gov/bbdecay/list.html.
[2] N. Shimizu, arXiv:1310.5431 (2013).
[3] HPCI SPIRE field 5; http://www.jicfus.jp/field5/
[4] Y. Utsuno et al., Phys. Rev. C 86 051301(R) (2012).
[5] Y. Iwata et al., arXiv:1409.4003.
[6] F. Videbaek et al., Nucl. Phys. A 451 131 (1986).
[7] NuDat 2.6; http://www.nndc.bnl.gov/nudat2/
[8] E.-W. Grewe et al., Phys. Rev. C 76, 054307 (2007).
[9] M. Horoi et al., Phys. Rev. C 75, 034303 (2007).

Nature of isomerism in exotic sulfur isotopes

Y. Utsuno[a,b], N. Shimizu[b], T. Otsuka[c,b,d], T. Yoshida[b], and Y. Tsunoda[c]

[a]*Advanced Science Research Center, Japan Atomic Energy Agency*
[b]*Center for Nuclear Study, Graduate School of Science, University of Tokyo*
[c]*Department of Physics, University of Tokyo*
[d]*Department of Physics and Astronomy and National Superconducting Cyclotron Laboratory, Michigan State University*

The structure of exotic nuclei around $N = 28$ has recently received much attention from the viewpoint of shell evolution because the $N = 28$ magic number disappears in ^{42}Si [1]. The $N = 28$ isotone ^{44}S has also very interesting properties. The $B(E2; 2_1^+ \rightarrow 0_1^+)$ value indicates moderate deformation in spite of the $N = 28$ singly magic nucleus, and the very low-lying 0_2^+ state suggests shape coexistence. Most surprisingly, the $E2$ transition from 4_1^+ to 2_1^+ is strongly hindered: $B(E2; 4_1^+ \rightarrow 2_1^+) < 1$ W.u. [2]. A similar strong hindrance in the $E2$ transition is also observed for the $E2$ decay from $7/2_1^+$ to $3/2_1^+$ in ^{43}S [3]. While the shell-model calculation well reproduces those exotic isomeric states [2], the origin of the isomerism is quite ambiguous. This is partly because the shell-model calculation does not directly give intrinsic properties. The present study aims at clarifying the nature of isomerism in sulfur isotopes by performing state-of-the-art beyond-mean-field analyses in the shell model [4].

The shell-model calculations are carried out in the $\pi(sd)$-$\nu(pf)$ shell using the SDPF-MU interaction [5]. As presented in Ref. [5], those shell-model calculations well reproduce the structure of exotic nuclei in the $N \sim 28$ region including the disappearance of the $N = 28$ magic number in ^{42}Si. In order to deduce the intrinsic properties of shell-model wave functions, we conduct the variation after angular-momentum projection (AM-VAP) calculation in the shell-model space. The wave function adopted in the AM-VAP is

$$|IM\sigma\rangle_{\mathrm{AM-VAP}} = \sum_K g_K^{IM\sigma} \hat{P}_{MK}^I |\Phi(IM\sigma)\rangle, \quad (1)$$

where $\hat{P}_{MK}^I$ denotes the usual angular-momentum projection operator with I, M and K denoting the total angular momentum and its z components along the laboratory and intrinsic frames, respectively, and each state with a given (I, M) is labeled with σ. $|\Phi(IM\sigma)\rangle$ is a Slater determinant, and is thus regarded as the intrinsic state of $|IM\sigma\rangle_{\mathrm{AM-VAP}}$. The form of $|\Phi(IM\sigma)\rangle$ and the coefficient $g_K^{IM\sigma}$, which characterizes the mixing between different K values, are determined to minimize the energy $E(I\sigma) = \langle IM\sigma|H|IM\sigma\rangle_{\mathrm{AM-VAP}}/\langle IM\sigma|IM\sigma\rangle_{\mathrm{AM-VAP}}$.

In Fig. 1, the energy levels calculated with the AM-VAP are compared with experimental data and those of the full shell-model calculation. The AM-VAP calculation successfully reproduces the anomalously hindered $B(E2; 4_1^+ \rightarrow 2_1^+)$ value as well as the full shell-model calculation. The similarity between the full shell-model AM-VAP results is confirmed from the overlap probabilities between the wave functions obtained by those two calculations. For the states shown in Fig. 1, those overlap probabilities are greater than 0.8. Thus, it is quite reasonable to discuss many-body properties in ^{44,43}S on the basis of the AM-VAP states.
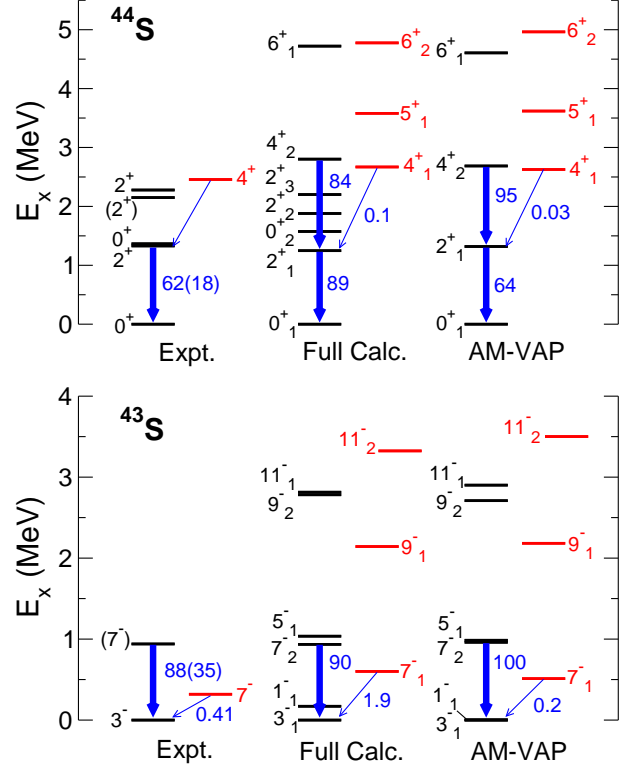
Figure 1: Energy levels and $B(E2)$ values (in e^2fm^4) in ^{44,43}S compared among experiments (Expt.), the full shell-model calculation (Full Calc.), and the AM-VAP approximation to the shell model (AM-VAP). The spin-parity is denoted as J^π for ^{44}S and $2J^\pi$ for ^{43}S.

The intrinsic properties of each state are obtained directly from the Slater determinant $|\Phi(IM\sigma)\rangle$. The intrinsic quadrupole moments Q_0 and Q_2 are defined as its expectation values of the mass quadrupole operators $r^2 Y_{20}$ and $r^2 Y_{22}$, respectively, where the intrinsic axes are determined to diagonalize the quadrupole tensor and to satisfy the order $\langle Q_{zz} \rangle \geq \langle Q_{xx} \rangle \geq \langle Q_{yy} \rangle$. Using Q_0 and Q_2, the deformation parameters β and γ are extracted in the usual way [6]. Since the intrinsic axes are thus determined, the K quantum number is well defined apart from its sign. The distribution of K, which is normalized to unity, is calculated by following the method described in Ref. [6].

The intrinsic properties of ^{44}S, including the distribution of K and deformation parameters β and γ, are listed in Table 1. The 0_1^+, 2_1^+, 4_2^+ and 6_1^+ states are dominated by the $K = 0$ configurations as expected for the ground-state band, while the $K = 1$ component enlarges with increasing spin due to the Coriolis coupling. On the other hand, the 4_1^+, 5_1^+ and 6_2^+ states are dominated by the $K = 4$ configurations. Although the possibility of the dominance of $K = 4$ in the 4_1^+ level was mentioned in Ref. [2], this suggestion

I_σ^π				$\|K\|$				β	γ
	0	1	2	3	4	5	6		
0_1^+	1.00							0.24	33
2_1^+	0.98	0.00	0.01					0.26	23
4_2^+	0.92	0.08	0.00	0.00	0.00			0.28	14
6_1^+	0.76	0.23	0.01	0.00	0.00	0.00	0.00	0.28	13
4_1^+	0.00	0.00	0.00	0.07	0.93			0.23	28
5_1^+	0.00	0.00	0.01	0.08	0.85	0.07		0.23	24
6_2^+	0.00	0.01	0.01	0.14	0.80	0.04	0.00	0.23	26

Table 1: Distribution of $|K|$ and deformation parameters (β, γ) (γ: in deg.) in the AM-VAP states for ^{44}S.

I_σ^π			$\|K\|$				β	γ
	1/2	3/2	5/2	7/2	9/2	11/2		
$1/2_1^-$	1.00						0.27	15
$3/2_1^-$	0.98	0.02					0.25	17
$5/2_1^-$	0.97	0.03	0.00				0.27	16
$7/2_2^-$	0.96	0.04	0.00	0.00			0.25	16
$9/2_2^-$	0.96	0.04	0.00	0.00	0.00		0.28	15
$11/2_1^-$	0.91	0.09	0.00	0.00	0.00	0.00	0.25	16
$7/2_1^-$	0.00	0.01	0.01	0.98			0.22	31
$9/2_1^-$	0.00	0.01	0.04	0.95	0.01		0.23	31
$11/2_2^-$	0.00	0.01	0.01	0.08	0.03	0.87	0.25	37

Table 2: Same as Table 1 but for ^{43}S.

was rather hypothetical based on a naive analogy to heavy nuclei. The succeeding microscopic calculations [7, 8] do not support the $K = 4$ hypothesis of Ref. [2]. Hence, the present calculation is the first to unambiguously show the dominance of $K = 4$ in the 4_1^+ level of ^{44}S. The K forbideness $\Delta K - \nu = 2$, where ν is the multipolarity of γ ray, accounts for the strong hindrance of the $E2$ decay from 4_1^+.

The 4_1^+ state in ^{44}S is classified as one of the high-K isomers which are observed in heavier-mass regions. It is widely accepted that high-K isomers occurs only in nuclei having stable axially-symmetric deformation in order that the K quantum number is conserved. In the case of ^{44}S, the 4_1^+ state has an approximately good quantum number in spite of significant triaxiality as presented in Table 1. The present analysis shows that although strong K mixing occurs in the intrinsic state $|\Phi(4_1^+)\rangle$, the resulting AM-VAP state $|4_1^+\rangle_{\text{AM-VAP}}$ in Eq. (1) has an approximately good K number after diagonalizing the Hamiltonian in the K space. Thus, this is a new kind of high-K isomer.

What is still unclear is why the $K = 4$ state lies below the normal $K = 0$ state in ^{44}S. The structure of ^{43}S provides crucial information on this question. As presented in Fig. 1, the $7/2_1^-$ state is located very close to the ground state and its $E2$ strength between them are quite small [3]. A similar AM-VAP analysis is done for ^{43}S and the resulting intrinsic properties are displayed in Table 2. This $E2$ hindrance is also due to the K forbideness: the $3/2_1^-$ and $7/2_1^-$ states are dominated by $K = 1/2$ and $K = 7/2$, respectively. The $K = 1/2$ and $K = 7/2$ states are regarded as the $\Omega = 1/2$ and $\Omega = 7/2$ one-quasiparticle states on top of the ^{42}S core, respectively, where Ω stands for the z component (in the intrinsic frame) of the angular momentum for a quasiparticle state. Since those quasiparticle levels lie very close from experimental $3/2_1^-$ and $7/2_1^-$ levels in ^{43}S, two-quasiparticle states occupying $\Omega = 1/2$ and/or $\Omega = 7/2$ become low-lying states. The possible two-quasiparticle states in ^{44}S are two $K = 0$ states (($\nu\Omega = 1/2)^2$ and $(\nu\Omega = 7/2)^2$), a $K = 4$ state ($\nu\Omega = 1/2 \otimes \nu\Omega = 7/2$), and a $K = 3$ state ($\nu\Omega = 1/2 \otimes \nu\Omega = 7/2$). The $K = 4$ state is higher than the $K = 0$ states in terms of the intrinsic energy even though the $\Omega = 1/2$ and $\Omega = 7/2$ levels are degenerate because pairing correlation lowers the $K = 0$ state alone. One the other hand, high-K states have smaller energy loss in rotational energy which amounts to $(I(I+1) - K^2)/2\mathcal{I}$. Here we consider the competition of the 4^+ states with $K = 0$ and $K = 4$. The pairing energy estimated from the binding energies of $^{43-45}$S is about 2.5 MeV, which corresponds to the excitation energy of the 4^+ level dominated by $K = 4$. The 4^+ level dominated by $K = 0$ estimated from the experimental 2_1^+ level in ^{44}S and a normal ratio

$E_x(4^+)/E_x(2^+) = 2.5$ is about 3 MeV. The competition between pairing energy and rotational energy thus accounts for the reason why the 4^+ level with $K = 4$ is located lower than the one with $K = 0$.

In this way, we are successful in giving a unified and comprehensive picture about the occurrence of isomeric states in neutron-rich sulfur isotopes.

References

[1] B. Bastin *et al.*, Phys. Rev. Lett. **99** (2007) 022503.
[2] D. Santiago-Gonzalez *et al.*, Phys. Rev. C **83** (2011) 061305(R).
[3] F. Sarazin *et al.*, Phys. Rev. Lett. **84** (2000) 5062.
[4] Y. Utsuno *et al.*, arXiv:1407.0444 (2014).
[5] Y. Utsuno *et al.*, Phys. Rev. C **86** (2012) 051301(R).
[6] T. R. Rodríguez and J. L. Egido, Phys. Rev. C **81**, 064323 (2010).
[7] T. R. Rodríguez and J. L. Egido, Phys. Rev. C **84**, 051307(R) (2011).
[8] R. Chevrier and L. Gaudefroy, Phys. Rev. C **89**, 051301(R) (2014).
[9] P. M. Walker and G. D. Dracoulis, Nature **399**, 35 (1999).

Density profiles of Be isotopes based on Monte Carlo shell model

T. Yoshida[a], N. Shimizu[a], T. Abe[b] and T. Otsuka[a, b, c]

[a] *Center for Nuclear Study, Graduate School of Science, University of Tokyo*
[b] *Department of Physics, University of Tokyo*
[c] *National Superconducting Cyclotron Laboratory, Michigan State University*

Ab initio calculations have recently started for light nuclei $A \leq 14$. One example is the Green's function Monte Carlo (GFMC) [1] approach. In its analysis of $A = 8$ nuclei, the two-α-cluster shape emerges *a priori* from the density distribution. This achievement is important for the shell-model calculations. The problem when we use the usual shell-model space is that the single-particle orbits are expanded around the one center of the harmonic oscillator potential. Therefore, discussions for the α-cluster configuration in view of intrinsic shape has been difficult so far. Recently, the size of the model space which is tractable in the shell-model calculation has increased due to the development of parallel computers and methodology of shell-model calculations. In fact, the deformation and cluster-like shape for Li isotopes have been investigated by using no core full configuration (NCFC) approach [2]. Another approach is the Monte Carlo shell model (MCSM) [3] method which has been applied to various nuclei by using recent parallel computers with sophisticated energy-minimum search where the conjugate gradient method and energy-variance extrapolation [4, 5] are combined.

In this report, we show the exsitence of the α-cluster strucutre based on the MCSM. We focus on the ground state of ^{8,10}Be which are expected to have the two-cluster configuration. In the case of ^{10}Be, the density for the valence neutrons is discussed. We extend the size of the model space from the previous study [6] by taking large number of basis states into account. The detail of the definition of the intrinsic wave function based on the MCSM has been discussed in Refs. [5, 7]. In Fig. 1, the proton densities for the 0^+ ground state of ^{8}Be are shown. Here, the densities in the laboratory system, which have spherical shape are shown in the left figures. The densities of the wave function Φ (before alignment) are shown in the middle figures. The intrinsic densities of the wave function Φ^{intr} are shown in the right figures.

Here, we use the JISP16 NN interaction which reproduces NN scattering data and properties of deuteron and other light nuclei [8]. We depict the density of Φ^{intr} by changing the number (N_b) of the bases states, which are described by a Slater determinant of Φ. As shown in the results of $N_b = 1$, a clear deformation and its neck structure to be called dumbbell shape appear. We can see that as the number of the Slater determinants increases, the densities before the alignment (middle) becomes vaguer because of the mixture of different directions of principal axes of the basis states. On the other hand, the intrinsic densities (right) have clearer dumbbell-like structure for any N_b. In addition, the density distribution of the intrinsic state is almost unchanged with respect to N_b. This result indicates the appearance of cluster structure. Since the number of particles for opposite sides of the principal axis is almost the same, this state can be considered as two α clusters. This result is similar to that of the GFMC [1].
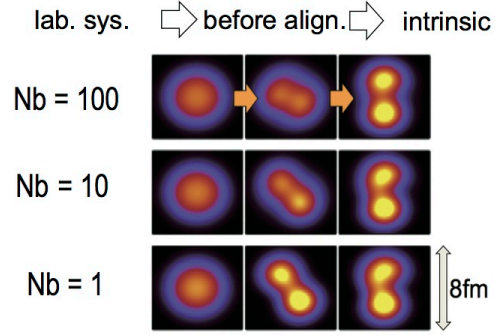
Figure 1: ^{8}Be proton densities in the laboratory system with J-projected states, (left) and before alignment of principal axes of unprojected basis states, (middle) and of intrinsic state (right) for various N_b and slices along yz plane. The numbers of basis states are $N_b = 1, 10$ and 100 for the lower, middle and upper figures, respectively. Slices along yz plane are $x = 0$ fm plane for each figure. The size of each box is 8×8 fm^2. The model space and harmonic oscillator energy are $N_{shell}=4$ and $\hbar\omega$=20 MeV, respectively.
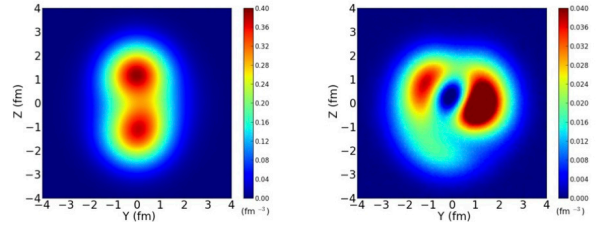
Figure 2: The densities of the 0^+ ground state for ^{10}Be are shown. The number of basis states is $N_b = 100$. The model space and harmonic oscillator energy are $N_{shell}=4$ and $\hbar\omega$=25 MeV, respectively. The intrinsic densities for matter and valence neutrons are shown (left and right figures, respectively).

We perform the same analysis for the 0^+ ground state of ^{10}Be. Here, we use the number of major shell, $N_{shell}=4$ and harmonic oscillator parameter, $\hbar\omega$=25 MeV. The wave function is determined by the conjugate gradient method, where the number of basis states is $N_b = 100$. We depict the densities as shown in Fig. 2. The valence-neutron density is estimated by subtracting the proton density from the neutron density. We find the ^{8}Be-like core in the matter density which has two-α-cluster structure. We see that the valence neutrons are located mainly at $z \sim 0$ region. The asymmetric distribution indicates the appearance of the correlation between the valence neutrons. This picture is consistent with the behavior of π-orbit in the molecular or-

bital model of ^{10}Be [9]. However, it is necessary to clarify whether the present analysis is valid with larger model spaces with respect to N_{shell}. The effects of the Coulomb interaction and contamination of spurious center of mass motion should be studied in the future.

References

[1] R. B. Wiringa, S. C. Pieper, J. Carlson and V. R. Pandharipande, *Phys. Rev.* C **62**, 014001 (2000).

[2] C. Cockrell, J. P. Vary and P. Maris, *Phys. Rev.* C **86**, 034325 (2012).

[3] T. Abe, P. Maris, T. Otsuka, N. Shimizu, Y. Utsuno and J. P. Vary, *Phys. Rev.* C **86**, 054301 (2012).

[4] T. Otsuka, M. Honma, T. Mizusaki, N. Shimizu and Y. Utsuno, *Prog. Part. Nucl. Phys.* **47**, 319 (2001).

[5] N. Shimizu, T. Abe, Y. Tsunoda, Y. Utsuno, T. Yoshida, T. Mizusaki, M. Honma and T. Otsuka, *Prog. Theor. Exp. Phys.* **2012**, 01A205 (2012).

[6] T. Yoshida, N. Shimizu, T. Abe and T. Otsuka, J. Phys. Conf. Ser. **445**, 012038 (2013).

[7] T. Yoshida, N. Shimizu, T. Abe and T. Otsuka, EPJ Web of Conferences **66**, 02113 (2014).

[8] A. M. Shirokov, J. P. Vary, A. I. Mazur, S. A. Zaytsev and T. A. Weber, *Phys. Lett.* B **621**, 96 (2005).

[9] N. Itagaki and S. Okabe, *Phys. Rev.* C **61**, 044306 (2000).

GPGPU application to the Monte Carlo shell model

T. Togashi[a], N. Shimizu[a], Y. Utsuno[a,b], T. Abe[c], T. Otsuka[a,c]

[a]*Center for Nuclear Study, Graduate School of Science, University of Tokyo*
[b]*Advanced Science Research Center, Japan Atomic Energy Agency*
[c]*Department of Physics, University of Tokyo*

General-Purpose computing on the Graphics Processing Unit (GPGPU) can be implemented with comparative ease in the Monte Carlo shell model since the main computational problems are attributed to the operations of matrices and/or vectors in the computation of the Hamiltonian matrix elements. Recent computation with a Graphics-Processing-Unit (GPU) accelerator demonstrates greater performance for matrix operations than CPU computing [1]. Hence, we attempt to apply GPGPU to the computation of Hamiltonian matrix elements in the Monte Carlo shell model for higher performance. In our work, the CPU computing is also assigned to operations which are not well suited for the GPU computing such as hybrid CPU-GPU platforms [2]. The detail of this work is reported in [3].

The computational method is summarized in the following. The Slater determinant of the state q in the Monte Carlo shell model is represented as

$$|\Phi(q)\rangle = P_{MK}^{J^\pi} \prod_i^{N_f} \left(\sum_l^{N_s} D(q)_{li} c_l^\dagger \right) |-\rangle,$$

where $P_{MK}^{J^\pi}$ is the projection operator for a give spin and parity (J^π), N_f and N_s are the numbers of fermions regarded as nucleons and the number of single-particle states of a harmonic-oscillator orbit, respectively. $D(q)_{li}$ is a complex $N_s \times N_f$ ($N_s \geq N_f$) matrix and $c_l^\dagger$ is a creation operator which generates the single-particle state of a nucleon from a vacuum $|-\rangle$. The main computational problem is attributed to calculate the norm and Hamiltonian matrices. The norm matrix $N(q', q)$ and the Hamiltonian matrix $H(q', q)$ are written as

$$N(q', q) = \sum_r^{N_m} W^r \det\left(D(q')^\dagger \cdot D(q^r) \right),$$

$$H(q', q) = \sum_r^{N_m} W^r \det\left(D(q')^\dagger \cdot D(q^r) \right) H^0(q', q^r),$$

where q^r denotes the rotated state of q by a Euler angle Ω^r, W^r is the Wigner D function for Ω^r, and N_m is the number of mesh points for a three-dimensional integration over the Euler angle in the J^π projection. $H^0(q', q^r)$ is written as

$$H^0(q', q^r) = \sum_{l_1 l_2}^{N_s} t_{l_1 l_2} \, \rho_{l_2 l_1}(q', q^r)$$

$$+ \frac{1}{2} \sum_{l_1 l_2 l_3 l_4}^{N_s} \rho_{l_3 l_1}(q', q^r) \, \bar{v}_{l_1 l_2, l_3 l_4} \, \rho_{l_4 l_2}(q', q^r),$$

where $t_{l_1 l_2}$ and $\bar{v}_{l_1 l_2, l_3 l_4}$ denote the one- and two-body matrix elements, respectively, and $\rho(q', q^r)$ is the density matrix: $\rho(q', q) = D(q) \cdot \left(D(q')^\dagger \cdot D(q) \right)^{-1} \cdot D(q')^\dagger$. The

numerical calculation directly using the above equation is inefficient because $\bar{v}_{l_1 l_2, l_3 l_4}$ is very sparse. Hence, we convert the sparse matrix $\bar{v}_{l_1 l_2, l_3 l_4}$ into the block-dense matrix as described in [4]:

$$\frac{1}{2} \sum_{l_1 l_2 l_3 l_4}^{N_s} \rho_{l_3 l_1}(q', q^r) \, \bar{v}_{l_1 l_2, l_3 l_4} \, \rho_{l_4 l_2}(q', q^r)$$

$$= \frac{1}{2} \sum_{\Delta m} \sum_{k'k} \tilde{\rho}\left(-\Delta m, q', q^r\right)_{k'} \times$$

$$\tilde{v}\left(-\Delta m, \Delta m\right)_{k'k} \tilde{\rho}\left(\Delta m, q', q^r\right)_k,$$

where the sets of (l_1, l_3) and (l_2, l_4) with $\Delta m_{13} = j_z(l_1) - j_z(l_3)$ and $\Delta m_{24} = j_z(l_2) - j_z(l_4)$ being $\Delta m_{13} = -\Delta m_{24} = -\Delta m$, respectively, are indexed by k' and k. This equation is regarded as a ^{t}(vector) $\times$ (matrix) $\times$ (vector) operation to be $^t\tilde{\rho} \cdot \tilde{v} \cdot \tilde{\rho} = \sum_{\Delta m} {}^t\tilde{\rho}(-\Delta m) \cdot \tilde{v}(-\Delta m, \Delta m) \cdot \tilde{\rho}(\Delta m)$. The (matrix) $\times$ (vector) operation $\tilde{v} \cdot \tilde{\rho}$, which costs most of the computational time, is repeated a number of times for different $\tilde{\rho}$'s: $\tilde{v} \cdot \tilde{\rho}^{(1)},...,\tilde{v} \cdot \tilde{\rho}^{(N_m)}$. By binding N_b's vectors $\tilde{\rho}^{(1)}, ..., \tilde{\rho}^{(N_b)}$ into a matrix $\theta \equiv (\tilde{\rho}^{(1)}, ..., \tilde{\rho}^{(N_b)})$, repeated (matrix) $\times$ (vector) operations are carried out by a (matrix) $\times$ (matrix) operation $\tilde{v} \cdot \theta$. Here, N_b can be chosen arbitrarily as the chunk parameter. In the previous work [4], the matrix multiplication of $\tilde{v} \cdot \theta$ computed by the BLAS interface allowed us to achieve efficient performance in the CPU computing. In the present work, the computation of $\tilde{v} \cdot \theta$ is performed by the cuBLAS [1] interface on a GPU device.

As the computational benchmark system, we consider the 0^+ states composed of eight protons and eight neutrons with no inert core, i.e., ^{16}O, and the Hamiltonian is taken as a JISP16 interaction [5]. We introduce N_{shell} as the number of major shells and adopt the model space for $N_{\text{shell}} = 4$, 5, 6 and 7. For the measurement of estimating the elapsed time, we compute the Hamiltonian matrix elements among 5 different Slater determinants, which lead to 15 different matrix elements due to the Hermiticity of the Hamiltonian matrix.

The present computational environment is composed of an AMD Opteron 6274 processor with a clock speed of 2.20 GHz and a NVIDIA Tesla K20X GPU accelerator. The theoretical peak performance of the CPU is 17.6 GFLOPS per a CPU core. The GPU accelerator has the theoretical peak performance of 1.31 TFLOPS for double precision. Our code, written in Fortran 90/95/2003, is compiled by PGI Accelerator Fortran Compiler Version 13.10 with the option to designate NVIDIA CUDA Version 5.0.

Figure 1 shows the GPU computing achieves about 42 and 27 times better performance of the single-threaded process of the CPU in the case of $N_{\text{shell}} = 7$ for the two-body part in Hamiltonian matrix elements and total computation, respectively. In Fig. 2, the performance of the GPU in FLOPS shows the execution efficiency reaches about 50% of the theoretical peak performance of 1.31 TFLOPS for
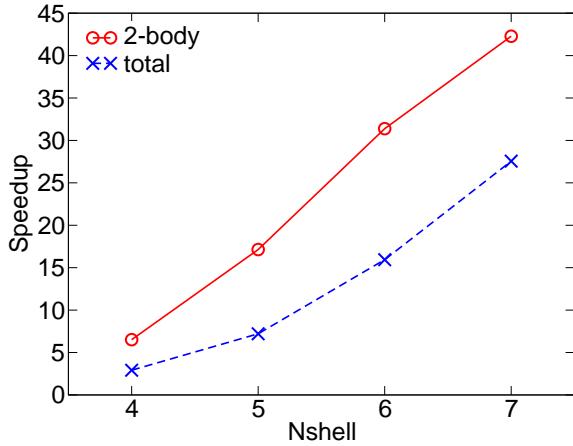
Figure 1: Speedup of the performance of the GPU computing to the single-threaded process of the CPU for the two-body part in Hamiltonian matrix elements labeled '2-body' and total computation labeled 'total' in each N_{shell}.
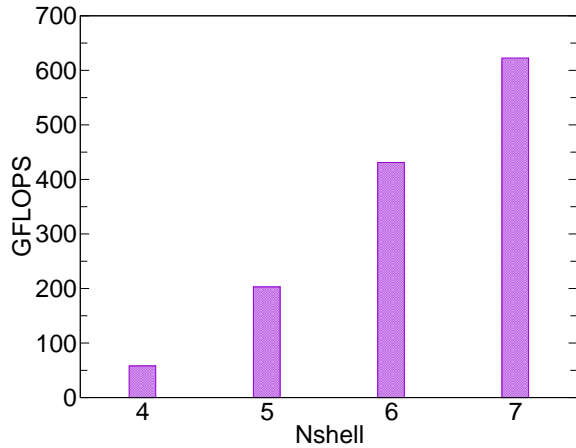
Figure 2: Performance in FLOPS of the GPU computing for the two-body part in Hamiltonian matrix elements in each N_{shell}.

the computation of $N_{\text{shell}} = 7$. While the performance of the single-threaded process of the CPU changes slightly from about 10 to 15 GFLOPS with the increase of N_{shell}, which represents the saturation of the performance of the CPU process, the performance of the GPU computing is improved gradually for larger model space. The present results demonstrate the applicability with high performance of GPGPU for the case of large model space in the Monte Carlo shell-model calculation. However, since the memory size of the two-body matrix elements $\tilde{v}$ requires more gigabytes for $N_{\text{shell}} \geq 8$ as shown in Fig. 3 of [4], in the larger model space, one GPU computing would not be feasible and it would be indispensable to introduce multi-GPGPU environment. We now extend this computation to multi-GPU parallelization.

References

[1] NVIDIA Developer Zone.
https://developer.nvidia.com/cuBLAS.

[2] P. Benner, P. Ezzatti, E. S. Quintana-Ortí and A. Remón, Eurp-Par 2009 Parallel Processing Workshops, Lecture Notes in Computer Science **6043** (2010) 132.

[3] T. Togashi, N. Shimizu, Y. Utsuno, T. Abe, and T. Otsuka, Procedia Computer Science **29** (2014) 1711.

[4] Y. Utsuno, N. Shimizu, T. Otsuka, and T. Abe, Comp. Phys. Comm. **184** (2013) 102.

[5] A. M. Shirokov, J. P. Vary, A. I. Mazur, and T. A. Weber, Phys. Lett. B **644** (2007) 33.

Code development for nuclear shell-model calculations

N. Shimizu

Center for Nuclear Study, Graduate School of Science, University of Tokyo

Nuclear shell-model calculation has been playing an important role to understand low-energy nuclear physics [1, 2]. In shell-model calculations, we usually use a harmonic-oscillator basis as a single-particle orbit, and define a certain group of active orbits (e.g. valence shell) as a model space. Then, we solve many-body problem including many-body correlation fully inside the model space and discuss physical quantities, such as low-lying spectra. The contribution from outside the model space is renormalized into the effective interaction.

The simplest representation for many-body basis state is called "M-scheme" state and described as

$$|M_i\rangle = \prod_{\alpha=1}^{A} c^\dagger_{M_i^{(\alpha)}} |-\rangle \qquad (1)$$

where A, $|-\rangle$ are a number of active nucleons and an inert core, respectively. The $c^\dagger_{M_i^{(\alpha)}}$ denotes a creation operator of the singles-particle state, $M_i^{(\alpha)}$. $M_i^{(\alpha)}$ denotes a single-particle state which is occupied by α-th active nucleon. $M_i = \{M_i^{(1)}, M_i^{(2)}, ..., M_i^{(A)}\}$ is called "configuration" and means that 1st, 2nd, ..., A-th particles occupy $M_i^{(1)}, M_i^{(2)}, ..., M_i^{(A)}$ single-particle states respectively. Since the model space is completely spanned by the M-scheme basis states, the shell-model wave function is expressed as a linear combination of them such as

$$|\Psi\rangle = \sum_{i=1}^{D} v_i |M_i\rangle. \qquad (2)$$

The number of the M-scheme basis, D, is called M-scheme dimension. The coefficients v_i are obtained by solving Schrödinger's equation in M-scheme such as

$$\sum_{j=1}^{D} \langle M_i|H|M_j\rangle v_j = E v_i. \qquad (3)$$

The D tends to be huge and, for example, reaches 10^9 in the case of ^{56}Ni with pf-shell model space. Therefore, it is important to develop a computer program for utilizing supercomputers in order to solve Eq.(3) efficiently.

In the last two decades, more than a dozen of shell-model codes had been developed (e.g. [3–8]). However, there is no code which is available to the public and applicable to MPI parallel computation still now. Hence, we developed a new code "KSHELL" fully from scratch for massive parallel computation with OpenMP-MPI hybrid. This code is written in Fortran 95 with ISO TR15581 extension. It is equipped with dialogue-type user interface written in python 2.

In KSHELL, Eq.(3) is solved numerically utilizing Thick-Restart Lanczos method [9], which is a kind of the Lanczos method and suppresses the number of the Lanczos vectors causing the reduction of reorthogonalization process. During the Lanczos iteration, the state vector is projected out to a good total-angular-momentum state optionally. This projection is performed by doing the Lanczos

method recursively to minimize the expectation value of total angular momentum. This option is convenient for the computation of highly excited non-yrast states.

In the Lanczos algorithm, the bottle neck of computation is matrix-vector product. The code is based on the M-scheme basis and proton-neutron factorization algorithm similarly to some preceding codes [5–7]. The matrix-vector product is performed with "on-the-fly" generation of the Hamiltonian matrix elements utilizing proton-neutron factorization of a M-scheme basis. An M-scheme basis state is expressed and manipulated by the bit representation efficiently. The basic concept of this algorithm is found at Ref. [7].

In order to fit massive parallel computation and to apply arbitrary truncation scheme, the whole M-scheme space is split into subspaces by specifying the occupation numbers of each single-particle orbit and z-component of angular momentum of protons. A unit of this subspace is called a "partition" or a "sector". We split the matrix-vector product into small parts corresponding to these partitions and calculate them in parallel.

A major restriction of the capability of large-scale shell-model calculations is the necessity of large memory. In practical calculations, at least two Lanczos vectors should be stored on main memory for efficient matrix-vector multiplication. The size of the two Lanczos vectors reaches huge, e.g. 80GB in the case of 10^{10} dimension, and surpasses typical memory size of a PC. This restriction is overcome by splitting the Lanczos vectors in units of "partition" and distributing them on the main memories of MPI nodes on an equal footing. Moreover, utilizing a large number of nodes allows us to store the whole Lanczos vectors (~ 100 vectors) on memory. It shortens the time to reorthogonalize these Lanczos vectors drastically.

Figure 1: Parallel performance of "KSHELL" code at K computer and FX10 supercomputer. The lines are shown to guide the eye.

Figure 1 shows the parallel performance of KSHELL at K computer and FX10 supercomputer at the University of Tokyo. We measured the computation time of the Lanczos one iteration for ^{56}Ni with pf shell and KB3 interaction [10]. The inverse of time is plotted against the number of CPU cores . The computation time is in inverse proportion to the number of CPU core almost perfectly. It shows

good strong scaling up to 8192 cores at FX10. Utilizing 8192 cores, it takes 145 seconds to compute the ground-state energy of ^{56}Ni in pf-shell, corresponding the eigen-value problem of 1,087,455,228-dimension matrix. This code copes with $O(10^{10})$ M-scheme dimension and, hopefully, larger dimension. This code runs also on a PC and its performance scales almost perfectly to the number of CPU cores with OpenMP threads.

This code can also compute quadrupole and magnetic moments, and $E2$ and $M1$ transition probabilities without additional manipulation. Three-body force is out of its purpose.

References

[1] B. A. Brown, Prog. Part. Nucl. Phys. **47**, 517, (2001).

[2] E. Caurier, G. Martinez-Pinedo, F. Nowacki, A. Poves, and A. P. Zuker, Rev. Mod. Phys. **77**, 427 (2005).

[3] B. A. Brown, A. Etchegoyen, and W. D. M. Rae, computer code OXBASH, the Oxford University-Buenos Aires-MSU shell model code, Michigan State University Cyclotron Laboratory Report No. 524, 1985.

[4] B. A. Brown and W. D. M. Rae, NUSHELL@MSU, MSU NSCL Report, 2007 (unpublished).

[5] E. Caurier and F. Nowacki, Acta Phys. Pol. B **30**, 705 (1999)

[6] T. Mizusaki, N. Shimizu, Y. Utsuno, and M. Honma, code MSHELL64, unpublished.

[7] C. W. Johnson, W. E. Ormand, and P. G. Krastev, Comp. Phys. Comm. **184**, 2761 (2013).

[8] P. Maris, M. Sosonkina, J. P. Vary, E. Ng, and C. Yang, Procedia Comp. Sci. **1**, 97 (2010).

[9] K. Wu and H. Simon, SIAM. J. Matrix Anal. & Appl., **22(2)**, 602 (2000).

[10] A. Poves and A. Zuker, Phys. Rep. **70**, 235 (1981).

Other Activities

Laboratory Exercise for Undergraduate Students

S. Ota, K. Yako, M. Niikura[a], T. Miyazaki[a], S. Momiyama[a], H. Sakurai[a,b] and S. Shimoura

Center for Nuclear Study, Graduate School of Science, University of Tokyo
[a]*Department of Physics, University of Tokyo*
[b] *RIKEN Nishina Center*

Nuclear scattering experiments were performed as a laboratory exercise for undergraduate students of the University of Tokyo. This program was aiming at providing undergraduate students with an opportunity to learn how to study subatomic physics by using an ion beam from an accelerator. In 2013, 31 students attended this program.

The four beam times were scheduled in the second semester for third-year students, and 8 students participated in each beam time. The experiments were performed at the RIBF using a 26-MeV alpha beam accelerated in the AVF cyclotron. The alpha beam extracted from the AVF cyclotron was transported to the E7B beam line in the E7 experimental hall. The scattering chamber has two separate target ports which enable us to perform two independent experiments. In each beam time, the students were divided into two groups and took one of the following two subjects:

1. Measurement of elastic scattering of incident alpha particle with ^{197}Au, to learn how to determine nuclear size.

2. Measurement of gamma rays emitted from the cascade decay of highly excited ^{154}Gd and ^{184}Os, to learn on the nuclear deformation.

Before the experiment, the students took a course on the basic handling of the semiconductor detectors and electronic circuits at the Hongo campus, and attended a radiation safety lecture at RIKEN. They also joined a tour to the RI beam factory at RIKEN.

In the $\alpha+^{197}$Au measurement, the Au target with a thickness of 1.42 mg/cm2, and α particles scattered from the Au target were detected using a silicon PIN-diode located 11 cm away from the target. A collimator with a diameter of 6 mm was attached on the silicon detector. The energy spectrum of the scattered α particles was recorded by a multi-channel analyzer (MCA) system. The beam was stopped by a Faraday cup in the scattering chamber. The cross section for the alpha elastic scattering was measured in the angular range of $\theta_{\mathrm{lab}} = 25-160°$.

The measured cross section was compared with the calculated cross section for the Rutherford scattering. The cross section was also analyzed by the potential model calculation, and the radius of the gold nucleus was discussed. Some students obtained the radius of 10 fm by using a classical model where the trajectory of the α particle in the nuclear potential is obtained using the Runge-Kutta method. Others tried to understand the scattering process by calculating the angular distribution using the distorted wave Born approximation method with a Coulomb wave function and a realistic nuclear potential.

In the measurement of gamma rays, excited states in ^{154}Gd and ^{184}Os nuclei were populated by the ^{152}Sm(α,2n) and ^{182}W(α,2n) reactions, respectively. The gamma rays emitted from the cascade decay of the rotational bands were measured by a high-purity germanium detector located 50-cm away from the target. The energy of the gamma ray were recorded by the MCA system. The gain and the efficiency of the detector system had been calibrated with standard gamma-ray sources of ^{22}Na, ^{60}Co, ^{133}Ba, and ^{137}Cs. The gamma rays from the 10^+ and 8^+ states in ^{154}Gd and ^{184}Os were successfully identified. Based on the energies of the gamma rays, the moment of inertia and the deformation parameters of the excited states were discussed by using a classical rigid rotor model and a irrotational fluid model. The students found that the reality lies between the two extreme models. The initial population among the levels in the rotational band was also discussed by taking the effect of the internal conversion into account.

It was the first time for most of the students to use large experimental equipments. They learned basic things about the experimental nuclear physics and how to extract physics from the data. We believe this program was very impressive for the students. The authors would like to thank Dr. Y. Uwamino, the CNS accelerator group, and the RIBF cyclotron crew for their helpful effort in the present program.

Irradiation of ^{7}Be and ^{22}Na beams for wear diagnostics application

A. Yoshida, T. Kambara, H. Takeichi, R. Uemoto[a], N. Takahashi[b], H. Yamaguchi[c], T. Nakao[c] and D. Kahl[c]

RIKEN Nishina Center for Accelerator-Based Science (RNC)
[a]*S.H.I. Examination and Inspection (SHIEI) Ltd.*
[b]*Sumitomo Heavy Industries, Ltd.*
[c]*Center for Nuclear Study (CNS), University of Tokyo*

In order to develop a method for wear diagnostics of industrial material using RI beams as tracers [1], irradiation experiments of intense ^{7}Be and ^{22}Na beams were performed using CRIB facility. These experiments were scheduled under the collaborative research agreement among RNC, CNS and private companies. RI nuclei are implanted in a near surface of the machine parts, and its wear-loss is evaluated by the decrease in the measured radioactivity. Continuous detection of γ rays from the outside of the machine enables real-time diagnostics of wear in running machines. For this purpose, intense beams of RI nuclei ^{7}Be ($T_{1/2}$ = 53d) and ^{22}Na ($T_{1/2}$ = 2.6y) were provided using CRIB.

The ^{7}Be beam was produced via $p(^7$Li,^{7}Be)n reaction. A primary beam of ^{7}Li^{2+} with the energy of 5.7 MeV/u and intensity of 1.7 *particle* μA (pμA) in average was introduced to the cryogenic H$_2$ gas target. The H$_2$ gas at a pressure of 760 *Torr* was cooled by liquid N$_2$ in a vessel at 90 K and circulated to the gas cell at a rate of 30 *slm*. The calculated energy loss in the gas target was 1.4 and 5.9 Watt at the exit Havar foil of 2.5 μm in thickness and in the target gas, respectively. During two days experiment, the target was stable, but the primary beam intensity was a bit unstable. CRIB control program became unresponsive two times, it seems related to high radiation dose of neutron caused by the RI beam production reaction. The produced ^{7}Be beam was introduced to the F2 focal plane without degrader foil at F1. At the F2 focal plane, a dedicated vacuum chamber fabricated by the industrial cooperation team (RNC) was installed. A position sensitive Si-detector (PSD, Hamamatsu S5378-02), a rotating energy degrader and a rotating irradiation sample holder were installed in the chamber. The profiles of secondary beams were measured using the PSD detector. The energy and beam spot size of the ^{7}Be^{4+} beam was 29.1 MeV (4.16 MeV/u) and 4.8×8.1 mm in fwhm, respectively, with a momentum slit of $\pm$ 3.1% ($\pm$ 50 mm) at F1. The beam spot size was a bit large. It seems related to a halo of beam spot at the gas target. The implanted dose rate of the ^{7}Be beam was 60 kBq/h, approximately, obtained by the following γ-ray measurement.

The ^{22}Na beam was produced via the $p(^{22}$Ne,^{22}Na)n reaction. A primary beam of ^{22}Ne^{7+} with energy of 6.1 MeV/u and intensity of 0.25 pμA in average was introduced to the gas target. The H$_2$ gas at a pressure of 400 *Torr* was cooled to 90 K and circulated to the gas cell at a rate of 20 *slm*. The calculated energy loss in the gas target was 2.1 and 4.5 Watt at the exit Havar foil and at the target gas, respectively. The Havar foil was broken when the primary beam intensity exceeded 0.30 pμA. During three days experiment, the primary beam intensity was almost stable, but the CRIB control program became unresponsive two times. The produced ^{22}Na beam was introduced to the F2 focal plane without degrader foil at F1. The energy and size of the ^{22}Na^{11+} beam was 80.8 MeV (3.67 MeV/u) and 4.7×4.3 mm in fwhm, respectively, with a momentum slit of $\pm$ 3.1% ($\pm$ 50 mm) at F1. The implanted dose rate was 0.3 kBq/h, approximately.

In order to control the implantation depth close to the surface, a rotating energy degrader (Fig.1) was newly introduced. Eight sets of aluminum foils can be mounted on a rotating wheel of 14 cm diameter. The wheel rotates with 12 *rpm* in speed using a vacuum motor. A beam collimator of 10 mm diameter is assembled at the down-stream of the wheel and a fixed-thickness degrader foil can be mounted on it. The stability of the secondary beam intensity was monitored by measuring a current from the collimator using a pico-ampere meter during the irradiation.
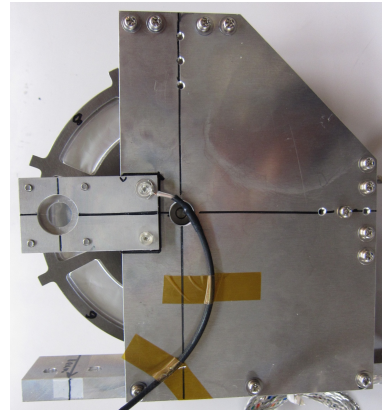
Figure 1: Rotating energy degrader unit.

To investigate the implantation-depth profile, a stack of 2-μm-thick aluminum foils were irradiated. After irradiation, the stack was disassembled and the intensity of the γ ray was measured using a Ge detector. As an example, ^{22}Na beam of narrow momentum distribution ($\pm$ 1 % at F1) was irradiated to the stack passing through seven sets of aluminum degrader foils; 4.9, 7.6, 11.9, 16.9, 23.8, 27.4, 31.7 μm in thickness. An obtained depth profile is shown in Figure 2. The black circles indicate a normalized fraction of each Al-foil measured by the stacked foil method using the Ge detector. The X and Y error bars indicate the thickness and the statistical error of each Al-foil data point. The range of ^{22}Na beam in aluminum is calculated by the SRIM code [2] using a measured beam energy spectrum obtained by the PSD detector. The dotted line is the continuous range spectrum. Below 5 μm in thickness, the range spectrum could not be measured as it was below the detector threshold, unfortunately. The triangles indicate a normalized fraction of each Al-foil calculated by re-binning of the continuous range spectrum. Here, a factor of 0.97 was applied for the stopping power calculated by the SRIM code, and then a good agreement between the data points

of Ge and PSD was obtained. We can conclude that the energy measurements using a Si detector gives a continuous implantation-depth profile with good accuracy.
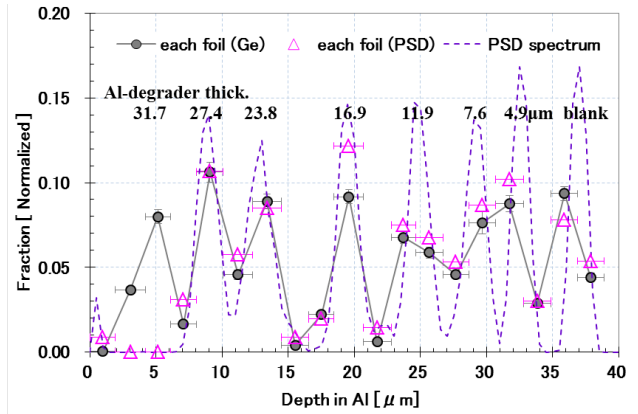
Figure 2: Implantation-depth profile of ^{22}Na beam into a stacked aluminum foils. The X error bars indicate the thickness of each foil as 2 μm, approximately.

The accuracy of this implantation-depth profile is the most important data for successive wear-loss diagnostics. The conventional stacked foil method is reliable, because it directly measures implanted dose in the material. But it has a limitation for depth-resolution. The resolution depends how thinner foils with same implantation material we can provide. Even though the thin foils are provided, the assembling of many thin foils as a stack is a hard work. On the other hand, the energy measurement using Si detector is simple, but it should rely on a range calculation. Here, we should introduce a small correction factor for the stopping power of unstable ^{22}Na beam in aluminum calculated by the SRIM code. But we can determine the factor experimentally using the pulse-shaped depth profile beam mentioned above. Thus, a precise measurement of implantation-depth profile can be performed using Si detector and the SRIM code calibrated by the stacked foil method.

Acknowledgements

References
[1] A. Yoshida *et al.*, CNS Annual Report, **CNS-REP-92** (2012) 65-66.
[2] James F. Ziegler, The SRIM code, the stopping and range of ions in matter, http://www.srim.org .

The 12th CNS International Summer School (CNSSS13)

S. Ota, S. Michimasa, T. Gunji, Y. Iwata, T. Nakatsukasa[a], T. Otsuka[b], H. Sakai[a], H. Sakurai[a,b],
Y. Utsuno[c], H. Utsunomiya[d], T. Uesaka[a], and S. Shimoura

Center for Nuclear Study, Graduate School of Science, University of Tokyo
[a]*RIKEN Nishina Center*
[b]*Department of Physics, Graduate School of Science, University of Tokyo*
[c]*Japan Atomic Energy Agency*
[d]*Department of Physics, Konan University*

The 12th CNS International Summer School (CNSSS13) was organized jointly by the Center for Nuclear Study (CNS), the University of Tokyo in the period of August 28–September 3, 2013. The summer school was held at the Nishina hall in the Wako campus of RIKEN and at the Koshiba hall in the Hongo campus, the University of Tokyo.

This summer school aimed at providing graduate students and postdocs with basic knowledge and perspectives of nuclear physics. It consisted of lectures by leading scientists in the fields of both experimental and theoretical nuclear physics. Each lecture started with an introductory talk from the fundamental point of view and ended with up-to-date topics in the relevant field.

The list of lecturers and their title are shown below.

Baha Balantekin (University of Wisconsin-Madison, US),
"Neutrinos, nuclear astrophysics, and exotic nuclei"
Peter Egelhof (GSI, Germany),
"Nuclear Physics with Radioactive Beams at Storage Rings and with Active Targets"
Navin Alahari (GANIL, France),
"Old Wine in a new Bottle : Reactions with exotic beams at energies around the Coulomb barrier"
Reprecht Machleidt (University of Idaho, US),
"Nuclear forces"
Shoji Asai (The University of Tokyo, Japan),
"Higgs and SUSY"
Silvio Cherubini (INFN LNS, Italy),
"Quasi-free reaction mechanisms as a tool for studying nuclear processes of interest for astrophysics: Trojan Horse Method and Virtual Neutron Method"
Atsushi Tamii (RCNP, Japan),
"Electric dipole resonance, neutron skin and symmetry energy"
Yutaka Utsuno (JAEA / CNS, Japan),
"Large-scale shell-model calculations for exotic nuclei"
Pieter Doornenbal (RNC, Japan),
"In-beam gamma-ray spectroscopy of fast RI beams"

This year, 9 lecturers and 104 participants attended from nine countries. Five lecturers and 29 participants were from foreign institutes. Attendances communicated with each other in the free discussion time between the lectures and in the welcome and farewell parties in a relaxed atmosphere.

Five lectures on August 29 were held at the Koshiba hall in the Hongo campus and were broadcasted via Internet.

Young scientist sessions were also held in the school. 24 talks and 22 posters were presented by graduate students and postdocs.

All the information concerning the summer school is open for access at the following URL:

http://www.cns.s.u-tokyo.ac.jp/summerschool/cnsss13

Appendices

Symposium, Workshop, Seminar, PAC and External Review
CNS Reports
Publication List
Talks and Presentations
Personnel

Symposium, Workshop, Seminar, Colloquium, and PAC

A. Symposium and Workshop

1. The 12th international symposium on Origin of Matter and Evolution of Galaxies (OMEG12)
   November 18-22, 2013, Tsukuba

B. CNS Seminar

1. Dr. Shinya Wanajo (NAOJ):" :   vs.   ", Jul. 23, 2013, Hongo Campus.

2. Dr. Haozhao Liang (RIKEN Nishina Center): "Nuclear charge-exchange excitations in covariant density functional theory", Oct. 31, 2013, Hongo Campus.

3. Dr. Toshiyuki Sumikama (Tohoku University): "   Zr   Mo   110
   ", Nov. 7, 2013, Hongo Campus.

4. Dr. Jirina Stone (University of Oxford / University of Tennessee-Knoxville): "Neutron Rich Matter in Stellar Processes" Nov. 22, 2013, Hongo Campus.

5. Prof. Michio Kohno (Kyushu Dental University): "   3
   ", Nov. 28, 2013, Hongo Campus.

6. Prof. Bruce R. Barrett (University of Arizona): "The No Core Shell Model within an Effective Field Theory framework", Nov. 27, 2013, Hongo Campus.

7. Dr. Kosuke Nomura (GANIL): "Interacting boson model and nuclear mean field", Dec. 26, 2013, Hongo Campus.

8. Dr. Noriyoshi Ishii (University of Tsukuba): "LS force and anti-symmetric LS force from lattice QCD", Jan. 21, 2014, Hongo Campus.

C. Program Advisory Committee for Nuclear-Physics Experiments at RI Beam Factory

1. The 12th NP-PAC meeting
   Date: June 28 and 29, 2013
   Place: RIBF Conference Hall on the 2nd floor of the RIBF Building

2. The 13th NP-PAC meeting
   Date: December 13 and 14, 2013
   Place: RIBF Conference Hall on the 2nd floor of the RIBF Building

CNS Reports

#91 Mixed harmonic azimuthal correlations in $\sqrt{s_{NN}}$ = 2.76 TeV Pb-Pb collisions measured by ALICE at LHC Y. Hour, April, 2013

#92 "CNS Annual Report 2012"
Edited by S. Ota and Y. Soma March, 2014

Publication List

A. Original Papers

1. J.J. He, L. Y. Zhang, A. Parikh S.W. Xu, H. Yamaguchi, D. Kahl, S. Kubono, J. Hu, P. Ma, S.Z. Chen Y. Wakabayashi, B.H. Sun, H. W. Wang, W. D. Tian, R.F. Chen, B. Guo, T. Hashimoto, Y. Togano, S. Hayakawa, T. Teranishi, N. Iwasa, T. Yamada, and T. Komatsubara, "The ^{18}Ne$(\alpha, p)^{21}$Na breakout reaction in x-ray bursts: Experimental determination of spin-parities for α resonances in ^{22}Mg via resonant elastic scattering of ^{21}Na$+p$", Phys. Rev. C **88** 012801(R) (2013).

2. S. J. Jin, Y. B. Wang, J. Su, S. Q. Yan, Y. J. Li, B. Guo, Z. H. Li, S. Zeng, G. Lian, X. X. Bai, W. P. Liu, H. Yamaguchi, S. Kubono, J. Hu, D. Kahl, H. S. Jung, J. Y. Moon, C. S. Lee, T. Teranishi, H. W. Wang, H. Ishiyama, N. Iwasa, T. Komatsubara, and B. A. Brown, "Resonant scattering of ^{22}Na + p studied by the thick-target inverse-kinematic method", Phys. Rev. C **88**, 035801 (2013).

3. H. Muto, Y. Ohshiro, S. Yamaka, S. Watanabe, M. Oyaizu, S. Kubono, H. Yamaguchi, M. Kase, T. Hattori, S. Shimoura, "Grating monochromator for electron cyclotron resonance ion source operation", Review of Scientific Instruments **84** 073304 (2013).

4. Y. Ohshiro, S. Yamaka, S. Watanabe, K. Kobayashi, Y. Kotaka, M. Nishimura, M. Kase, H. Muto, H. Yamaguchi, S. Shimoura, "Production of beams from solid materials at center for nuclear study electron cyclotron resonance ion source", Rev. of Sci. Instrum. **85** 02A912 (2013).

5. N. Duy, S. Kubono, H. Yamaguchi, D. Kahl, Y. Wakabayashi, T. Teranishi, N. Iwasa, Y. Kwon, L. Khiem, Y. Kim, J. Song, J. Hu, Y. Ayyad, "Low-energy radioactive ion beam production of ^{22}Mg", Nucl. Instr. and Meth. in Phys. Res. A, **723** 99–101 (2013).

6. J.J. He, L. Y. Zhang, A. Parikh S.W. Xu, H. Yamaguchi, D. Kahl, S. Kubono, J. Hu, P. Ma, S.Z. Chen Y. Wakabayashi, B.H. Sun, H. W. Wang, W. D. Tian, R.F. Chen, B. Guo, T. Hashimoto, Y. Togano, S. Hayakawa, T. Teranishi, N. Iwasa, T. Yamada, and T. Komatsubara, "The ^{18}Ne$(\alpha,p)^{21}$Na breakout reaction in x-ray bursts: Experimental determ ination of spin-parities for α resonances in ^{22}Mg via resonant elastic scattering o f ^{21}Na$+p$" Phys. Rev. C **88**, 012801(R) (2013).

7. S.J. Jin, Y.B. Wang, J. Su, S. Q. Yan, Y.J. Li, B. Guo, Z.H. Li, S. Zeng, G. Lian, X.X. Bai, W.P. Liu, H. Yamaguchi, S. Kubono, J. Hu, D. Kahl, H.S. Jung, J.Y. Moon, C.S. Lee, T. Teranishi, H.W. Wang, H. Ishiyama, N. Iwasa, T. Komatsubara, and B.A. Brow, "Resonant scattering of ^{22}Na + p studied by the thick-target inverse-kinematic method" Phys. Rev. C **88**, 035801 (2013).

8. L. Y. Zhang, J. J. He, A. Parikh, S. W. Xu, H. Yamaguchi, D. Kahl, S. Kubono, P. Mohr, J. Hu, P. Ma, S. Z. Chen, Y. Wakabayashi, H. W. Wang, W. D. Tian, R. F. Chen, B. Guo, T. Hashimoto, Y. Togano, S. Hayakawa, T. Teranishi, N. Iwasa, T. Yamada, T. Komatsubara, Y. H. Zhang, X. H. Zhou, "Investigation of the thermonuclear ^{18}Ne$(\alpha,p)^{21}$Na reaction rate via resonant elastic scattering of ^{21}Na$+p$", Phys. Rev. C **89** (2014) 015804.

9. Y. Satou, J.W. Hwang, S. Kim, K. Tshoo, S. Choi, T. Nakamura, Y. Kondo, N. Matsui, Y. Hashimoto, T. Nakabayashi, T. Okumura, M. Shinohara, N. Fukuda, T. Sugimoto, H. Otsu, Y. Togano, T. Motobayashi, H. Sakurai, Y. Yanagisawa, N. Aoi, S. Takeuchi, T. Gomi, M. Ishihara, S. Kawai, H.J. Ong, T.K. Onishi, S. Shimoura, M. Tamaki, T. Kobayashi, Y. Matsuda, N. Endo, M. Kitayama, "One-neutron knockout reaction of 17C on a hydrogen target at 70 MeV/nucleon ", Phys. Lett. B **728** (2014) 462–466.

10. H. Muto, Y. Ohshiro, S. Yamaka, S. Watanabe, M. Oyaizu, S. Kubono, H. Yamaguchi, M. Kase, T. Hattori, S. Shimoura, "Plasma spectroscopy of metal ions for hyper-electron cyclotron resonance ion source", Rev. Sci. Instrum. **85** (2014) 02A905.

11. Y. Ohshiro, S. Yamaka, S. Watanabe, K. Kobayashi, Y. Kotaka, M. Nishimura, M. Kase, H. Muto, H. Yamaguchi, S. Shimoura, "Production of beams from solid materials at Center for Nuclear Study electron cyclotron resonance ion source", Rev. Sci. Instru. **85** (2014) 02A912.

12. H. Suzuki, N. Aoi, E. Takeshita, S. Takeuchi, S. Ota, H. Baba, S. Bishop, T. Fukui, Y. Hashimoto, E. Ideguchi, K. Ieki, N. Imai, M. Ishihara, H. Iwasaki, S. Kanno, Y. Kondo, T. Kubo, K. Kurita, K. Kusaka, T. Minemura, T. Motobayashi, T. Nakabayashi, T. Nakamura, T. Nakao, M. Niikura, T. Okumura, T.K. Ohnishi, H.J. Ong, H. Sakurai, S. Shimoura, R. Sugo, D. Suzuki, M.K. Suzuki, M. Tamaki, K. Tanaka, Y. Togano, K. Yamada "Collectivity of neutron-rich Ti isotopes", Phys. Rev. C **88** (2013) 024326.

13. S. Michimasa, M. Takaki, M. Dozono, S. Go, H. Baba, E. Ideguchi, K. Kisamori, H. Matsubara, H. Miya, S. Ota, H. Sakai, S. Shimoura, A. Stolz, T.L. Tang, H. Tokieda, T. Uesaka, R.G.T. Zegers, " Development of CVD diamond detector for time-of-flight measurements", Nucl. Instru Meth. B **317** (2013) 710–713.

14. H. Miya, S. Ota, T. Fujii, S. Kawase, Y. Kubota, C.S. Lee, H. Matsubara, K. Miki, A. Saito, S. Michimasa, T. Uesaka, H. Sakai, S. Shimoura, "Development of low-pressure multi-wire drift chambers for high-resolution spectroscopy with radioactive isotope beams", Nucl. Instru Meth. B **317** (2013) 701–704.

15. J.W. Hwang, Y. Satou, T. Nakamura, Y. Kondo, N. Matsui, Y. Hashimoto, T. Nakabayashi, T. Okumura, M. Shinohara, N. Fukuda, T. Sugimoto, H. Otsu, Y. Togano, T. Motobayashi, H. Sakurai, Y. Yanagisawa, N. Aoi, S. Takeuchi, T. Gomi, M. Ishihara, S. Kawai, H.J. Ong, T.K. Onishi, S. Shimoura, M. Tamaki, T. Kobayashi, Y. Matsuda, N. Endo, M. Kitayama, "Discovery of the First 2- State in 16C via Neutron Knockout Reaction", Few-Body Syst (2013) **54** 1469-472.

16. H. Muto, Y. Ohshiro, S. Yamaka, S. Watanabe, M. Oyaizu, S. Kubono, H. Yamaguchi, M. Kase, T. Hattori, S. Shimoura "Grating monochromator for electron cyclotron resonance ion source operation", Rev. Sci. Instrum. **84** (2013) 073304.

17. S. Michimasa, M. Takaki, Y. Sasamoto, M. Dozono, T. Nishi, T. Kawabata, S. Ota, H. Baba, T. Baba, T. Fujii, S. Go, S. Kawase, Y. Kikuchi, K. Kisamori, M. Kobayashi, Y. Kubota, C.S. Lee, H. Matsubara, K. Miki, H. Miya, S. Noji, H. Tokieda, M. Tsumura, K. Yako, R. Yokoyama, H. Takeda, Y. Yanagisawa, T. Kubo, N. Inabe, N. Fukuda, D. Kameda, H. Suzuki, Y. Shimizu, H.Sato, T. Ichihara, A. Stolz, R.G.T. Zegers, H. Sakai, T. Uesaka, S. Shimoura, "SHARAQ spectrometer for high-resolution studies for RI-induced reactions", Nucl. Instru Meth. B **317** (2013) 305–310.

18. T. Otsuka, S. Shimoura, Y. Onda, A. Shinohara, T. Shibata, "Soil radioactivity of ^{131}I measured by Pilot Investigation", Radioisotopes (published by The Japan Radioisotope Association), **62**, 752 (2013).

19. S. Shimoura, "Activities of Center for Nuclear Study (CNS), The University of Tokyo", Radioisotopes (published by The Japan Radioisotope Association), **62** 810–816 (2013).

20. P. Doornenbal, H. Scheit, S. Takeuchi, N. Aoi, K. Li, M. Matsushita, D. Steppenbeck, H. Wang, H. Baba, H. Crawford, C.R. Hoffman, R. Hughes, E. Ideguchi, N. Kobayashi, Y. Kondo, J. Lee, S. Michimasa, T. Motobayashi, H. Sakurai, M. Takechi, Y. Togano, R. Winkler, K. Yoneda, "In-Beam γ-Ray Spectroscopy of ^{34,36,38}Mg: Merging the N=20 and N=28 Shell Quenching", Phys. Rev. Lett. **111**, 212502 (2013).

21. D. Steppenbeck, S. Takeuchi, N. Aoi, P. Doornenbal, J. Lee, M. Matsushita, H. Wang, H. Baba, N. Fukuda, S. Go, M. Honma, K. Matsui, S. Michimasa, T. Motobayashi, D. Nishimura, T. Otsuka, H. Sakurai, Y. Shiga, P.-A. Soderstrom, T. Sumikama, H. Suzuki, R. Taniuchi, Y. Utsuno, J.J. Valiente-Dobon, K. Yoneda "Investigating the strength of the N = 34 subshell closure in ^{54}Ca", J. Phys. Conf. Ser. **445**, 012012 (2013).

22. D. Steppenbeck, S. Takeuchi, N. Aoi, P. Doornenbal, M. Matsushita, H. Wang, H. Baba, N. Fukuda, S. Go, M. Honma, J. Lee, K. Matsui, S. Michimasa, T. Motobayashi, D. Nishimura, T. Otsuka, H. Sakurai, Y. Shiga, P.-A. Soderstrom, T. Sumikama, H. Suzuki, R. Taniuchi, Y. Utsuno, J.J. Valiente-Dobon, K. Yoneda, "Evidence for a new nuclear 'magic number' from the level structure of ^{54}Ca", Nature (London) **502**, 207 (2013).

23. A. Adare, *et al.* (PHENIX Collaboration), "Azimuthal anisotropy of π^0 and eta mesons in Au+Au collisions at $\sqrt{s_{NN}}$=200 GeV", Phys. Rev. C **88**, 064910 (2013).

24. B.B. Abelev, *et al.* (ALICE Collaboration), "K_S^0 and Λ production in Pb-Pb collisions at $\sqrt{s_{NN}}$ = 2.76 TeV", Phys. Rev. Lett. **111**, no. 22, 222301 (2013).

25. B.B. Abelev, *et al.* (ALICE Collaboration), "Long-range angular correlations of pi, K and p in p–Pb collisions at $\sqrt{s_{NN}}$ = 5.02 TeV", Phys. Lett. B **726**, 164 (2013).

26. AB.B. Abelev, *et al.* (ALICE Collaboration), "Multiplicity dependence of the average transverse momentum in pp, p-Pb, and Pb-Pb collisions at the LHC", Phys. Lett. B **727**, 371 (2013).

27. B.B. Abelev, *et al.* (ALICE Collaboration), "Multiplicity dependence of two-particle azimuthal correlations in pp collisions at the LHC", JHEP **1309**, 049 (2013).

28. B.B. Abelev,*et al.* (ALICE Collaboration), "Energy Dependence of the Transverse Momentum Distributions of Charged Particles in pp Collisions Measured by ALICE", Eur. Phys. J. C **73**, 2662 (2013).

29. B.B. Abelev, *et al.* (ALICE Collaboration), "Directed Flow of Charged Particles at Midrapidity Relative to the Spectator Plane in Pb-Pb Collisions at $\sqrt{s_{NN}}$=2.76 TeV", Phys. Rev. Lett. **111**, no. 23, 232302 (2013).

30. E. Abbas, *et al.* (ALICE Collaboration), "Performance of the ALICE VZERO system", JINST **8**, P10016 (2013).

31. A. Adare, *et al.* (PHENIX Collaboration), "Nuclear Modification of ψ', χ_c, and J/ψ Production in d+Au Collisions at $\sqrt{s_{NN}}$=200GeV", Phys. Rev. Lett. **111**, no. 20, 202301 (2013).

32. B. Abelev, *et al.* (ALICE Collaboration), "D meson elliptic flow in non-central Pb-Pb collisions at $\sqrt{s_{NN}} = 2.76$TeV", Phys. Rev. Lett. **111**, 102301 (2013).

33. E. Abbas, *et al.* (ALICE Collaboration), "Mid-rapidity anti-baryon to baryon ratios in pp collisions at $\sqrt{s} = 0.9$, 2.76 and 7 TeV measured by ALICE", Eur. Phys. J. C **73**, 2496 (2013).

34. E. Abbas, *et al.* (ALICE Collaboration), "Charmonium and e^+e^- pair photoproduction at mid-rapidity in ultra-peripheral Pb-Pb collisions at $\sqrt{s_{NN}} = 2.76$ TeV", Eur. Phys. J. C **73**, 2617 (2013).

35. A. Adare, *et al.* (PHENIX Collaboration), "Spectra and ratios of identified particles in Au+Au and d+Au collisions at $\sqrt{s_{NN}} = 200$ GeV", Phys. Rev. C **88**, no. 2, 024906 (2013).

36. E. Abbas, *et al.* (ALICE Collaboration] "Centrality dependence of the pseudorapidity density distribution for charged particles in Pb-Pb collisions at $\sqrt{s_{NN}} = 2.76$ TeV", Phys. Lett. B **726**, 610 (2013).

37. E. Abbas, *et al.* (ALICE Collaboration), "J/ψ Elliptic Flow in Pb-Pb Collisions at $\sqrt{s_{NN}} = 2.76$ TeV", Phys. Rev. Lett. **111**, 162301 (2013).

38. A. Adare, *et al.* (PHENIX Collaboration), "Quadrupole Anisotropy in Dihadron Azimuthal Correlations in Central d+Au Collisions at $\sqrt{s_{NN}}$=200 GeV", Phys. Rev. Lett. **111**, no. 21, 212301 (2013).

39. B. Abelev, *et al.* (ALICE Collaboration), "Centrality dependence of π, K, p production in Pb-Pb collisions at $\sqrt{s_{NN}} = 2.76$ TeV", Phys. Rev. C **88**, no. 4, 044910 (2013).

40. B. Abelev, *et al.* (ALICE Collaboration), "Centrality determination of Pb-Pb collisions at $\sqrt{s_{NN}} = 2.76$ TeV with ALICE", Phys. Rev. C **88**, no. 4, 044909 (2013).

41. B. Abelev, *et al.* (ALICE Collaboration), "Charge correlations using the balance function in Pb-Pb collisions at $\sqrt{s_{NN}} = 2.76$ TeV", Phys. Lett. B **723**, 267 (2013).

42. B. Abelev, *et al.* (ALICE Collaboration), "Measurement of the inclusive differential jet cross section in pp collisions at $\sqrt{s} = 2.76$ TeV", Phys. Lett. B **722**, 262 (2013).

43. Y. Utsuno, N. Shimizu, T. Otsuka, T. Abe, "Efficient computation of Hamiltonian matrix elements between non-orthogonal Slater determinants", Comp. Phys. Comm. **184**, (2013) 102.

44. J. Papuga, M.L. Bissell, K. Kreim, K. Blaum, B.A. Brown, M. De Rydt, R.F. Garcia Ruiz, H. Heylen, M. Kowalska, R. Neugart, G. Neyens, W. Nortershauser, T. Otsuka, M.M. Rajabali, R. Sanchez, Y. Utsuno, and D.T. Yordanov, "Spins and Magnetic Moments of 49K and 51K: Establishing the 1/2+ and 3/2+ Level Ordering Beyond N=28", Physical Review Letters **110**, 172503 (2013).

45. Y. Tsunoda, T. Otsuka, N. Shimizu, M. Honma, and Y. Utsuno, "Novel shape evolution in exotic Ni isotopes and configuration-dependent shell structure", Physical Review C **89** (2014) 031301(R).

46. T. Otsuka, "Large-scale emergency measurement of environment radiation by nuclear physicists and what we can learn from it", Radioisotopes (published by The Japan Radioisotope Association), **62**, 746 (2013).

B. Proceedings

1. N. Duy, S. Kubono, H. Yamaguchi, D. Kahl, Y. Wakabayashi, T. Teranishi, N. Iwasa, Y. Kwon, L. Khiem, Y. Kim, J. Song, J. Hu, Y. Ayyad, "Low-energy radioactive ion beam production of ^{22}Mg", Nuclear Instruments and Methods in Physics Research Section A **723** 99–101 (2013) .

2. S. Kubono, Dam N. Binh, S. Hayakawa, T. Hashimoto, D.M. Kahl, H. Yamaguchi, Y. Wakabayashi, T. Teranishi, N. Iwasa, T. Komatsubara, S. Kato, A. Chen, S. Cherubini, S. H. Choi, I.S. Hahn, J.J. He, Le H. Khiem, C.S. Lee, Y.K. Kwon, S. Wanajo and H.-T. Janka, "Experimental challenge to nucleosynthesis in core-collapse supernovae - Very early epoch of type II SNe -", AIP Conf. Proc. **1533** 70 (2013).

3. Y. Ohshiro, S. Yamaka, S. Watanabe, K. Kobayashi, Y. Kotaka, M. Nishimura, M. Kase, H. Muto, H. Yamaguchi, S. Shimoura, "Production of beams from solid materials at center for nuclear study electron cyclotron resonance ion source", Rev. of Sci. Instrum. **85** 02A912 (2013).

4. H. Yamaguchi, D. Kahl, T. Nakao, Y. Wakabayashi, S. Kubono, T. Hashimoto, S. Hayakawa, T. Kawabata, N. Iwasa, T. Teranishi, Y.K. Kwon, D.N. Binh, L.H. Khiem and N.N. Duy, "Recent developments and research projects at the low-energy RI beam facility CRIB", Nucl. Instr. and Meth. B, **317** 664–667 (2013).

5. M. Gulino, S. Cherubini, G.G. Rapisarda, S. Kubono, L. Lamia, M. La Cognata, H. Yamaguchi, S. Hayakawa, Y. Wakabayashi, N. Iwasa, S. Kato, H. Komatsubara, T. Teranishi, A. Coc, N. De Séréville, F. Hammache, C. Spitaleri, "Trojan Horse method and radioactive ion beams: study of 18F(p,alpha)15O reaction at astrophysical energies", 11th International Conference on Nucleus-Nucleus Collisions (NN2012), Journal of Physics: Conference Series **420** 012149 (2013).

6. H. Yamaguchi, D. Kahl, T. Nakao, Y. Wakabayashi, S. Kubono, T. Hashimoto, S. Hayakawa, T. Kawabata, N. Iwasa, T. Teranishi, Y.K. Kwon, P.S. Lee, D.N. Binh, L.H. Khiem, and N.N. Duy, "Studies on alpha-induced astrophysical reactions using the low-energy RI beam separator CRIB" EPJ Web of Conferences **66**, 07027 (2014).

7. M. Kobayashi, K. Yako, S. Shimoura, M. Dozono, S. Kawase, K. Kisamori, Y. Kubota, C.S. Lee, S. Michimasa, H. Miya, S. Ota, H. Sakai, M. Sasano, M. Takaki, "Measurement of the $^8\text{He}(p,n)^8\text{Li}$ reaction at intermediate energy in inverse kinematics", Proceedings of the 12th Asia Pacific Physics Conference (APPC12), Jul. 14–19, 2013, Makuhari, Japan, JPS Conf. Proc. 1, 013034 (2014)

8. Y. Kubota, M. Sasano, T. Uesaka, M. Dozono, M. Itoh, S. Kawase, M. Kobayashi, C.S. Lee, H. Matsubara, H. Miya, S. Ota, K. Sekiguchi, T. Taguchi, T. L. Tang, H. Tokieda, and T. Wakui, "A new neutron detector with a high position resolution for the study of the (p,pn) reaction on rare isotopes", EPJ Web of Conferences Vol. 66, No. 11022 (2014).

9. M. Matsushita, S. Takeuchi, N. Aoi, P. Doornenbal, J. Lee, K. Li, T. Motobayashi, H. Scheit, D. Steppenbeck, H. Wang, H. Baba, D. Bazin, L. Ceres, H. Crawford, P. Fallon, R. Gernhauser, J. Gibelin, S. Go, S. Grevy, C. Hinke, C. R. Hoffman, R. Hughes, E. Ideguchi, K. Ieki, D. Jenkins, N. Kobayashi, Y. Kondo, R. Kr   ken, T. Le Bleis, G. Lee, A. Matta, S. Michimasa, T. Nakamura, S. Ota, M. Petri, T. Sako, H. Sakurai, S. Shimoura, K. Steiger, K. Takahashi, M. Takechi, Y. Togano, R. Winkler, K. Yoneda (Oral), "In-beam ?-ray spectroscopy of $^{38,40,42}\text{Si}$", EPJ Web of Conferences Vol. 66, No. 02070 (2014).

10. N. Shimizu, T. Otsuka, Y. Utsuno, T. Mizusaki, M. Honma, T. Abe, "History and future perspectives of the Monte Carlo shell model -from Alphleet to K computer-", J. Phys.: Conf. Ser. **445** (2013) 012004.

11. T. Yoshida, N. Shimizu, T. Abe, T. Otsuka, " Density profiles of the intrinsic frame of light nuclei obtained from Monte Carlo shell model calculation", J. Phys.: Conf. Ser. **445** (2013) 012038.

12. Y. Tsunoda, T. Otsuka, N. Shimizu, M. Honma, Y. Utsuno, " Study of nuclei around Z = 28 by large-scale shell model calculations", J. Phys.: Conf. Ser. **445** (2013) 012028.

C. Theses

1. M. Kobayashi: "Spin-isospin response of neutron-rich nucleus ^{8}He via (p,n) reaction in inverse kinematics", Master Thesis, the University of Tokyo, March 2014.

2. K. Terasaki: "Research and Development of COBRA GEM for Ion Back Flow Suppression", Master Thesis, the University of Tokyo, March 2014.

3. S. Go: "Superdeformation of ^{35}S", Doctor Thesis, the University of Tokyo, March 2014.

4. R. Akimoto: "'Measurement of Charms and Bottoms with Semi-leptonic Decay Modes in $p+p$ Collisions at $\sqrt{s} = $ 200 GeV', Doctor Thesis, the University of Tokyo, March 2014.

D. Other Publications

1.   (   ), "LHC-ALICE   ",   /pp.6-10, 2013-06

2.   ,"   :   ", vol.58-1 (2013) 96-108.

Talks and Presentations

A. Conferences

1. H. Yamaguchi (oral,invited), "Nuclear astrophysics and structure studies using low-energy RI beams", Pioneering Symposium: "The Third Generation of RIB Facilities" in Korean Physical Society Meeting, Apr 24–26, 2013, Daejeon, Korea.

2. H. Yamaguchi (oral), "Studies on nuclear reaction and structure using low-energy RI beams at CRIB", Workshop on the INFN-RIKEN collaboration on nuclear physics activities May 17, 2013, Istituto Italiano di Cultura di Tokyo, Sala "G Puccini" 2-1-30 Kudan Minami, Chiyoda-ku, Tokyo

3. H. Yamaguchi (oral), "Studies on alpha-induced astrophysical reactions using the low-energy RI beam separator CRIB" The 25th International Nuclear Physics Conference (INPC 2013), June 2–7 2013, Florence, Italy.

4. H. Yamaguchi (oral), "Recent activities at CRIB - nuclear astrophysics, reaction, and structure studies with low-energy RI beam" RIBF Users Meeting 2013, June 26–27, 2013, RIKEN, Wako, Saitama, Japan.

5. H. Yamaguchi (oral), "Studying alpha-cluster structure using low-energy RI beam", RCNP Workshop; Clustering phenomena in multi nucleon and hyperon system, Jul 26–27 2013, Kansai Gakuin University, Yokohama, Japan.

6. H. Yamaguchi (oral), "Studies on astrophysical reactions using low-energy RI beam at CRIB", SKKU Symposium on Astrophysics and Cosmology: from Particle to Universe, Oct. 4 and December 2-4, 2013, SKKU Natural Sciences Campus, Suwon, Korea.

7. H. Yamaguchi (oral), "Recent status of the low-enrgy RI beam separator CRIB", 1st RIKEN-RISP Joint Workshop, Nov. 7–8, 2013, IBS, Daejeon, Korea

8. H. Yamaguchi (oral), "Alpha resonant scattering for astrophysical reaction studies", The 12th International Symposium on Origin of Matter and Evolution of the Galaxies (OMEG12), Nov 18–22, 2013, Epochal Tsukuba, Tsukuba, Ibaraki, Japan.

9. H. Yamaguchi (oral), "The low-energy RI beam facility CRIB for astrophysics and nuclear structure studies", JUSTIPEN-JUSEIPEN Workshop, Dec. 9–12, 2013, RIKEN, Wako, Saitama, Japan

10. H. Yamaguchi (oral), "Recent status and technical aspects of RI Beam separator CRIB", Nuclear physics seminar at RISP, Feb. 28, 2014, IBS, Daejeon, Korea.

11. M. Matsushita, S. Takeuchi, N. Aoi, P. Doornenbal, J. Lee, K. Li, T. Motobayashi, H. Scheit, D. Steppenbeck, H. Wang, H. Baba, D. Bazin, L. Ceres, H. Crawford, P. Fallon, R. Gernhauser, J. Gibelin,S. Go,S. Grevy,C. Hinke, C. R. Hoffman,R. Hughes,E. Ideguchi,K. Ieki,D. Jenkins, N. Kobayashi, Y. Kondo, R. Kruken, T. Le Bleis, G. Lee, A. Matta, S. Michimasa, T. Nakamura, S. Ota, M. Petri, T. Sako, H. Sakurai, S. Shimoura, K. Steiger, K. Takahashi, M. Takechi, Y. Togano, R. Winkler, K. Yoneda (Oral), "In-beam γ-ray spectroscopy of ^{38,40,42}Si", International Nuclear Physics Conference (INPC2013), June 2-7, 2013, Firenze, Italy

12. S.Michimasa, Y. Yanagisawa, K. Inafuku, N. Aoi, Z. Elekes, Zs. Fulop, Y. Ichikawa, N. Iwasa, K. Kurita, M. Kurokawa, T. Machida, T. Motobayashi, T. Nakamura, T. Nakabayashi, M. Notani, H.J. Ong, T. K. Onishi, H. Otsu, H. Sakurai, M. Shinohara, T. Sumikama, S. Takeuchi, K. Tanaka, Y. Togano, K. Yamada, M. Yamaguchi, K. Yoneda (Poster), "Proton inelastic scattering study on ^{30}Ne and ^{34,36}Mg isotopes" International Nuclear Physics Conference (INPC2013), June 2-7, 2013, Firenze, Italy.

13. S. Go, D. Kameda, T. Kubo, N. Inabe, N. Fukuda, R. Yokoyama, T. Fujii, E. Ideguchi, H. Takeda, H. Suzuki, K. Yoshida, K. Kusaka, Y. Yanagisawa, M. Ohtake, H. Sato, Y. Shimizu, H. Baba, M. Kurokawa, D. Nishimura, T. Ohnishi, N. Iwasa, A. Chiba, T. Yamada, H. Nishibata, K. Ieki, D. Murai, S. Momota, Y. Sato, J. Hwang, S. Kim, O.B. Tarasov, D.J. Morrissey, B.M. Sherrill, G. Simpson (Poster), "Observation of new isomers in N=100 neutron-rich rare-earth nuclei" International Nuclear Physics Conference (INPC2013), June 2-7, 2013, Firenze, Italy

14. Y. Kubota, M. Sasano, T. Uesaka, M. Dozono, M. Itoh, S. Kawase, M. Kobayashi, C.S. Lee, H. Matsubara, H. Miya, S. Ota, K. Sekiguchi, T. Taguchi, T. L. Tang, H. Tokieda, and T. Wakui (Poster), "A new neutron detector with a high position resolution for the study of the (p,pn) reaction on rare isotopes", The 25th International Nuclear Physics Conference (INPC2013), July 2-7, 2013, Florence, Italy

15. S. Shimoura (Oral), "Experimental opportunities for the high-resolution spectroscopy using GRAPE and/or SHARAQ", Sunflower Workshop, Sept. 10-11, 2013, Darmstadt, Germany

16. K. Yako (Invited), "(p,n) measurements in inverse kinematics at SHARAQ-WINDS", JUSTIPEN-JUSEIPEN Workshop, Dec. 9–12, 2013, RIKEN.

17. S. Shimoura (Invited), "Energy degrading project for RI beams in CNS", JUSTIPEN-JUSEIPEN Workshop, Dec. 9-12, 2013, Wako

18. S. Shimoura (Invited), "Energy degrading project of RI beams in CNS – OEDO project", Workshop on Physics Opportunities using Compton Supressed Ge Clover Array (CAGRA13), Dec. 16-17, 2013, Osaka University

19. S. Michimasa (Oral), "Physics Oppotunity via transfer reaction measurements with gamma-ray detectors" Workshop on Physics Research with Grand Raiden Forward-mode Beam Line, Nov. 28-29, 2013, RCNP, Osaka University.

20. M. Dozono (Oral), "Research for 0^- states via $(^{16}O,^{16}N\gamma)$ reaction" Workshop on Physics Research with Grand Raiden Forward-mode Beam Line, Nov. 28-29, 2013, RCNP, Osaka University.

21. M. Takaki (Oral), "Research for double GT states via $(^{12}C,^{12}Be\gamma)$ reaction" Workshop on Physics Research with Grand Raiden Forward-mode Beam Line, Nov. 28-29, 2013, RCNP, Osaka University.

22. S. Shimoura (Invited), "OEDO project"   , Mar. 6–8, RIKEN

23. M. Kobayashi, K. Yako, S. Shimoura, M. Dozono, S. Kawase, K. Kisamori, Y. Kubota, C.S. Lee, S. Michimasa, H. Miya, S. Ota, H. Sakai, M. Sasano, M. Takaki (Oral), "Measurement of the ^{8}He$(p,n)^8$Li reaction at intermediate energy in inverse kinematics", APPC12, Jul. 14–19, 2013, Makuhari, Japan

24. K. Yako, "Recent physics programs at SHARAQ spectrometer", RIBF Users Meeting 2013, Jun. 26–27, 2013, RIKEN.

25. C.S. Lee, S. Ota, H. Tokieda, R. Kojima, Y. Watanabe, and T. Uesaka "Properties of Thick GEM in Low-pressure Deuterium" (Oral) Micro-Pattern Gaseous Detector (MPGD) 2013, Jul.1–4, 2013, Zaragoza, Spain.

26. S. Go, E. Ideguchi, M. Kobayashi, R. Yokoyama, K. Kisamori, S. Michimasa, S. Shimoura, M. Niikura, A. Yagi, H. Nishibata, I. Matea, D. Verney, F. Azaiez, M. Koizumi, Y. Toh, A. Kimura, H. Harada, K. Furukata, S. Nakamura, F. Kitatani, Y. Hatsukawa, M. Ohshima (Oral), "Study of high spin states in ^{35,36}S" 2nd Workshop on the physics at the Tandem-ALTO facility, May 14–15, 2013, Orsay, France

27. S. Go, E. Ideguchi, R. Yokoyama, M. Kobayashi, K. Kisamori, S. Michimasa, S. Shimoura, M. Niikura, A. Yagi, H. Nishibata, I. Matea, D. Verney, F. Azaiez, M. Koizumi, Y. Toh, A. Kimura, H. Harada, K. Furukata, S. Nakamura, F. Kitatani, Y. Hatsukawa (Oral), "Study of high spin states in ^{35}S" French-Japanese Symposium on Nuclear Structure Problems, Sep. 30–Oct. 3, 2013, Paris, France

28. H. Hamagaki (invited), "ALICE Experiment", at PHENIX Workshop on Physics Prospects with Detector and Accelerator Upgrades; from 29 July 2013 to 2 August 2013 at RIKEN

29. T. Gunji (invited), "ALICE Physics Perspectives and GEM-TPC upgrade", Heavy Ion Meeting, Nov 2, 2013, 3 Inha University, Korea

30. T. Gunji (invited), "Probing the hot and dense QCD medium with hard probes at RHIC and LHC", Pioneering Symposium for heavy ion collisions, in Korean Physical Society Meeting, Oct 30, 2013, Pusan, Korea.

31. T. Gunji (invited), "LHC-ALICE   ", Heavy Ion Pub, May 31, 2013, Osaka, Japan

32. K. Terasaki for the ALICE Collaboration (poster), "Study of Ion Back Flow suppression with thick COBRA GEM", The 3rd International Conference on Micro Pattern Gaseous Detectors (MPGD203), July 1-4, 2013, Zaragoza, Spain.

33. Y. Yamaguchi for the ALICE Collaboration (oral), "ALICE   GEM-TPC   ",   10   Micro-Pattern Gas Detector   , Dec. 12–13, 2013, Kyoto, Japan

34. K. Terasaki, for the ALICE Collaboration (oral), "Thick COBRA GEM   ",   10   Micro-Pattern Gas Detector   , Dec. 12–13, 2013, Kyoto, Japan

35. K. Yukawa (oral), "   ",   10   Micro-Pattern Gas Detector   , Dec. 12–13, 2013, Kyoto, Japan

36. H. Hamagaki (invited), "Study of hadron properties in QCD medium using the high-energy heavy-ion collisions", workshop on Hadrons in Nucleus, Oct. 31 Nov. 2, 2013, Kyoto, Japan

37. K. Terasaki, (oral), "R&D of Thick COBRA GEM for the application of the GEM-based TPC", 2013 IEEE Nuclear Science Symposium and Medical Imaging Conference (2013 NSS/MIC), Oct 27 Nov 02, 2013, Seoul, Korea

38. Y. Sekiguchi (poster), "Basic performance of SoI pixel detector for radiation monitor", 2013 IEEE Nuclear Science Symposium and Medical Imaging Conference (2013 NSS/MIC), Oct 27 Nov 02, 2013, Seoul, Korea

39. Y. Yamaguchi for the PHENIX Collaboration (oral), "A Search for Beyond the Standard Model Particles with the PHENIX detector at RHIC", APS Division of Nuclear Physics, Fall Meeting, October 23-26, 2013, New- port News, VA,

40. T. Yoshida, N. Shimizu, T. Abe and T. Otsuka (oral), "Density of ligh nuclei obtained from Monte Carlo shell model", HPCI Strategic Program Field 5 Symposium, Fujisoft Akiba Plaza, Tokyo, Japan, March 5-6, 2013.

41. S. Ebata, T. Nakatsukasa, T. Inakura (oral), "Density functional approaches to nuclear dynamics", HPCI Strategic Program Field 5 Symposium, Fujisoft Akiba Plaza, Tokyo, Japan, March 5-6, 2013.

42. T. Otsuka (oral), "Ultra large-scale Simulations of quantum many-body systems for nuclear properties and its applications", HPCI Strategic Program Field 5 Symposium, Fujisoft Akiba Plaza, Tokyo, Japan, March 5-6, 2013.

43. Y. Iwata, T. Otsuka and S. Heinz (oral), "Fission dynamics of superheavy compound nuclei", Fission 2013, Caen, France, May 2013.

44. Y. Utsuno (invited), T. Otsuka, N. Shimizu, M. Honma, T. Mizusakia, Y. Tsunoda and T. Abe (oral), Recent shell-model results for exotic nuclei 25th International Nuclear Physics Conference (INPC 2013), Florence, Italy, June 3-7, 2013.

45. Y. Iwata, T. Otsuka and S. Heinz, "Fission dynamics of superheavy compound nucle", International Nuclear Physics Conference 2013 (INPC2013), Florence, Italy, June 3-7, 2013.

46. Y. Iwata, T. Otsuka and S. Heinz, "Fission dynamics of superheavy compound nuclei", The 12th Asia Pacific Physics Conference of AAPPS (APPC 12), Chiba, Japan, July 14-19, 2013.

47. T. Yoshida, N. Shimizu, T. Abe and T.Otsuka (poster), "Density profiles of light nuclei in Monte Carlo shell-model calculation", International Nuclear Physics Conference 2013 (INPC2013), Florence, Italy, June 3-7, 2013.

48. T. Yoshida, N. Shimizu, T. Abe and T.Otsuka (poster), "Density profiles of light nuclei in Monte Carlo shell-model calculation", The 12th Asia Pacific Physics Conference, Chiba, Japan, July 14-19, 2013.

49. Y. Iwata, "Fission dynamics of superheavy compound nuclei", The 12th Asia Pacific Physics Conference, Chiba, Japan, July 14-19, 2013.

50. T. Otsuka (invited), "Monte Carlo Shell Model and shape phase transitions in exotic nuclei", Int. Conf. on Nuclear Theory in the Supercomputing Era - 2013, Ames, USA, May 13-17, 2013.

51. T. Otsuka (invited), "Fukushima Nuclear Power Plant Accident and Nuclear Physicists", International Nuclear Physics Conference 2013 (INPC2013), Florence, Italy, June 3-7, 2013.

52. T. Otsuka (invited), "Driving forces of shell evolution and shapes of exotic nuclei", Gordon Conference on Nuclear Chemistry, Colby-Sawyer College, New London, USA, June 9-14, 2013.

53. T. Otsuka (invited), "Structure Evolutions in Exotic Nuclei", 12th Asia Pacific Physics Conference, Makuhari, Chiba, Japan, July 15-19, 2013.

54. Y. Iwata (invited), "The TDDFT calculations for low-energy heavy-ion collisions", French-Japanese Symposium on Nuclear Structure Problems, Paris, France, September 30, 2013.

55. T. Otsuka (invited), "Perspectives beyond the Shell Evolution", French-Japanese Symposium on Nuclear Structure Problems -Organized in the framework of FJNSP LIA-, CNRS, Paris, September 30-Oct. 3, 2013.

56. T. Otsuka (invited), "Structure Evolutions in Exotic Nuclei", Mini-Symposium on Experiment and Theory for Nuclei Close to the Driplines, 2013 Fall Meeting of the APS DNP, Newport News, USA, October 23-26, 2013.

57. T. Otsuka (invited), "Perspectives of physics of exotic nuclei beyond the shell evolution", First African Symposium on Exotic Nuclei (IASEN-2013), Cape Town, South Africa, December 2-6, 2013.

58. Y. Utsuno (invited), "Shell evolution along the Sn isotopes", 10th ASRC International Workshop "Nuclear Fission and Decay of Exotic Nuclei", JAEA Nuclear Science Research Institute, Tokai, Japan, March 21-22, 2013.

59. S. Ebata and T. Nakatsukasa (oral), "Pairing effects in fusion phenomena utilizing a time-dependent mean field theory", 10th ASRC International Workshop "Nuclear Fission and Decay of Exotic Nuclei", JAEA Nuclear Science Research Institute, Tokai, Japan, March 21-22, 2013.

60. Y. Iwata, T. Otsuka, T. Otsuka and S. Heinz (oral), "Fission dynamics of superheavy compound nuclei", The 10th ASRC International Workshop "Nuclear Fission and Decay of Exotic Nuclei", JAEA Nuclear Science Research Institute, Tokai, Japan, March 21-22, 2013.

61. Y. Utsuno, T. Otsuka, N. Shimizu, T. Mizusaki and M. Honma, "Tensor-force driven shell evolution studied with large-scale shell-model calculations", RCNP Workshop on the Importance of Tensor Interactions in Nuclear and Hadron Structures, Osaka, Japan, July, 2013.

62. T. Yoshida, "Density distributions of Be isotopes based on Monte Carlo shell model", RCNP , Kanagawa, Japan, July 26-27, 2013.

63. Y. Iwata (invited), "TDDFT calculations for the symmetry energy research", RIBF-ULIC Mini Workshop 027 "Nuclear symmetry-energy and nucleus-nucleus collision simulation", Saitama, Japan, July 2-4, 2013.

64. Y. Iwata, T. Otsuka, T. Otsuka and S. Heinz (oral), "Fission dynamics of superheavy compound nuclei", Fission 2013, Caen, France "Fifth International Workshop on Nuclear Fission and Fission Product Spectroscopy", May 28-31, 2013.

65. Y. Utsuno (invited), "Shell-model approach to shape coexistence in light nuclei", IOP Workshop "Shape Coexistence Across the Chart of Nuclides, York, UK, April, 2013.

66. T. Otsuka (invited), "Tensor force and shell structure - A personal history - ", RCNP Workshop on the Importance of Tensor Interactions in Nuclei and Hadron structure, RCNP, Osaka, Japan, July 11-12, 2013.

67. N. Shimizu, "Large-scale shell-model calculations and Monte Carlo shell model", JUSTIPEN-JUSEIPEN Workshop, Saitama, Japan, December 9-12, 2013.

68. T. Otsuka, "ICN status", JUSTIPEN-JUSEIPEN Workshop, Saitama, Japan, December 9-12, 2013.

69. Y. Iwata (invited), "Charge equilibration and its application to symmetry energy research", ECT* workshop "Advances in time-dependent methods for quantum many-body systems", Trento, Italy, October, 2013.

70. Y. Iwata (invited), "A study of nuclear reaction mecha- nism based on TDDFT calculations",   3   HPCI   2   5   , Institute for Molecular Science, Aichi, Japan, November 2013.

71. T. Otsuka (invited), "Shell model calculations with more than one shell", INT workshop "Computational and Theoretical Advances for Exotic Isotopes in the Medium Mass Region", INT, Seattle, USA, March 25-Aprl 19, 2013.

72. T. Otsuka (invited), "Shape coexistence and shell evolution in exotic Ni isotopes", International Workshop on "Shape Coexistence Across the Chart of the Nuclides", Kings Manor, York, UK, April 15-16, 2013.

73. T. Otsuka (invited), "Shapes of medium-mass exotic nuclei and MCSM calculations", ECT*/HIC for FAIR workshop "From Few-Nucleon Forces to Many-Nucleon Structure", ECT*, Trento, Italy, June 10-14, 2013.

B. JPS Meetings

1. M. Kobayashi, K. Yako, S. Shimoura, M. Dozono, S. Kawase, K. Kisamori, Y. Kubota, C.S. Lee, S. Michimasa, H. Miya, S. Ota, H. Sakai, M. Sasano, M. Takaki, "Spin-isospin response of a neutron rich nucleus ^{8}He via (p,n) reactions in inverse kinematics", at the JPS Fall meeting, Sep. 20–23, 2013, Kochi University, Japan

2. H. Miya, S. Shimoura, K. Kisamori, H. Baba, T. Baba, M. Dozono, N. Fukuda, T. Fujii, S. Go, E. Ideguchi N. Inabe, M. Ito, D. Kameda, T. Kawabata, S. Kawase, T. Kubo, Y. Kubota, M. Kobayashi, Y. Konodo, C.S. Lee, Y. Maeda, H. Matsubara, K. Miki, S. Michimasa, T. Nishi, M. Nishimura, S. Ota, S. Sakaguchi, H. Sakai, M. Sasano, H. Sato, Y. Shimizu, H. Suzuki, M. Takaki, A. Tamii, H. Takeda, S. Takeuchi, H. Tokieda, M. Tsumura, T. Uesaka, Y. Yanagisawa, K. Yako, R. Yokoyama, K. Yoshida, M. Assie, D. Beaumel, H. Fariouz, A. Stolz, "Study of spin-isospin response via exothermic charge exchange (^{8}He, ^{8}Liγ) for ^{4}He nuclei" at the JPS Fall meeting, Sep. 20–23, 2013, Kochi University, Japan

3. K. Kisamori, S. Shimoura, H. Miya, H. Baba, T. Baba, M. Dozono, N. Fukuda, T. Fujii, S. Go, E. Ideguchi N. Inabe, M. Ito, D. Kameda, T. Kawabata, S. Kawase, T. Kubo, Y. Kubota, M. Kobayashi, Y. Konodo, C.S. Lee, Y. Maeda, H. Matsubara, K. Miki, S. Michimasa, T. Nishi, M. Nishimura, S. Ota, S. Sakaguchi, H. Sakai, M. Sasano, H. Sato, Y. Shimizu, H. Suzuki, M. Takaki, A. Tamii, H. Takeda, S. Takeuchi, H. Tokieda, M. Tsumura, T. Uesaka, Y. Yanagisawa, K. Yako, R. Yokoyama, K. Yoshida, M. Assie, D. Beaumel, H. Fariouz, A. Stolz, "
    4   ", at the JPS Fall meeting, Sep. 20–23, 2013, Kochi University, Japan

4. S. Go, E. Ideguchi, M. Kobayashi, R. Yokoyama, K. Kisamori, S. Michimasa, S. Shimoura, M. Niikura, A. Yagi, K. Nishibata, I. Matea, D. Suzuki, D. Verney, F. Azaiez, M. Sugawara, M. Koizumi, Y. Fuji, T. Shizuma, A. Kimura, H. Harada, K. Furutaka, S. Yakamura, F. Kitatani, Y. Hatsukawa, M. Oshima "35S   ",
    at the JPS Fall meeting, Sep. 20–23, 2013, Kochi University, Japan

5. M. Dozono, T. Uesaka, M. Sasano, J. Zenihiro, H. Matsubara, S. Shimoura, K. Yako, S. Michimasa, S. Ota, H. Tokieda, H. Miya, S. Kawase, R. Tang, K. Kisamori, M. Takaki, Y. Kubota, C.S. Lee, T. Fujii, R. Yokoyama, H. Sakai, T. Kubo, K. Yoshida, Y. Yanagisawa, N. Fukuda, H. Takeda, D. Kameda, N. Inabe, T. Wakasa, K. Fujita, S. Sakaguchi, M. Ichimura, H. Sagawa "   0-   ", at the JPS Fall meeting, Sep. 20–23, 2013, Kochi University, Japan

6. R. Yokoyama, E. Ideguchi, G. Simpson, M. Tanaka, S. Nishimura, G. Lorusso, H. Sumikama, P. Doornenbal, H. Baba, T. Isobe, P-A.Sderstrm, J. Wu, Z. Xu, R. Browne, Z. Patel, S. Rice, L. Sinclair, Z. Li, H. Watanabe, G. Gey, E. Sahin, F. Bello, Z. Vajra, I. Kuri, J. Taprogge, A. Odahara, Y. Fang, R. Daido, A. Yagi, K. Nishibata, N. Aoi, K. Kobayashi, S. Michimasa, M. Matsushita, M. Kobayashi, S. Go, T. Kubo, D. Kameda, N. Inabe, H. Takeda, N. Fukuda, H. Suzuki, I. Nishiduka, T. Komatsubara, C.-B. Moon, "   Pm
    ", at the JPS Fall meeting, Sep. 20–23, 2013, Kochi University, Japan

7. C.S. Lee, S. Ota, H. Tokieda, R. Kojima, Y. Watanabe, and T. Uesaka, "
    ", at the JPS Spring meeting, Mar. 27–30, 2014, Tokai University, Japan.

8. S. Kawase, T. Uesaka, S. Shimoura, K. Yako, S. Ota, S. Michimasa, H. Tokieda, H. Miya, T.T. Leung, K. Kisamori, M. Takaki, Y. Kubota, C.S. Lee, R. Yokoyama, T. Fujii, M. Kobayashi, M. Sasano, J. Zenihiro, H. Matsubara, M. Dozono, J. Lee, H. Sakai, T. Kubo, K. Yoshida, N. Inabe, Y. Yanagisawa, H. Takeda, K. Kusaka, N. Fukuda, D. Kameda, H. Suzuki, T. Kawahara, T. Wakui, S. Sakaguchi, T. Noro, T. Wakasa, J. Yasuda, T. Fukunaga, Y. Maeda, W. Kim. S. Hwang, S. Stepanyan, A. Obertelli, A. Galind-Uribarri, E. Padilla-Rodal, D. Beaumel, "
    AO(p,2p)   ", at the JPS Spring meeting, Mar. 27–30, 2014, Tokai University, Japan

9. S. Ota, A. Corsi, M. Dozono, U.Garg, T. Hashimoto, M. Ito, T. Kawabata, S. Kawase, R. Kojima, Y. Kubota, C.S. Lee, Y. Maeda, J. Matta, Y. Matsuda, S. Michimasa, A. Obertelli, H. Otsu, D. Patel, C. Santamaria, M. Sasano, M. Takaki, T. Terashima, H. Tokieda, T. Uesaka, H. Yamaguchi, J. Zenihiro and H307 collaboration, "
                                        ", at the JPS Spring meeting, Mar. 27–30, 2014, Tokai University, Japan

10. H. Tokieda, S. Ota, M. Dozono, T. Gunji, H. Hamagaki, T. Hashimoto, T. Kawabata, S. Kawase, R. Kojima, S. Kubono, Y. Kubota, C.S. Lee, Y. Maeda, H. Matsubara, S. Michimasa, H. Otsu, M. Sako, T. Uesaka, H. Yamaguchi, Y. Watanabe, "   ", at the JPS Spring meeting, Mar. 27–30, 2014, Tokai University, Japan

11. K. Yako, "Study of nuclear matrix element of the double-beta decay by charge-exchange reactions", JPS Spring meeting, Mar. 27–30, 2014, Tokai University

12. Y. Kubota, M. Sasano, T. Uesaka, M. Dozono, M. Itoh, S. Kawase, M. Kobayashi, C.S. Lee, H. Matsubara, K. Miki, H. Miya, S. Ota, K. Sekiguchi, T. Shima, T. Taguchi, A. Tamii, T. L. Tang, H. Tokieda, T. Wakasa, T. Wakui, J. Yasuda, and J. Zenihiro "   ", at the JPS Spring meeting, Mar. 27–30, 2014, Tokai University, Japan

13. T. Gunji (invited), "RHIC-LHC   ", at the JPS Fall meeting, Sep. 20–23, 2013, Kochi University, Japan

14. Y. Yamaguchi for the PHENIX Collaboration, "Dark photon search at the PHENIX experiment", at the JPS Fall meeting, Sep. 20–23, 2013, Kochi University, Japan

15. K. Terasaki, "COBRA GEM   ", at the JPS Fall meeting, Sep. 20–23, 2013, Kochi University, Japan

16. S. Hayashi for the ALICE Collaboration, "Dielectron measurement in $\sqrt{s_{NN}} = 5.02$ TeV $p-$Pb collisions at LHC-ALICE", at the JPS Fall meeting, Sep. 2023, 2013, Kochi University, Japan

17. Y. Sekiguchi, "   SOI   ", at the JPS Fall meeting, Sep. 20–23, 2013, Kochi University, Japan

18. T. Gunji for the ALICE Collaboration, "R&D status of the ALICE GEM-TPC upgrade", at the JPS Spring meeting, Mar. 27–30, 2014, Tokai University, Japan

19. K. Yukawa, T. Gunji, H. Hamagaki, K. Terasaki, "GEM-TPC ", at the JPS Spring meeting, Mar. 27–30, 2014, Tokai University, Japan

20. Y. Utsuno, N. Shimizu, M. Honma, T. Mizusaki, and T. Otsuka , "Shell evolution in antimony isotopes", JPS 2012 Autumn Meeting, Sep. 11–14, 2012, Kyoto Sangyo Univ., Kyoto, Japan.

21. S. Ebata, "Application of Cb-TDHFB to nuclear collision II", JPS 2012 Autumn Meeting, Sep. 11–14, 2012, Kyoto Sangyo Univ., Kyoto, Japan.

22. N. Shimizu, T. Mizusaki and K. Kaneko, "Extension of Monte Carlo method on nuclear shell model diagonalization", JPS 2012 Autumn Meeting, Sep.11–14, 2012, Kyoto Sangyo Univ., Kyoto, Japan.

23. N. Shimizu, "Nuclear structure calculations aimed at K computer", JPS 2012 Autumn Meeting, Sep.11–14, 2012, Kyoto Sangyo Univ., Kyoto, Japan.

24. T. Yoshida, N. Itagaki and K. Katō, " Study of linear-chain structure of ^{16}O in alpha cluster model" , JPS 2012 Autumn Meeting, Sep.11–14, 2012, Kyoto Sangyo Univ., Kyoto, Japan.

25. Y. Utsuno, T. Otsuka, N. Shimizu, T. Mizusaki, and M. Honma, "Energy levels and shell evolution for neutron-rich Ca isotopes" JPS 2013 Spring Meeting, Mar. 26–29, 2013, Hiroshima Univ., Hiroshima, Japan.

26. T. Yoshida, N. Shimizu, T. Abe and T. Otsuka, "Study of light-nuclei density measured from body-fixed frame in Monte Carlo shell model", JPS 2013 Spring Meeting, Mar. 26–29, 2013, Hiroshima Univ., Hiroshima, Japan.

27. S. Ebata, T. Nakatsukasa, T. Inakura, "Systematic study of low-lying E1 mode", JPS 2013 Spring Meeting, Mar. 26–29, 2013, Hiroshima Univ., Hiroshima, Japan.

28. S. Ebata, "Approaches to nuclear dynamics by time dependent mean field theory", JPS 2013 Spring Meeting, Mar. 26–29, 2013, Hiroshima Univ., Hiroshima, Japan.

29. N. Shimizu, Y. Utsuno, S. Ebata, M. Honma, T. Mizusaki, and T. Otsuka , "Study of E1 excitation for neutron-rich Ca isotopes", JPS 2013 Spring Meeting, Mar. 27, 2013, Hiroshima Univ, Hiroshima, Japan.

C. Lectures

1. Y. Utsuno (invited), "Large-scale shell-model calculations for exotic nuclei", The 12th CNS International Summer School (CNSSS13), Riken, Wako and Hongo, Japan, August 28-September 3, 2013.

D. Seminars

1. T. Otsuka, "Evolutions of shell structure and shapes in exotic nuclei ", April 29, 2013, IPN, Orsay, France.

2. T. Otsuka, "Fukushima Nuclear Power Plant Accident and Nuclear Physicists", April 30, 2013, IPN, Orsay, France.

3. T. Otsuka, "Evolutions of shell structure and shapes in exotic nuclei ", May 3, 2013, GANIL, Caen, France.

4. T. Otsuka, "Tensor force in nuclei", May 28, 2013, Hanyang University, Seoul, Korea.

5. T. Otsuka, "Fukushima Nuclear Power Plant Accident", August 15, 2013, GSI Colloqium, GSI, Darmstadt, Germany.

6. T. Otsuka, "Shell and shape evolutions in exotic nuclei - How magic are ^{54}Ca and $^{68-78}$Ni? -", July 31, 2013, Seminar at Technical University of Darmstadt, Darmstadt, Germany.

Personnel

Director

    OTSUKA, Takaharu   *Professor, Department of Physics,*
                                                      Graduate School of Science

Scientific Staff

SHIMOURA, Susumu	*Professor*
HAMAGAKI, Hideki	*Associate Professor*
YAKO, Kentaro	*Associate Professor*
SHIMIZU, Noritaka	*Project Associate Professor*
YAMAGUCHI, Hidetoshi	*Lecturer*
MICHIMASA, Shin'ichiro	*Assistant Professor*
GUNJI, Taku	*Assistant Professor*
OTA, Shinsuke	*Assistant Professor*

Guest Professors

UTSUNOMIYA, Hiroaki	*Konan University*
UTSUNO, Yutaka	*JAEA*

Technical Staff

OHSHIRO, Yukimitsu   YAMAZAKI, Norio

Technical Assistants

WATANABE, Shin-ichi

YAMAKA, Shoichi

NINOMIYA, Hideaki

YOSHIMURA, Kazuyuki

KUREI, Hiroshi

YOSHINO, Akira

SENOO Takehiko

TANAKA Masahiro

Post Doctoral Associates

YOSHIDA, Toru

DOZONO, Masanori

STEPPENBECK, David

NAKAO Taro

YAMAGUCHI, Yorito

Graduate Students

KAHL, David

TAKAHARA, Akihisa

TOKIEDA, Hiroshi

KAWASE, Shoichiro

KISAMORI, KenIchi

SEKIGUCHI, Yuko

KUBOTA, Yuki

TERASAKI, Kohei

YUKAWA, Kentaro

MATSUSHITA, Masashi

MIYA, Hiroyuki

TSUJI, Tomoya

HAYASHI, ShinIchi

TAKAKI, Motonobu

YOKOYAMA, Rin

LEE, CheongSoo

KOBAYASHI, Motoki

Administration Staff

YOSHIMURA, Hiroshi

YAMAMOTO, Ikuko

ENDO, Takako

KISHI, Yukino

ITAGAKI, Toshiko

SOMA, Yuko

Committees

Steering Committee

AIHARA, Hiroaki	*Department of Physics, Graduate School of Science, UT*
HOSHINO, Masahiro	*Department of Earth and Planetary Science, Graduate School of Science, UT*
MIYASHITA, Seiji	*Department of Physics, Graduate School of Science, UT*
OTSUKA, Takaharu	*Department of Physics, Graduate School of Science, UT*
SHIMOURA, Susumu	*Center for Nuclear Study, Graduate School of Science, UT*
HAMAGAKI, Hideki	*Center for Nuclear Study, Graduate School of Science, UT*
GONOKAMI, Makoto	*Department of Physics, Graduate School of Science, UT*
NAGAMIYA, Shoji	*J-PARC Center, KEK and JAEA*
KOBAYASHI, Tomio	*International Center for Elementary Particle Physics, UT*
TAKAHASHI, Hiroyuki	*Department of Nuclear Engineering and Management, Graduate School of Engineering, UT*